中国科学院大学
University of Chinese Academy of Sciences

博士学位论文

太阳黑子振荡及半影动力学纤维的观测研究

作者姓名：Priya Thambaje Gopalan

指导教师：邓元勇 研究员　苏江涛 研究员

中国科学院国家天文台

学位类别：理学博士

学科专业：天体物理

培养单位：中国科学院国家天文台

2018 年 6 月

Observational study of Sunspot oscillations and penumbral dynamic fibrils

By

Priya Thambaje Gopalan

A Dissertation Submitted to
The University of Chinese Academy of Sciences
in partial fulfillment of the requirement
for the degree of
Doctor of Philosophy
in Astrophysics

National Astronomical Observatories of China
Chinese Academy of Sciences

June, 2018

中国科学院大学
研究生学位论文原创性声明

本人郑重声明：所呈交的学位论文是本人在导师的指导下独立进行研究工作所取得的成果。尽我所知，除文中已经注明引用的内容外，本论文不包含任何其他个人或集体已经发表或撰写过的研究成果。对论文所涉及的研究工作做出贡献的其他个人和集体，均已在文中以明确方式标明或致谢。

作者签名：

日　　期：

中国科学院大学
学位论文授权使用声明

本人完全了解并同意遵守中国科学院有关保存和使用学位论文的规定，即中国科学院有权保留送交学位论文的副本，允许该论文被查阅，可以按照学术研究公开原则和保护知识产权的原则公布该论文的全部或部分内容，可以采用影印、缩印或其他复制手段保存、汇编本学位论文。

涉密及延迟公开的学位论文在解密或延迟期后适用本声明。

作者签名：　　　　　　　　导师签名：

日　　期：　　　　　　　　日　　期：

摘　　要

太阳黑子振荡，虽然已经研究了近60年，但是真正解决的问题并不多。在近十年中，由于地面和空间多波段、高分率望远镜的投入使用，带动了太阳振荡研究的发展。其中，黑子本影振荡和半影波的传播又重新成为热门的研究课题。光球和色球黑子本影振荡有5分钟和3分钟周期的差别。5分钟振荡是光球和色球半影中的现象。它的振幅由于随着太阳大气高度的增加而减少，所以在上层色球和过渡区中它很难被探测到。另一方面，3分钟的振荡频率在色球本影以及色球和日冕之间本影的过渡区中占据主导地位。多年来，5分钟与3分钟黑子振荡的内在联系、产生的物理机制以及它们与日冕加热的关系是太阳物理研究面临的一个大的挑战。基于此，我们在这篇论文中有针对性的提出了两个不同的问题。第一个是在不同太阳大气高度中观测到的半影行波驱动源是什么，它们与黑子本影振荡有什么内在的联系。第二个是黑子本影振荡和色球超半影纤维动力学演化的关系问题。我们的研究在这连个问题上取得了进展。利用美国大熊湖天文台1.6米太阳望远镜观测到的两个黑子数据，通过研究黑子光强和多普勒速度的演化，用快速傅立叶变换方法得到了振荡频谱和主要波周期。我们首次发现当本影行波传播到本影-半影边界时，出现两种传播方向，其一是继续沿着径向传播，最终发展成传统意义上的半影行波；其二是做螺旋运动，重新返回到本影中心并在那里膨胀，开启下一次的本影振荡事件。这意味着本影振荡与半影行波在本影-半影边界可能有共同的驱动源，而不是简单的前者驱动后者的问题。另外，我们从统计上研究了与超半影纤维相关的物质流动，发现了纤维中物质流动与太阳黑子振荡的关系，即：黑子本影振荡可能是超半影纤维动力学演化的驱动源。进一步研究发现，超半影纤维的旋转运动会到导致其缠绕强度的增加，进一步可能导致其内部电流的增强，这与我们观测到日冕中超半影纤维增亮存在着时间上的正相关性，由此可知在本事例中半影纤维中的欧姆耗散是加热纤维的主要能源。

关键词： 太阳，太阳黑子，磁场，纤维，振荡，波

Abstract

Over the last 60 years there had been discussions and debates on the spatial characteristics of the umbral oscillations. Basically 5-min oscillations indicate the photospheric phenomenon. Their amplitude decreases with increasing height and they can hardly be detected in the upper chromosphere and transition region. The sunspot serves the main object to understand the study of oscillations. The umbral oscillations in sunspot could trace the eigenmodes from g-modes (periods of several tens of min) to $p-$modes (periods of tens of seconds). On the other hand, the oscillatory power in the 3-min band shows a dominant peak in the sunspot chromosphere and in the transition region between the chromosphere and the corona. The propagation of umbral and penumbral waves from photosphere through corona has been a hot topic since last decade. The connection with coronal heating is a big challenge infront of solar community. These are major long-standing problems in solar physics and serve as a common motivation for most of the studies. Broadly, two different issues are addressed, one is the origin of the emergence of RPWs from sunspots using the spectra of TiO, Hα, and 304 Å for various atmospheric heights from the photosphere to lower corona and the other is the relation between the umbral oscillations and the evolution of dynamic fibrils from sunspots. To be more precise, the connection between the chromospheric umbral oscillations and the running waves associated with them has been looked upon.

The observational study performed in this work gives an insight into the oscillations of 3, 5 and 8-min periods that have significance with sunspot oscillations at different atmospheric layers and connects with the running waves to trace the emergence of running umbral and penumbral waves. Alternatively, the study of velocity and intensity flows associated with the dynamic fibrils are performed statistically to understand the origin of flows and its relation with the oscillations in sunspots. The Comprehensive imaging and spectroscopic observations at high spectral and spatial resolution provides new insights into the origin of running waves characteristics and its distribution across the sunspot atmosphere.

Observations were carried out on two prime sunspot with 1.6-m Goode Solar Telescope (GST) at the Big Bear Solar Observatory. The high resolution imaging observations were performed with NOAA Active Regions 12127, 12132 and multiple spectral lines were scanned co-temporally to sample the dynamics at the photospheric and chromospheric layers. 1-2.5 hours of observations done at high spatial and temporal resolution have been analyzed according to their evolution in spectral intensities and Doppler velocities. A Fast Fourier Transform method

(FFT) was adopted to obtain the wave power and dominating wave periods. A reconstruction of the magnetic field inclination based on sunspot oscillations was developed.
This study measured oscillations of various periods. Umbral and penumbral waves have been traced based on these oscillations. Using phase space filter running umbral and penumbral waves are detected and showed their emergence. The initial emergence of the 3-min oscillations are noticed closer to or on umbral boundaries and these 3-min oscillations are observed as propagating from a fraction of preceding Running Penumbral Waves (RPWs). These fractional wavefronts rapidly separates from RPWs and move towards umbral center, wherein they expand radially outwards suggesting the beginning of a new umbral oscillation. We found that most of these umbral oscillations further develop into RPWs. Further, a statistical analysis of dynamic fibrils are performed from the measurement of its upflows and downflows, which indicates that these fibrils are triggered by the oscillations in sunspot. Our analysis also finds that some dynamic fibrils rooted at the sunspot umbral boundary showing brightening along it. We presume that this brightening could be either due to the twisting of all the fibrils together into one which results in some ohmic loss and becomes a cause for the heating of the loop.

Keywords: Sun, Sunspots, Magnetic fields, Fibril, Oscillations, Waves

目　录

表　　格

插　　图

第一章 Introduction

The sun known as a second-generation star is a ball of hot gas located at the center of our solar system. The formation of sun is from the material left by the first generation stars in our milky way. For the sustainment of life on the earth, the sun plays a major role. The life on earth is completely impossible without the solar energy. Also, it emanates highly energetic charged particles continuously into the interplanetary space. These energetic particles are channeled down through polar field lines and interacts with the atmosphere of the earth and produces beautiful auroral patterns. The temperature at the core of the sun is about 27 million degrees Fahrenheit. It is extremely difficult to reproduce the extreme conditions in the outer atmosphere of the Sun and thus makes it a completely unique physical laboratory to enhance our understanding in different branches of physics. The nuclear reactions are the main source for the generation of energy at the core of the sun. Four protons fuse together to form Helium nuclei and releases energy. The main mode of transportation of energy is by radiation upto 0.67 $R_\odot$ and by convection from there to the solar surface. Based on the transportation of energy, these regions are termed as radiative and convective zones, respectively. Different layers of the Sun are shown in Figure 1.1.

1.1 The Solar atmosphere

The sun's atmosphere is composed of, the photosphere, the chromosphere and the corona. The different layers of the solar atmosphere are shown in Figure 1.1. The temperature variation across these layers is shown in Figure 1.2 for a model solar atmosphere. Starting from the surface of the Sun, the temperature first decreases over a few hundred kilometres and reaches a minimum value. This region is the lowest layer of the sun's atmosphere and is known as photosphere which is about 500 kilometers thick. Photosphere is the region where the energy of the sun is released as light. It gradually rises up to about 2,000 km height from the photosphere and then sharply increases to the order of a million kelvin within the short distance of a few hundred kilometers. The layer between the temperature minimum upto where the temperature becomes approximately 20,000 K is generally defined as chromosphere, the region where the temperature reaches $\sim 10^6$ K and the densities are very low compared to the chromosphere is called solar corona. A very thin layer separating the dense, cool chromosphere and tenuous, hot corona with temperatures of the order of 10^5 K, is the transition region. Because of the huge variation in temperature, lines from molecular G-band to those from heavily ionized iron is observed in the solar atmosphere. Different

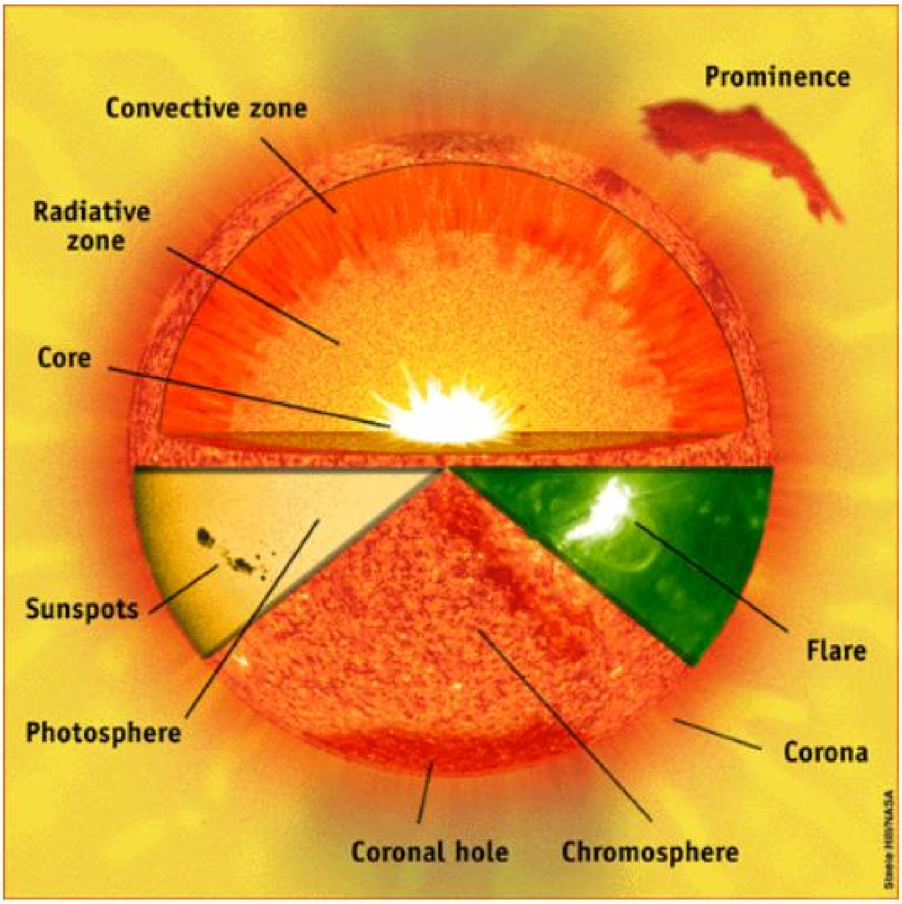

图 1.1: A cartoon image showing the different layers of Sun from the central core to outer corona. Credit: (`http://sohowww.nascom.nasa.gov`).

lines formed at different heights of the solar atmosphere are shown in Figure 1.2. The temperature variation presented here is a representative variation and the actual heights of these layers may vary from one region of the solar atmosphere to the other. The parameter that determines the dynamics of solar atmosphere is plasma-β which is defined as the ratio of gas pressure to magnetic pressure given by

$$\beta = \frac{p_{gas}}{p_{mag}} \approx \frac{nkT}{(B^2/8\pi)} \tag{1.1}$$

The variation of plasma-β in the solar atmosphere is shown in Figure 1.3. At the photospheric level, this parameter is greater than 1 implying the domination of plasma motions over the magnetic fields whereas in the chromosphere and corona this value decreases below 1, leading to a confinement of plasma to the magnetic structures (this makes the corona highly structured). In the higher upper atmosphere this value rises again causing the magnetic field to transport out with the solar wind plasma.

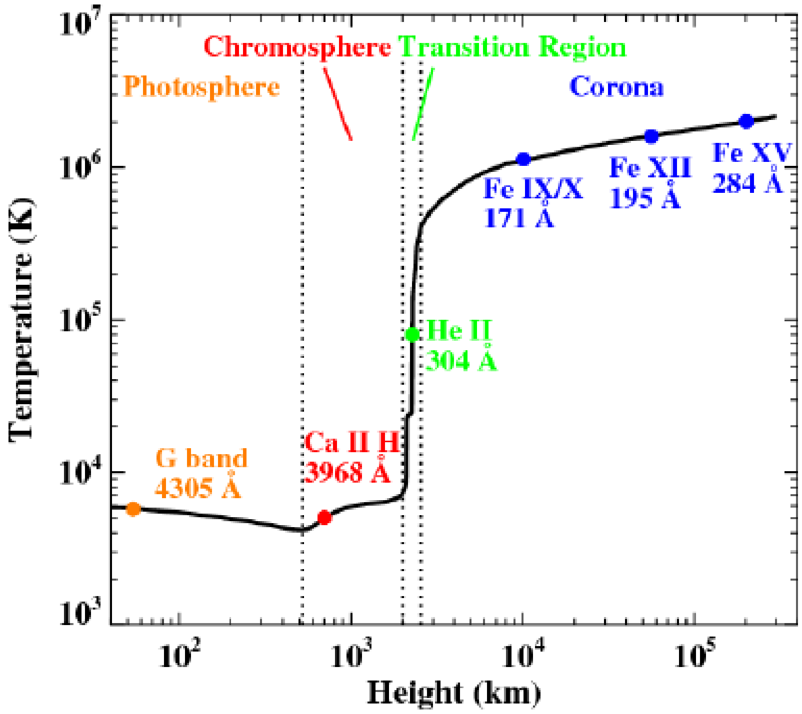

图 1.2: Temperature variation from photosphere to corona. Spectral lines that can be used to observe different regions of the atmosphere are marked at respective locations[3].

1.1.1 Photosphere

The surface of the Sun from where photons start escaping into space is called Photosphere. Below this layer, as none of the photons escapes, it is not possible to be seen. This layer is a few hundred kilometers thick and is usually defined using the optical depth. Since this quantity is dependent on wavelength, the exact definition of photosphere is given as the region where optical depth τ becomes unity for the radiation of wavelength 5000 Å. The temperature of this layer is about 6400 K. Many features like granules, supergranules, and sunspots are observed in this layer. Granules are small structures appearing bright at centre, and formed due to surface convection. They have a typical size of ≈100-1100 km and several minutes of lifetimes. Supergranules are the higher version of the granules, and are about 30,000 km across, and some thousand of kilometres thick and their lifetime is of the order of few days. The material from the interior is convected upwards around the cell centre and spreads out towards the boundaries of the cell almost in horizontal direction with velocities of 0.4 km s^{-1} and followed by convection downwards with velocities of 0.1 km s^{-1}. In this process the convective flow transports concentrations of magnetic fields towards the boundary and forms the so called magnetic network region around it. This region within the cell is called Internetwork (IN). Here, due to high plasma-β, most of the pattern is dominated

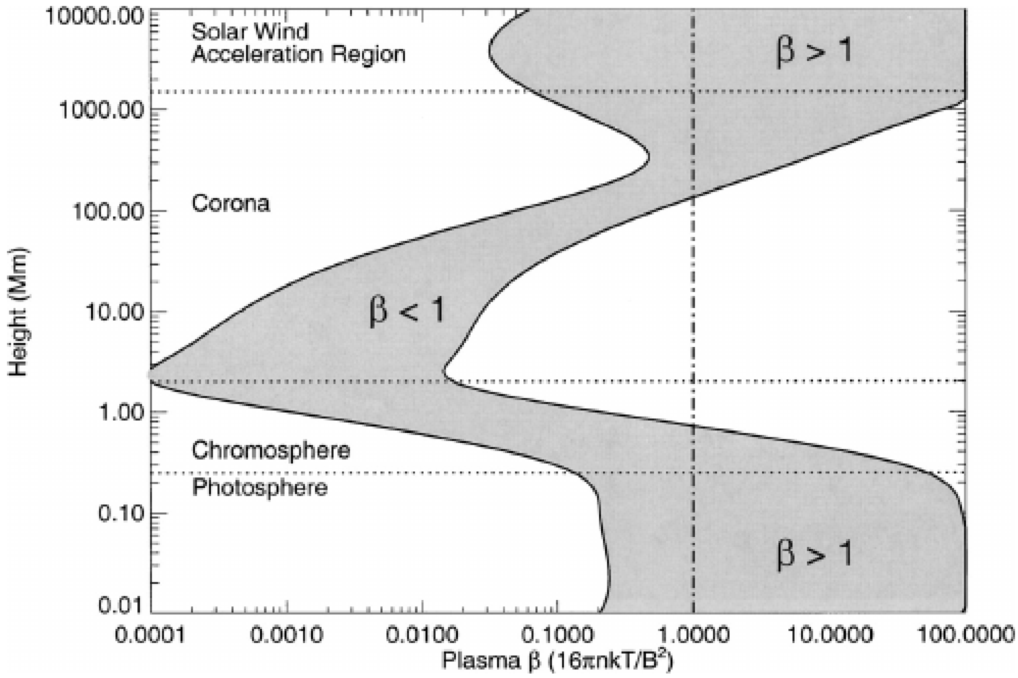

图 1.3: Variation of plasma-β in the solar atmosphere for a range of magnetic field strengths between 100 G and 2500 G [4].

by convection. But a sunspot is an exception to this, where the magnetic field concentration is high and therefore appears dark due to the inhibition of convective flows. The dark region of the sunspot is called umbra where the temperature drops below the ambient temperature and the less dark outer region of a sunspot is known as penumbra. The sunspots visible in the photosphere varies periodically with a period of 11 years which is termed as solar cycle. Although, the sunspots appears dark, the total brightness of the Sun increases by about 0.1% during the solar maximum period due to the presence of faculae.

1.1.1.1 Quiet sun

The quiet Sun(QS) is defined as the region outside sunspots and pores where strong coherent magnetic fields over large scales are observed. But the QS is far from being magnetic free. High spatial resolution and high sensitivity QS magnetograms show magnetic fields in network and IN elements. The network elements have strong fields of the order of 1 kG and are located at the borders of the supergranular cells with typical diameters of 30,000 km, while the IN ones, in the cell interior, show much weaker fields. It has been estimated that a significant fraction of the total magnetic flux of the solar surface resides in the quiet sun. The origin of both network and IN elements is not clear. Numerical simulations by Vogler et al. (2007) [15] has shown that the vigorous convective motions in the solar photosphere, where the dynamic pressure of the flows exceeds the magnetic pressure, can cause an efficient amplification of the magnetic energy at small scales from a magnetic seed[16]. This small-scale dynamo action could be the source of the quiet Sun magnetic fields. The quiet solar atmosphere is highly variable in both space and time, due to the interaction between magnetic fields, solar differential rotation and convective flows. At the solar surface, the large scale convective flows form a pattern of cells known as super-granular cells. The magnetic filed lines are transported horizontally at the edges of the supergranular cells, resulting to the formation of the magnetic network.

1.1.2 Chromosphere

The Chromosphere extends up to the transition region starting from the temperature minimum region. The thickness of chromosphere is about 2,000 km to 3,000 km and temperature ranges from about 4,400 K to 20,000 K. Within this temperatures the hydrogen is partially ionized with most of them in the excited state leading to Hα emission which makes this layer to appear pinkish in colour because of which it is named as chromosphere at 6563 Å. Other activities like spicules and prominences can also be observed in this layer. Spicules are nothing but jet like eruptions of gas that propagates upwards, releasing material off the surface and outwards towards the Corona with a speed of about 20-30 km s^{-1}. Spicules have a lifetime of the order of minutes and are usually found at the boundaries between supergranules and are formed due to shocks which are due to the p-mode leakage at inclined magnetic fields[17]. When this is viewed in Hα line they appear dark on the disk covering about 10% of the solar surface. Solar prominences are dense clouds of gas suspended above the surface of the by the magnetic field. Basically there are two types of prominences: Quiescent and Active. Quiescent prominences are the more stable and long-lived prominences and retains their structure for upto a year before they evolve by breaking up. Active prominences are the opposite of quiescent prominences and tend to be short-lived and smaller. Prominences appears dark and are called filaments. The transition region is a very thin layer separating the chromosphere from corona with temperature varying between 20,000 K to 1 MK over a short distance. The plasma-β becomes very low and the magnetic fields becomes dominant (see Figure 1.3). As the hydrogen gets ionized at these high temperatures, the dominant emission comes from ions of carbon, oxygen and silicon[18].

1.1.3 Corona

The outer atmosphere of the Sun is called Corona, where temperatures are of the order of few million kelvin. At such a high temperatures, the hydrogen and helium gets strip of the electrons and goes undetected. This is the reason why the spectral lines are observed from highly ionized calcium and iron. When the spectral lines are observed during solar eclipse in visible light, the emission that occurs is due to three main components which are termed as K-corona, F-corona, and E-corona. K-corona displays a continuous spectrum arising out of the photospheric light that is scattered by the electrons of the coronal plasma. The F-corona is due to the photospheric light scattering by dust particle in the ecliptic plane. As they have high thermal velocities of the scattering electrons, these lines are invisible in the K-corona. E-corona represents the emission directly coming from the coronal gas and consists of isolated spectral lines formed by the coronal ions. This is due to the thermal emission of the interplanetary dust and is largely in infrared part of the spectrum. The plasma mostly gets confined to coronal loops as the plasma-β is very low in this region. These loops either extend into the interplanetary space or turn back to the photosphere which are often referred to open and closed loops respectively. Corona can be divided into three regions: Active regions (ARs), coronal holes and QS regions. ARs are dominated by closed field structures, and the coronal holes are dominated by open field structures. The corona is magnetically dominated making the shape of outer corona varying greatly over the solar activity cycle.

1.2 Active region and Sunspots

The active region on the Sun is an area with a strong magnetic field. Most solar storms like solar flares and coronal mass ejections (CME) occurs from the ARs. The Magnetic fields in ARs can be more than thousand times stronger than the average magnetic field over the Sun. Sunspots are the indicators of ARs, although not all ARs produce sunspots. Sunspots are usually surrounded faculae (singular: facula). Sunspots appear as dark areas on the otherwise bright Suns surface. The sunspot is formed due to the bursting of internal magnetic field through the visible surface and out into the corona. Sunspots appear dark because the magnetic fields get in the way of energy and heat being transported from inside the Sun to its surface. Because these areas are heated less, they are a few thousands of degrees Kelvin cooler (1,000-2,000 K normally), making them appear dark in comparison to the rest of the surface. A sunspot consists of two parts: The dark part umbra and lighter part around the dark part called penumbra as shown in Figure 1.4.

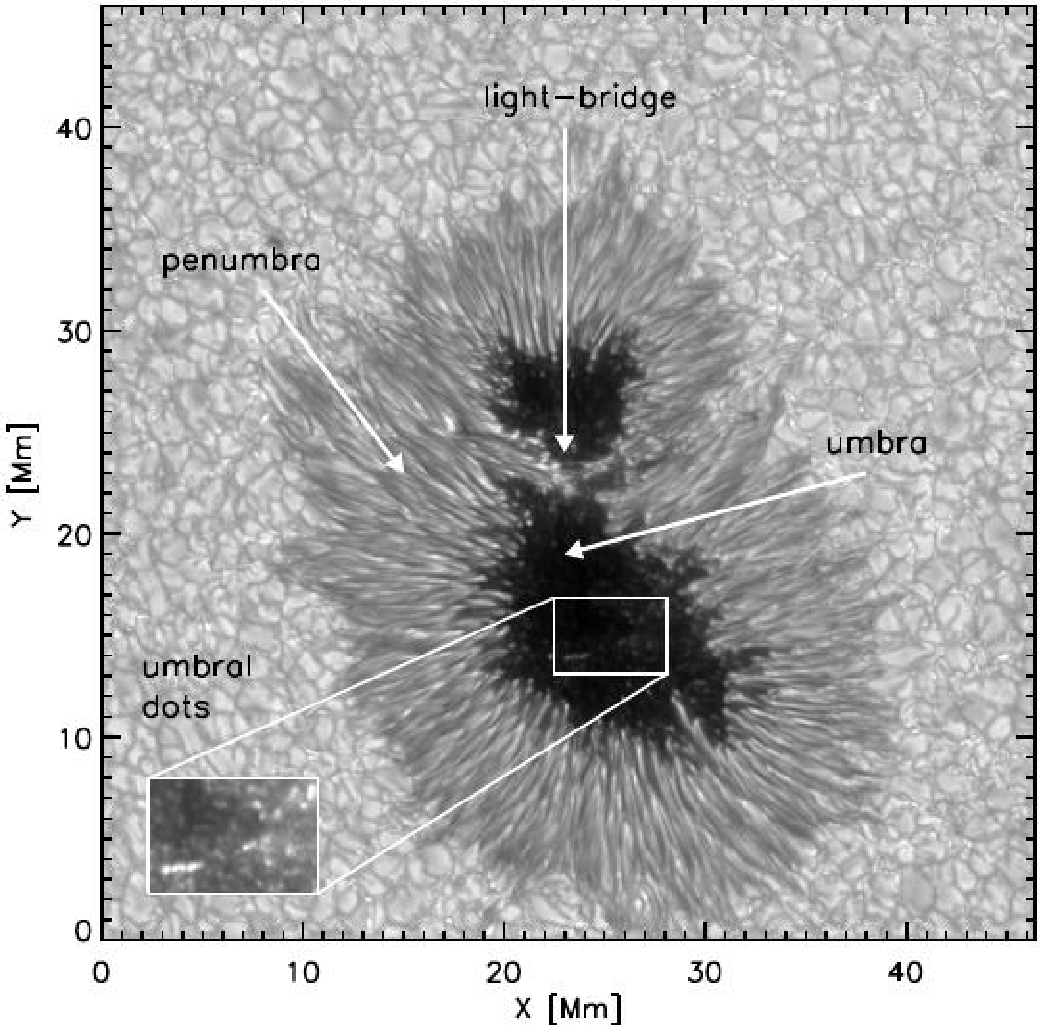

图 1.4: The image of this sunspot was taken with the Swedish 1-m Solar Telescope (SST). The various parts like umbra, penumbra, light-bridge and umbral dots can be seen. For the better vision of the umbral dots a part of the umbra is shown in lower left of the image[5].

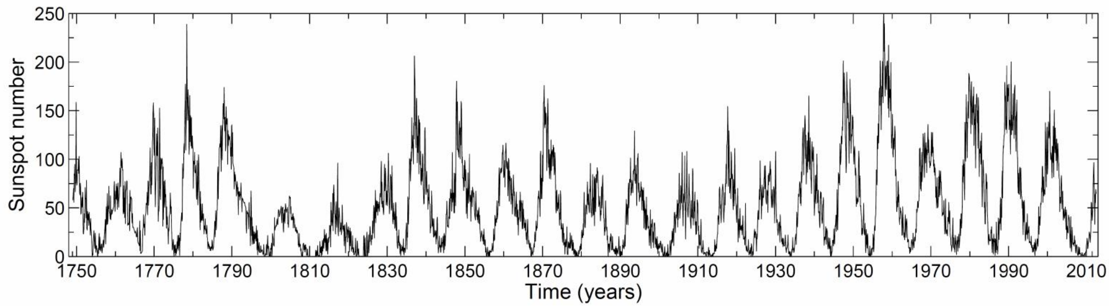

图 1.5: Solar cycle: monthly averaged sunspot number between 1750 to 2012 (Credit:http://www.ngdc.noaa.gov).

1.2.1 Magnetic field

The photospheric magnetic field has a wide range of spatial scales. The regions of enhanced surface magnetic fields are called ARs. These ARs display a bipolar configuration. The largest features in terms of size and the magnetic field strength are the sunspots. Magnetic field structures on the solar surface also appear on the scale as small as the diffraction limit of the present generation telescopes. The smallest magnetic field structures are called the magnetic elements. Outside the AR, i.e. in the quiet Sun, magnetic elements appear with enhanced density in network which are basically the boundaries of large scale convective cells. These cells with size of 20-40 Mm are called the supergranules. The magnetic field which appears in between the magnetic network is known as the IN magnetic field[19]. The magnetic field of the Sun varies in a period of about 11 years which is clearly evident in the temporal variation of daily numbers of the sunspots visible on the solar surface (Figure 1.5). The magnetic polarity reverses after ∼11 years so as to have a mean period of 22 years in the full magnetic cycle of the Sun. The dynamo is accepted as the root cause for the generation of the magnetic field and also a cause for the solar cycle. The solar activities occurring at different layers of atmosphere around the sunspots are interconnected due to various interactions occurring between energy and mass between these layers. It is known to be a strong coupling existing among the layers of chromosphere, TR, and corona during solar flares (see the review by Benz (2008)[20]). Some flare models do indicate that the magnetic reconnection to be first taking place in the corona, followed by the chromospheric heating by the accelerating particles propagating downward and the thermal conduction, which generates the emission seen as flare ribbons. The heated chromospheric plasma can then trigger an upflow, which is called chromospheric evaporation[21]. The above scenario has also been confirmed observations[22–27].

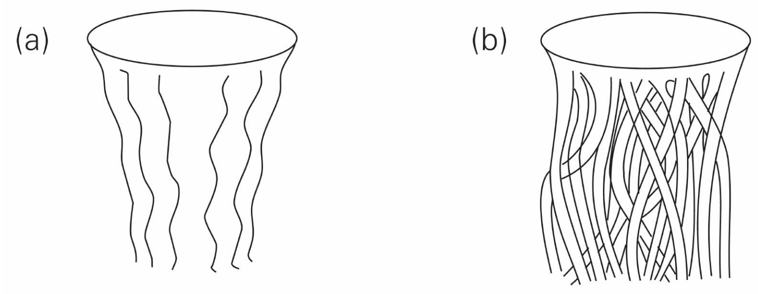

图 1.6: Panel (a) A sketch of subsurface structure of a monolithic model and panel (b) shows that of a cluster model of sunspot[6].

1.2.2 Umbra: Theoretical models

The relative darkness and the rich fine structure of sunspots constitute a challenging and enigmatic problem for theoretical models. In addition, the dynamical time-scale which is the time of the magnetocacoustic wave to propagate across the sunspot is about an hour, while the lifetime of sunspot is several weeks. Hence, because of this reason the long term stability of sunspots remains as a question. The fine structures, i.e., umbral dots, penumbral filaments, penumbral grains, etc., have a faster dynamics in comparison to the life time of sunspots. The strong magnetic field of sunspots suppresses overturning convection which is the main mechanism of heat transport to the solar surface. Therefore sunspots are cooler compared to the surrounding photosphere and appear darker[28]. Jahn (1992)[29] made an alternative scenario based on a monolithic flux tube. A sketch is shown in Figure 1.6 (a), which expands from the deeper layers towards the surface of the Sun to balance the stratified gas pressure of field free surrounding. Here, the magnetic field takes a form of a funnel where the diameter of the monolithic flux tube is smaller (stronger B) in sub-surface layers. When the flux system is thermally isolated from its surrounding, any form of possible energy transport from the deeper layers to the surface may cause a reduced heat flux at the surface and hence cools down, because of the increased cross section of the flux tube. As sunspot umbrae have temperatures of 4000 K and the heat transport through conduction and radiation will not suffice to maintain such a high temperature, which means that the convection is not completely inhibited in the sunspot umbrae[30]. The concept of mixing length theory with a depth dependent mixing length has been used to show the convective heat transport in sunspots[30]. The models are based on another model[31], where umbra, penumbra and the QS are thermally isolated against each other. The boundary between penumbra and the QS is known as magnetopause.

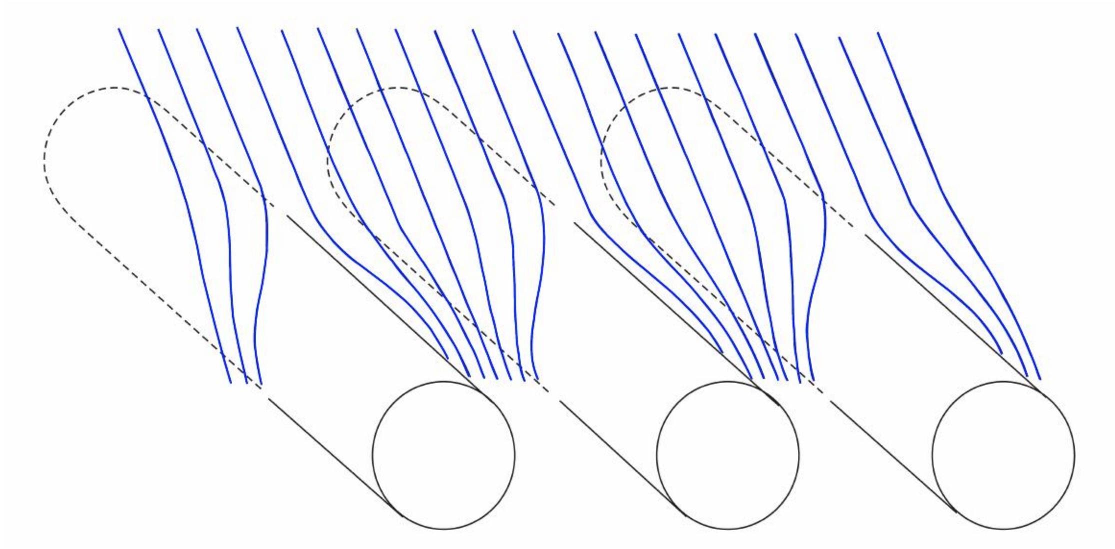

图 1.7: Uncombed penumbra: A sketch of the horizontal magnetic flux tube embedded in a relatively less inclined magnetic field[7].

1.2.3 Penumbra: Models

The heat flux in sunspot penumbrae is ∼75% of it in the QS, while the average magnetic field strength is still high, being ∼1500 G. The heat transport mechanisms like e.g., hot flows along flux tubes, says about the convection in radially aligned flux tubes and also the convection in field free gaps. Along with the heat transport in penumbrae, there are also Evershed flow, the filamentary structure of the brightness, the magnetic field and the plasma flow, and their relation each other, which all are challenges for giving the explanation using theoretical models.

1.2.3.1 The uncombed model

Auer and Heasley (1978)[32], Lites (1992)[33] and Landolfi (1996)[34] indicated that the gradient of V_{los} with respect to the optical depth τ only cannot generate the observed amount of Net circular polarization (NCP). It is said that only a gradient of B along with the gradient of V_{los} can explain the observed NCP. It is pointed out that the NCP requires a steep vertical gradient of the inclination of the magnetic filed vector (around $45°\tau^{-1}$) and also of V_{los} (around 1.5 km s^{-1})[33]. Solanki (1993)[35] said that there is steep gradient of inclination which results in a mechanical instability in the sunspot. The uncombed model of the sunspot magnetic field which successfully explained NCP observed and also naturally exhibits the presence of azimuthal variations of the magnetic field strength, the inclination and the Evershed flows[35]. In the uncombed model horizontal flux tubes, carrying the Evershed flows, are embedded in a more vertical background field. A sketch of the uncombed model is presented in Figure 1.7. According to this model the LOS of an observer penetrates a three-fold layered atmosphere where the background magnetic field is wrapped around the horizontal flux tube (Figure 1.7). Two sudden changes of the inclination of the magnetic field, first from the more vertical to the horizontal and second from the horizontal to the more vertical, are responsible for the observed NCP. The uncombed model also successfully explains the center-to-limb variation of the NCP, i.e. when the sunspot is observed at different heliocentric angles[35,36]. The three-dimensional model explains the variation in the azimuth direction of the field vector, $\delta\phi$, also has a significant influence on the NCP[37,38]. Explanation was given on the asymmetry of the NCP with respect to line-of-symmetry of the sunspot when observed in the Fe I 1.56 μm lines by a variation of the azimuthal angle $\delta\phi$ and the effect of the overturning convection (i.e. a lateral flow) had been included[39] and it was concluded that this flow does not result in a significant effect on the NCP. The main features of the uncombed model, namely more vertical field spreading to cover the interlaced horizontal field bundles, has been supported by many observational studies[37,39–46]. One feature of the model, however, namely that the horizontal field is in the form of flux tubes is being debated with increasing evidences suggesting that it is in need of revision.

1.2.4 Light bridges

As shown in Figure 1.8, the sunspot umbra can be divided into multiple cores. The Light bridge (LB) separating the umbrae appear as bright lanes of convection at photospheric heights. Since up to 20% of the plasma in LB is field-free, the magnetic field strength compared to the umbral cores is significantly reduced by 200-1500 G at the arc-second scale[47]. The magnetic field components of LB are shown in Figure 1.8 (panels (f)-(h)). In accordance with literature[48], the magnetic field is more inclined than in the nearby umbral cores. Zenith angles in LB are up to 30 Å larger. The azimuth of the field differs from the radial symmetry of the sunspot, too. As supported by Figure 1.8, the appearance of the LB in the upper photosphere (panel (c)) and chromosphere (panel (d)) gets less pronounced. So does the gradient in magnetic field strength and inclination. LBs also influence the oscillations in the sunspot chromosphere[49]. It has been reported that the waves cannot propagate across the light bridge from one umbral core to another[50]. But as umbral oscillations in the multiple umbrae seem to be in phase, it is suggested that the oscillations share the same driving source below the light bridge in a probably connected umbra. Moreover, while thin LB at low chromospheric layers reveal a standing wave behavior, wider LB exhibit running waves along the long axis towards the center of the LB with propagation speeds of 10-20 km s^{-1}. Rueedi (1995)[51] has measured strong localized down-flows of up to 1.5 km s^{-1} within the light bridge. It is suggested that the inverse wave

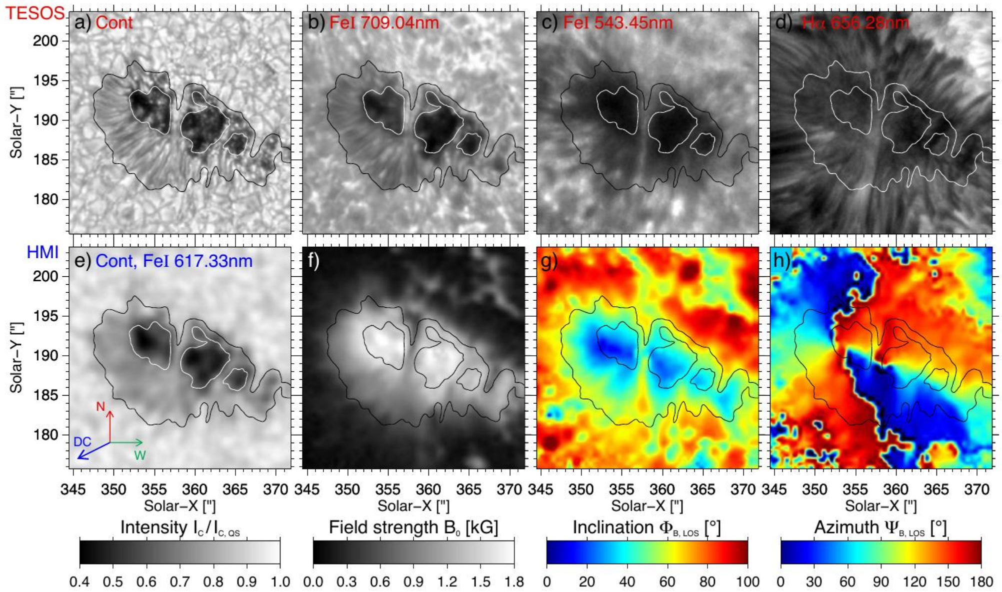

图 1.8: Major sunspot of NOAA 11455 on April 14th 2012 at 11:37:34 UTC as observed by TESOS (upper row) and HMI (bottom row). Panels (a)-(e) show the region in spectral intensity: continuum ((a), (e)), and line minima of (b) Fe I 709.04 nm, (c) Fe I 543.45 nm, (d) Hα 656.28 nm. The magnetic field parameters from the inversion of the HMI Stokes profiles of Fe I 617.33 nm are displayed in panels (f)-(h) for the field strength B_0, zenith inclination $\phi_{B,LOS}$, and azimuth $\psi_{B,LOS}$. The black contours mark the penumbral boundaries from continuum intensity. The blue arrow is pointing toward disk center[8].

propagation in LB can be considered as the counterpart of running waves along the penumbral filaments. A possible explanation considers light bridge oscillations as standing acoustic waves trapped by the atmospheric non-linearities.

1.2.5 Sunspot oscillations

The investigation of solar oscillations started with the detection of pressure waves in the overall photosphere[52]. As we know today, these acoustic p-modes propagate within the convection zone and photosphere. The most prominent wave modes have periods of 4-8 min and horizontal wavelengths of up to hundred Mm. In Helioseismology, the discrete mode pattern of wavenumbers and frequencies is used to obtain information about the interior of the Sun. When studying a local region in the lower photosphere, the periods of the characteristic p-modes peak at 5 min. The predominantly vertical oscillations have typical amplitudes of more than 0.5 km s^{-1} in Doppler velocity and a few percent in relative spectral intensity[53]. Only few years after the detection of p-modes in the solar atmosphere, significant oscillations were measured also in the sunspot atmosphere[54–56]. Periodic fluctuations of Doppler shifts and intensities of spectral lines provide evidence for compressional waves in sunspots. The power and frequency of the oscillations depend on the part of the sunspot and the atmospheric layer. As shown in Figure 1.9, the dominating peaks in the umbral power spectra shift from the 3.5 mHz ($\sim$5 min) range in the photosphere to the 6 mHz ($\sim$3 min) range in the chromosphere. Compared to the p-mode oscillations in the quiet sun, the magnetic field of sunspots damp the oscillatory amplitude in the photospheric umbra. Toward the chromosphere above the umbra, the wave power increases by more than a magnitude. In addition, the observation of sunspots at chromospheric spectral intensities reveals the visual appearance of fast propagating waves. Traditionally, the wave phenomena in sunspots[33] are classified as 1) five-minute oscillations in the sunspot photosphere, 2) three-minute oscillations and umbral flashes in the umbral chromosphere, and 3) running penumbral waves in the penumbral chromosphere. Intensity and velocity observations in various spectral lines have revealed the existence of 5 and 3-min oscillations[33,57–59] in the umbral photosphere[60]/chromosphere[55,61]. The 5-min oscillations are predominantly a photospheric phenomenon. Their amplitude decreases with increasing height and they can hardly be detected in the upper chromosphere and transition region. On the other hand, the oscillatory power in the 3-min band shows a dominant peak in the sunspot chromosphere[62,63] and in the transition region between the chromosphere and the corona[64]. A manifestation of chromospheric umbral oscillations is umbral flashes (UFs), which were first discovered[54] in Ca II H and K filtergrams and spectrograms of a sunspot. UFs appear in the form of narrow bright lanes stretched along the LB and around clusters of umbral bright points[65] when the velocity amplitudes exceed a threshold, e.g., 5 km s^{-1} for the Ca II K line. UFs are rarely observed in Hα and perhaps only when the velocity amplitude is large enough[66].

1.2.5.1 5-min Oscillations

To measure oscillations in the umbral photosphere which is a cooler surface, a variety of spectral lines of simple molecules (e.g., TiO) and non-ionized metals (e.g., Fe I, Si I, Ti I, Ni I, Mg I) have been applied. The observation and analysis of their spectral intensities and Doppler shifts have given some results[9,10,67–70]. For example, the umbral photosphere shows a very broad combination of wave modes with the five-minute mode, like in the case of p-modes in the quiet sun. The left panel of Figure 1.9 shows a power spectrum of velocity oscillations in the umbral photosphere obtained from the Fe I 630.15 nm line core. There are several individual peaks centered at periods of about 300s. The power peak at 197s (D in the left panel, E in the right panel), as well as all other modes, have counterparts in the chromospheric power spectrum (right panel). Thomas et al. (1994)[9] shows a rather strong coherence between the oscillations in the umbral photosphere with

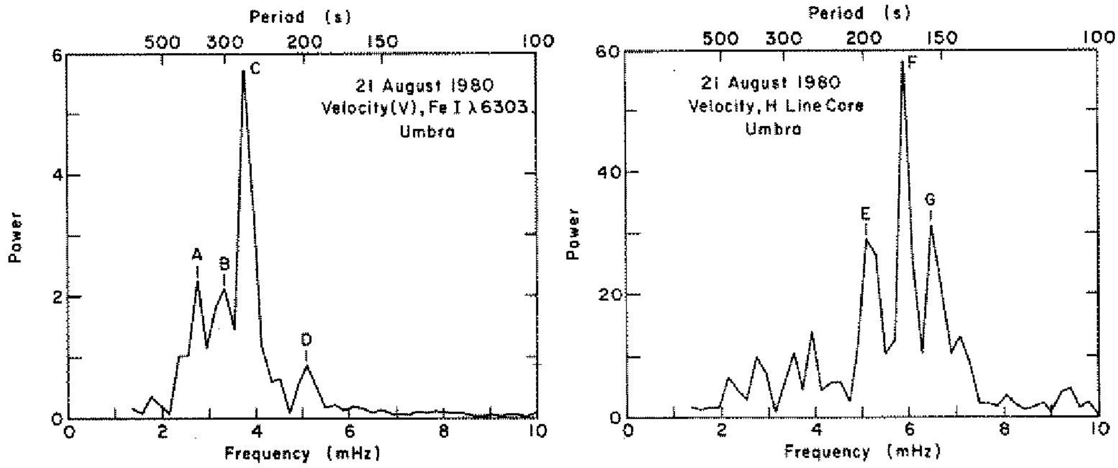

图 1.9: Velocity power spectra in a sunspot umbra from the photospheric Fe I 630.25 nm line (left panel) and chromospheric Ca II H 396.85 nm line (right panel). The units of power are 10^3 m^2 s^{-2} mHz^{-1}. The maximum power in the chromospheric case is one order of magnitude larger than in the photospheric case[9].

the wave modes at higher layers. In Figure 1.10, the temporal diagrams show the evolution of Doppler velocities in photosphere[10]. In the upper panel, the velocity oscillations are in the 2.0-4.5 mHz (4-8 min) range. The time-series stress upon the dominating five-minute oscillations. In general, the five-minute oscillations are largely coherent in the sunspot umbra and often also in a considerable part of the penumbra[71]. The velocity amplitudes typically reach values up to ± 100 m s^{-1} and more. However, the velocity of oscillations in the umbral photosphere gets reduced by a factor of two or three compared to the amplitudes of the p-modes in the area around of the sunspot, the oscillatory velocity in the umbral photosphere is reduced at least by a factor of two or three[67,69]. In the penumbra, the suppression of five-minute wave power is more moderate. Overall, the damping of the velocity power in the sunspot region makes the main distinction of five-minute waves in the sunspot region and the p-modes in the quiet sun. But even more important than their distinction is the connection between p-modes and sunspot waves. Observational evidence was given that propagating p-modes in the active region photosphere can cross the entire sunspot region[72]. When the inward and outward traveling p-mode waves in a sunspot are separated[73], it is evident that sunspot absorb up to half of the incoming power of wave power. It seems natural that the five-minute oscillations in the sunspot photosphere could be forced by the p-mode oscillations in the surrounding convection zone[74]. Moreover, Bogdan (2000)[75] proposed the absorbed acoustic wave power in sunspots for mode conversion into upward propagating magnetohydrodynamic waves .

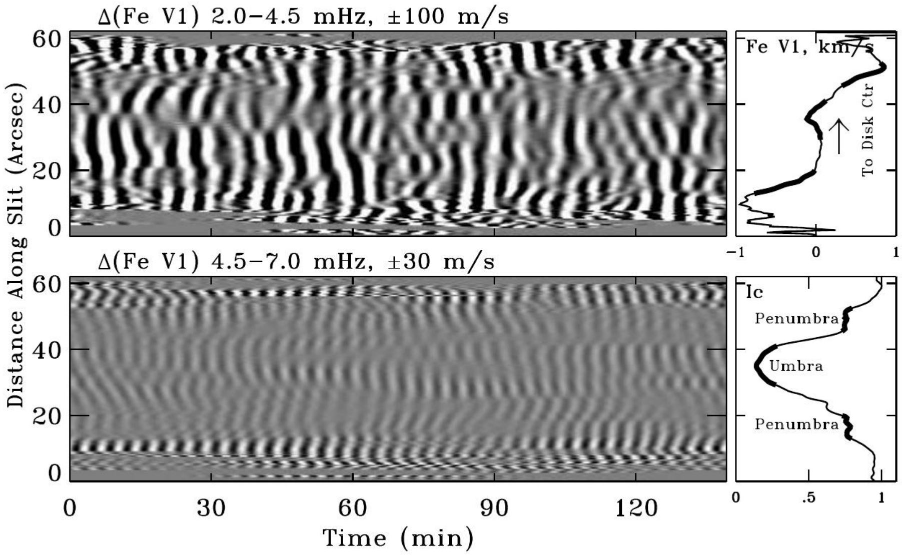

图 1.10: Doppler velocity oscillations in the sunspot photosphere filtered for the 5-min (upper left) and 3-min (lower left) period range. A slit was centered at the sunspot. The velocities were obtained from the Fe I 630.15 nm line and plotted against time. The displayed values were scaled to 100 m s^{-1} and 30 m s^{-1}. The time-averaged continuum intensity and Doppler velocity are shown in the lower and upper right panels[10].

1.2.5.2 3-min Oscillations

Three-minute oscillations in the umbral atmosphere are already present in the photosphere. As shown in the lower panel of Figure 1.10, the oscillations in Doppler velocity in the frequency range of 5-7 mHz are hard to detect. With velocity amplitudes below $\pm$ 30 m s^{-1}, the photospheric three-minute oscillations are overpowered by the sunspots five-minute oscillations. This is also reflected in the power spectrum shown in the left panel of Figure 1.9. Sunspot pores yield the same photospheric three-minute oscillations[76,77]. The situation changes towards the umbral chromosphere. The upward propagating waves in the three-minute range starts to dominate umbral sunspots wave power[78]. As shown in the right panel of Figure 1.9, the wave modes in the 5-7 mHz frequency range (2.4-3.3 min) increase in velocity power by two orders of magnitude compared to the low photospheric case. The oscillations with periods of about 2.8 min governs the chromospheric umbra. The average velocity amplitudes reach values of around $\pm$ 1 km s^{-1}. As the altitude increases, the plasma density decreases exponentially causing the kinetic energy density of the photospheric three-minute oscillations to be above the chromospheric level. It is seen that the linear upward propagating waves steepen in amplitude with the drop in atmospheric density, and eventually forms magnetoacoustic shock front in the chromosphere and transition region[79,80].

1.2.5.3 Running Penumbral waves (RPWs)

The waves and oscillations associated with the sunspots is known for more than 40 year[54]. The earlier works on the oscillations in the structures of sunspot have helped in approving the detection of long-period oscillations, generated by the response of the umbral photosphere to the five minute p-mode global oscillations. Though the oscillations in solar ARs are dominated by the periodicities which are linked to the global p-mode spectrum, a lot of alternative wave periods can be identified in the sunspot locality covering over three orders of magnitude, from several seconds[81] to in excess of one hour[82]. The dynamics in the chromospheric penumbra are dominated by running penumbral waves. The first observational evidence of running penumbral waves (RPWs) was given by Giovanelli[55] and Zirin[83] in 1972 where in they detected a concentric intensity waves propagating outward through sunspot penumbra. Since then, numerous observational and theoretical studies have been performed for the determination of nature and properties[49,50,84–94]. Most observational studies on running penumbral waves concentrates upon the spectroscopic signals and wave properties at chromospheric and upper photospheric layers. The propagation and appearance of running penumbral waves is prominent at the lower and middle chromosphere. Therefore, the waves are predominantly observed in the line core and wings of Hα, CaH and K, and the Ca II lines in the near-infrared. These waves were considered to be acoustic modes, were observed to propagate with a phase velocity of 10-20% and exhibited intensity fluctuations in the range 10-20%. Brisken et al. (1997)[95] and Kobanov (2004)[72] revealed how the frequencies and phase speeds of RPWs are largest (3 mHz, 40 km s^{-1}) at the inner penumbral boundary, and decreases to their lowest values (1 mHz, 10 km s^{-1}) at the outer penumbral edge. At chromospheric height, running penumbral waves propagate along the superpenumbral filaments upto a height of 15$''$ outside the sunspots white light boundary[89]. The spectral signal of the running penumbral waves decreases as it propagates towards the photospheric layers. In the upper photosphere, the signal is overpowered by solar p-mode oscillation at the outer penumbra. In addition, the strong Evershed flow at the outer penumbral edge gives the impression of merging with the waves. Only few attempts have been made to determine a lower photospheric signature of the wave phenomenon[10,86,91,96]. The detection is difficult since the Doppler velocity oscillation is expected to be low. Moreover, strong p-modes can propagate across the sunspot and reduce the significance of a signal from the weaker running penumbral waves. In recent studies[49,97], running penumbral waves were also measured in the chromospheric fibrils of pores. They have been classified as sunspot running waves or upwardly propagating waves.

1.3 The theory of waves

Waves exists always on the sun as it is a completely restless body. In the convection zone, turbulence generates global acoustic modes which gets trapped in the solar interior and hence is seen in the photosphere directly as five-minute oscillations. In the atmosphere of the sun, the small scale dynamical phenomena like granules, spicules etc generates variety of wave modes that contributes to the heating of the atmosphere. Waves aloso forms a main source for the transformation of energy over a long distance. The transversal waves and longitudinal acoustic waves also propagates with the speed of sound through medium in the form of compression and rarefaction. A many kinds of hydrodynamic wave components are introduced by the magnetism. These Magnetohydrodynamic waves (MHD) depends on the magnetic field of the medium. We see through literature that all these waves are present in the Sun and its atmospheres. MHD plays a very important role in the transporting the energy and heating of the chromosphere and the corona as the sun's atmosphere is covered by magnetic fields. Here a very brief introduction is given to the fundamentals of magnetohydrodynamic wave theory.

1.3.1 Basic MHD

MHD is the theory of fluid dynamics in the presence of magnetic fields. The magnetohydrodynamic theory is based on the theories of fluid mechanics and electromagnetism. In the strong magnetic fields of sunspots, the interactions between the plasma and magnetic fields plays an important role. When the strong flows are driven, the magnetoacoustic waves gets excited. Basically, MHD theory is a combination of the equations of slow electromagnetism and the hydrodynamic of the fluids. The phenomena of electromagnetism is by the Maxwell's equations in the form of

$$4\pi j = \frac{\partial \mathbf{E}}{\partial t} = c\nabla \times \ \mathbf{B} \tag{1.2}$$

$$\frac{\partial \mathbf{B}}{\partial t} = -c\nabla \times \ \mathbf{E} \tag{1.3}$$

$$\nabla.\mathbf{B} = 0 \tag{1.4}$$

$$\nabla.\mathbf{E} = 4\pi\sigma \tag{1.5}$$

with the electrical current density j, the charge density σ and the speed of light c. Replacing the electric field by

$$\mathbf{E} = -v \times \frac{\mathbf{B}}{c} \tag{1.6}$$

we get the induction equation of ideal MHD:

$$\frac{\partial \mathbf{B}}{\partial t} = \nabla \times (v \times \mathbf{B}) \tag{1.7}$$

These MHD waves depends on several plasma parameters, in particular the strength of the magnetic field.

There are three types of MHD waves in a magnetized fluid. The waves may propagate with or without compressing the plasma. The three types of waves are

- Alfven waves : This describes a linear wave with incompressible propagation along the magnetic field. It has a characteristic velocity called the Alfven velocity v_A. This wave is driven by the perturbations in the magnetic field lines. The magnetic tension acts inorder to straighten the distortions and acts as a restoring force for the curvature of the field.

- Slow magnetoacoustic waves : The slow MHD wave is one out of the two compressible magnetoacoustic modes which is excited but the changes in the plasma pressure and the magnetic pressure acting in opposition. Along the magnetic field lines, the slow mode wave propagates like an acoustic wave with velocities less than the sound and the Alfven speed. The slow magnetoacoustic wave can steepen into a slow mode shock which compresses and thus heats the plasma.

- Fast magnetoacoustic waves : The fast MHD wave is the second of the compressible magnetoacoustic modes. Just like the slow-mode wave, it also changes with the variation in gas and magnetic pressure but with the two interacting pressure forces in phase. The restoring forces for the magnetoacoustic perturbations are the pressure forces, gravity, and also the tension force of the magnetic field lines.

1.3.2 Plasma-β

In the solar atmosphere, the gas plasma is generally scattered with the magnetic fields. The β-value of a magnetized plasma quantifies the dominating atmospheric force. The plasma-β is defined as the ratio of the local plasma pressure p_{gas} to the magnetic pressure p_{mag} of the field configuration:

$$\beta = \frac{p_{gas}}{p_{mag}} = \frac{p_{gas}}{(B^2/8\pi)} = \frac{\rho/\gamma . c_s^2}{(B^2/8\pi)} = \frac{2}{\gamma} . \frac{c_{s^2}}{v_{A^2}} \approx \frac{c_{s^2}}{v_{A^2}}$$

(1.8)

with the magnetic field strength B, the plasma density ρ, the adiabatic γ, permeability of free space μ_0 (here 4π), the local speed of sound c_s and the Alfven velocity v_A.
In the case of high-β (Eq.1.3.2), the gas pressure of the plasma dominates the magnetic pressure. In the convection zone where $\beta \gg 1$, the magnetic fields are frozen in the convection. The solar convection zone and most parts of the photosphere feature a high plasma-β.
In the case of low-β, the magnetic pressure forces dominates the plasma pressure. As the convective pressure and plasma density decrease with altitude, the upper solar atmosphere (from the chromosphere to the corona) features a low plasma-β. If $\beta \sim 1$, transition level of the plasma-β, the magnetic and plasma pressure are in equipartition. Consequently, in this region the sound speed reaches the Alfven velocity. In the quiet solar atmosphere, the β- unity layer is located at chromospheric heights. Between the high-β and low-β domain, the effective mode mixing and conversion of fast and slow-mode waves occurs.

1.4 Chromospheric Jets and dynamic fibrils

The chromosphere which is considered to be in a highly dynamic state, varies on a time sale of few minutes or less. The dynamics in the magnetized regions associated with the magnetic network and plage is dominated by short-lived and jet-like features. Lot of names have been given to explain these chromospheric features. At the quiet-Sun limb, they are traditionally called spicules when observed in Hα appears as thin, elongated features that develop speeds of 10-30 km s^{-1} and reaches height of on average 5-9 Mm during their lifetimes of 3-15 minutes[98]. Their widths (0.2-1 Mm) and dynamics have been very close to the resolution limits of observations. As a result of this limitation, the superposition inherent in limb observations, and the difficulty associated with interpreting Hα data, the properties of spicules have not been very well constrained, which has led to a multitude of theoretical models. The Hα disk observations shows dark mottles in quiet-Sun regions which seem similar to spicules and usually appear in close association with small flux concentrations (and bright points) in the magnetic network that outlines the supergranular cells. There has been a long-standing discussion on whether spicules and mottles are the same phenomenon. There had been lot of discussion on this and it concluded that mottles are not the disk counterpart of spicules Grossmann-Doerth (1992)[99]. However, several groups have used more recent data to argue to show a close relation between mot-

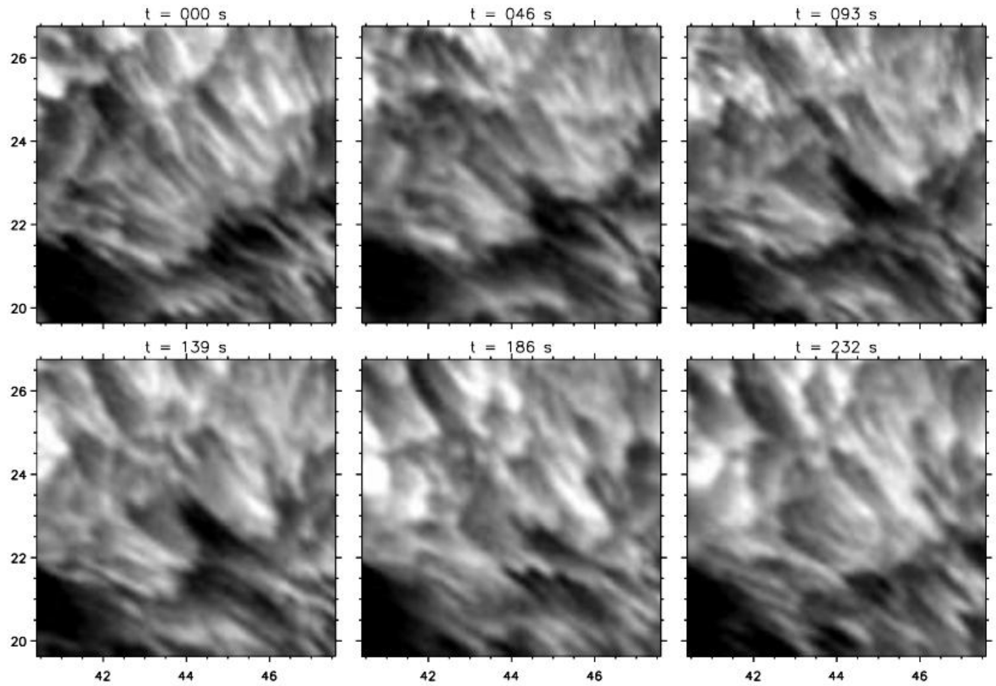

图 1.11: Snapshots in Hα line center that show the temporal evolution of a DF as it rises and retreats[11].

tles and spicules (Tsiropoula et al. 1994; Suematsu et al. 1995; Christopoulou 2000)[87,88,100]. Dynamic, jet-like features can also be seen in and around active region (AR) plage regions. These are shorter (1-4 Mm) and shorter lived (3-6 minutes) and appear to form a subset of what is called the active region fibrils. There are also fibrils that do not show jet-like behavior and are apparently low-lying, heavily inclined, and more static looplike structures connecting the plage regions with opposite polarity magnetic flux. The flows (up and down) from photosphere to chromosphere and the higher-layer corona show a variety of oscillation modes like three-minute, five-minute and seven-minute oscillations. Tian (2014)[101] first presented strong evidence related to the shock behavior of sunspot oscillations in the transition region (TR) and in the chromosphere based on IRIS (Infra-Red Imaging Spectropolarimeter) observations. The 5-minute oscillations happening over these sunspots have been studied extensively by Leighton (1962)[52] over a period of time and it has been found that there is a decrease in amplitude with height that is not easily detected in higher layers above the photosphere. Stangalini (2012)[77] said that the 3-minute oscillations could be due to the mode conversion of magnetoacoustic waves. Hale (1908)[102] demonstrated the fibrilar structure of the chromosphere reveals that magnetic fields play a significant role . The jet-like features which are also known as spicules, mottles and DFs are observed on the limb, QS disk and in ARs respectively.

1.5 Coronal loops

The existence and structure of coronal loops has been a mystery since long. As the plasma-β of the coronal magnetic field is low, hence it is expected to be force-free because of which the magnetic field occupies the entire space in corona. EUV observations reveals the coronal loops that are thin and have curved hot-plasma structures. Such EUV loops exist as discrete structures in the corona implying a part of coronal field lines to be filled with EUV-emitting plasma. It has been rather mysterious how the width of a loop varies little along it even though the forcefree field lines are supposed to diverge with height [103]. It is also a question how a loop can maintain a finite width despite the apparent excess of plasma pressure over its surroundings. For understanding the coronal loops more deeply, the magnetic twist appears to be an important element since it may be responsible for the coronal heating that maintains EUV emission as well as the constriction of loops [104–107]. Also, the twist of the loop is supported by earlier observations. The TRACE (Transition Region and Coronal Explorer) observations reported the wrapping of two bright EUV loops with a twist of less than one turn [108]. Chae et al. (2000) [106] reported the rotational motion of a loop around its axis from SOHO (Solar and Heliospheric Observatory) SUMER (Solar Ultraviolent Measurements of Emitted Radiation) observations may be considered as indirect evidence for magnetic twist. The other kind of indirect observational evidence came from the observation of kinked loops by Williams (2005) [109], which might have resulted from the kink instability that occurs when the magnetic twist of a flux tube exceeds a critical threshold. It is well known that the ARs have certain amount of magnetic helicity [110], a fraction of which exist in the form of the magnetic twist of coronal loops and the twist value of about 1.2π and (2-3)π has been reported by Aschwanden (1999) [111]. Recently, Chae and Moon (2005) [107], developed a magnetohydrostatic model of a twisted flux tube was developed and found that the magnetic twist of a loop is about 1.5π. This result is quite consistent with the theoretical result giving the stability of coronal loops against the kinking perturbation when the twist is smaller than a critical value of 2.5π to 4.8π [112,113]. To get the statistical distribution information of the twist, it is important to measure the magnetic twist of many loops using the same method. Magnetic reconnection play a major role in astrophysical plasma dynamics for the solar corona. This localized process converts magnetic energy into thermal and kinetic energies of plasma flows allowing a global change of the magnetic topology through an alteration of the field lines connectivity. They are clear observational evidences from X-ray pictures taken by the Yokhoh satellite that a reconnection process takes place during the solar flare phenomenon [114], and that it provides a substantial heating of the solar corona [115,116]. The basic physics of the magnetic reconnection requires the presence of a thin region called an X-line where the magnetic field changes orientations. A plasma flow towards the X-line is also necessary to squeeze sideways the fluid and maintain a current sheet structure. In a weakly resistive plasma (like the solar corona), the resistive diffusion is important only in this thin internal region where large magnetic gradients are present. Since the pioneering work on the reconnection phenomenon, numerous analytical and numerical results have been obtained in hot plasmas and more specifically in the solar corona context [117–119]. Depending on the geometry, the physical parameters, and the boundary conditions, many different regimes qualified as slow or fast have been then identified. However, Priest (1997) [119] has carried out most of these studies in two dimensions, and the three dimensional (3D) reconnection process has been considered .

1.6 Motivation for the current studies

It is known that the propagation of RPWs could be seen in the chromosphere upto a height of about $\sim 15''$ which is ~10,000 km from the edge of the boundary of the penumbra. This gives a view that the quiet sun *p*-mode oscillations dominates and conquers the remaining RPWs signatures. Though the running waves were observed in the umbra earlier but it was not related to the waves in the penumbra. Not just in the umbra, the running waves were also observed in the pores. In this way, the origin of RPWs has been under discussion since their discovery. Many groups of people consider them to be the trans-sunspot waves of completely chromospheric origin or they are considered to be the chromospheric signature of upwardly propagating *p*-mode waves. A sequence of studies have been performed by using multiwavelength imaging and doppler velocity measurements in order to examine the phase lag between the oscillations of sunspot at the different layers of the lower atmosphere of the sun. It has been quite interesting to know about the compressional waves that propagate upwards and which finally develops into shock. The concept of shock driving has been studied earlier based on simulations of spicules and mottles in quiet regions and dynamic fibrils in ARs and is observationally supported by the pattern of motion detected in individual mottles and the dynamic fibrils. One of the known patterns of chromospheric motion inside the sunspots are umbral oscillations and running penumbral waves. This relation motivates us to look upon the oscillations in sunspot and connect it with the fibrils that originates from the sunspot and propagates through penumbra and superpenumbra.

It has been reported recently by Chae et al. (2014) [120] from the observational results that the chromospheric jets, specifically the superpenumbral fibrils, outside of a sunspot, as well as penumbral waves, are closely related to the oscillations inside the sunspot. But how are these fibrils related to the sunspot oscillations and what drives the fibrils? We have looked into such fibrils and found that these are driven by the oscillations in the sunspot. The umbral oscillations has been looked into and studied its relation with the RPWS. The emergence of RPWs have been studied and presented in Chapter 4 with the observational data and analysis description in chapter 2 and chapter 3 respectively. The dynamic fibrils originating from the sunspot have been studied further to relate it with the sunspot oscillations and presented in Chapter 5. The following chapters discuss the relation between the sunspot oscillations and the dynamic fibrils. The major results of these investigations have been summarised in Chapter 7. Some of the possible future prospects of these studies are also outlined in this Chapter.

第二章 Observational Data

We have chosen two main sunspots of NOAA ARs 12127 and 12132 for this study. To cover different heights from photosphere to Corona we obtained the data in different wavelengths using ground and space based facilities. The details of facilities, observations, data collection and processing, and adapted methods in analysis are described below.

2.1 Telescopes and Instruments

The data in TiO band, Hα, and He I are obtained from GST (Goode Solar Telescope). The images of 304 Å are taken from AIA on board SDO. To study the effect of the inclination of magnetic field on the wave period, we used vector magnetograms from SOT (Solar Optical Telescope) on board HINODE and HMI (Helioseismic and Magnetic imager) on board SDO (Solar Dynamic Observatory). Data collected from different instruments were used to address the problems in our work. Important information on these facilities are given in this section.

2.1.1 BBSO

2.1.1.1 Goode Solar Telescope

Goode Solar Telescope (GST) is a 1.6 m clear aperture solar telescope in BBSO (Big Bear Solar Observatory) which had its first light in January 2009. The first science grade data was obtained in the Summer of 2009 and first data corrected by adaptive optics (AO) was in the Summer of 2010. The GST is the first facility-class telescope, dedicated for solar observations, built in the United States in a generation. The GST[1] is a modern telescope with off-axis 1.6-m mirror (Goode et al., (2010)[121]; Cao et al. (2010)[2]) that offers a significant improvement in ground-based high angular resolution and polarimetric capabilities. The telescope is configured as an off-axis Gregorian system consisting of a parabolic primary, prime focus field stop and heat reflector (heat-stop), and an elliptical secondary. For more details see chapter 3.

2.1.2 SDO

Solar Dynamics Observatory (SDO)[12] is the first mission launched under NASA's Living With a Star (LWS) program, a program designed to understand the causes of solar variability and its impacts on Earth. It was launched from

[1] http://www.bbso.njit.edu/nst_project.html

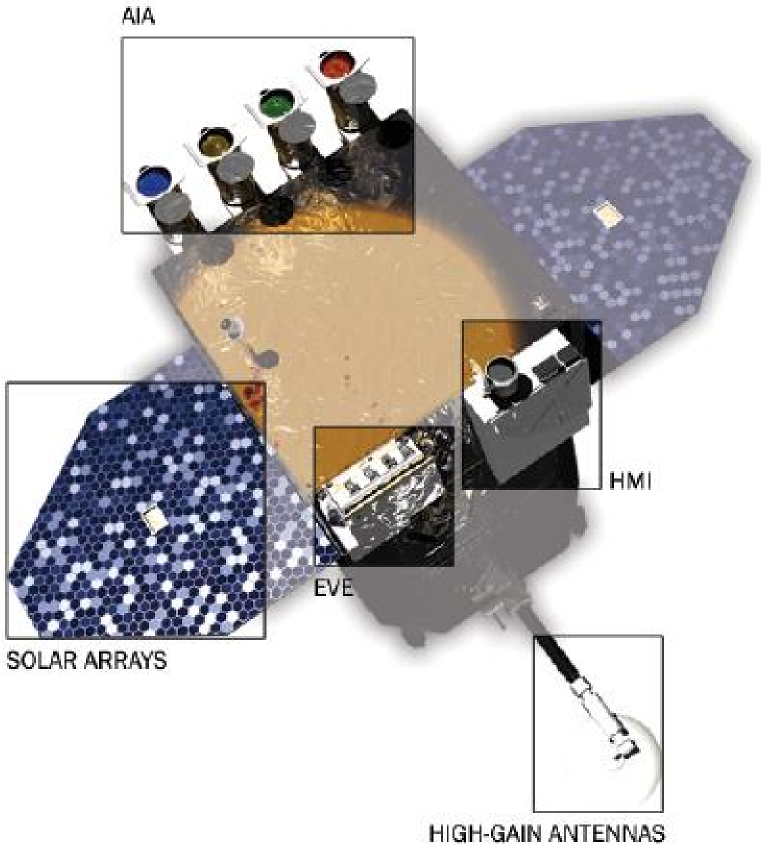

图 2.1: The SDO spacecraft with all the three instruments onboard high-lighted. The high-gain antennas and the solar arrays can also be seen[12].

Kennedy Space Centre in Florida on February 11, 2010. The main goal of SDO is to understand the Suns influence on Earth. Also, near-Earth space by monitoring the solar interior and different layers of its atmosphere with high spatial and temporal coverage, in multi wavelengths simultaneously. The requirement of high spatial and temporal coverage implies a large volume of data, which led to place the satellite in an inclined geosynchronous orbit that allows the contact with a single, dedicated ground station for a continuous downlink. The orbit is inclined at 28.5° with nearly continuous view of the Sun, apart from two eclipse seasons (due to shadow of Earth) per year. During this time there will be daily interruptions in the observations. In addition, three more brief interruptions every year due to Lunar transit.

There are three instruments onboard SDO; the Atmospheric Imaging Assembly (AIA) built in partnership with the Lockheed Martin Solar & Astrophysics Laboratory (LMSAL), the Helioseismic and Magnetic Imager (HMI) built in partnership with Stanford University, and the Extreme ultraviolet Variability Explorer (EVE) built in partnership with the University of Colorado at Boulder's Labo-

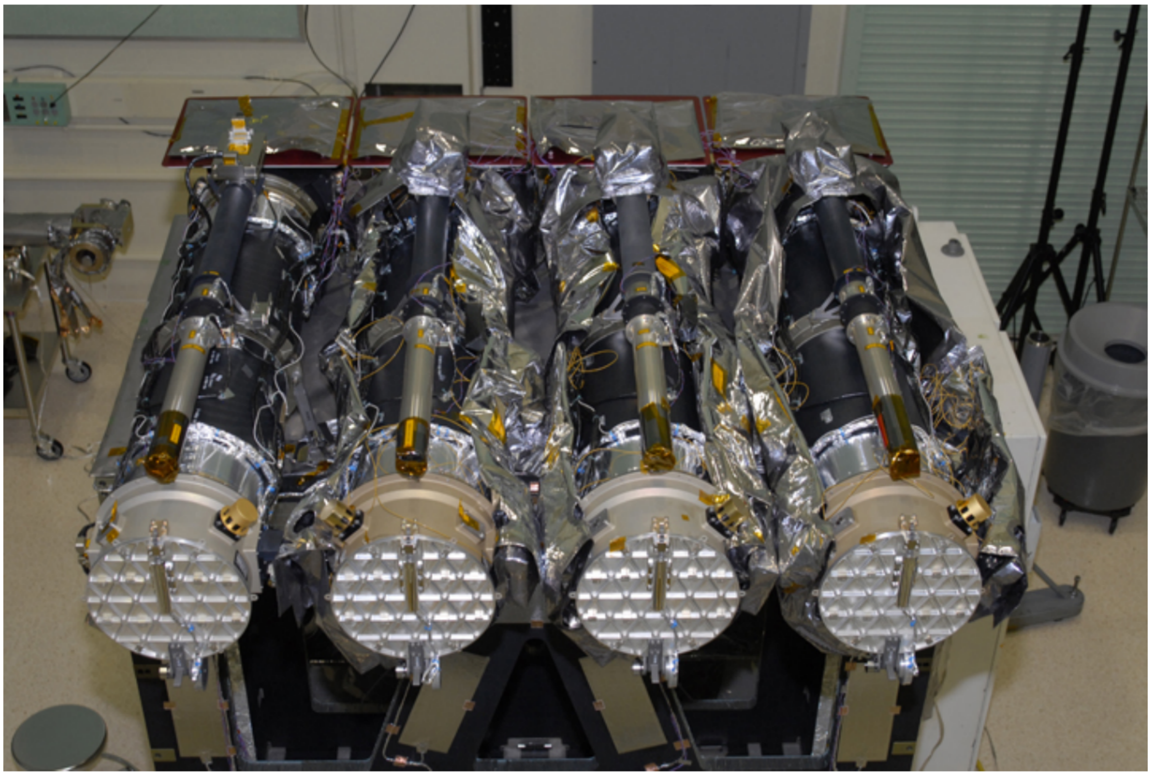

图 2.2: The four AIA telescopes mounted on the SDO spacecraft during integration at NASA's Goddard Space Flight Centre[1].

ratory for Atmospheric and Space Physics (LASP). Figure 2.1 shows the SDO spacecraft with different instruments onboard highlighted. This observatory started its science operations on May 1, 2010 with a planned lifetime of 5 years. EVE measures the solar spectral irradiance in 1 to 1050 Å wavelength range which is the most variable and unpredictable part of the solar spectrum. It also measures the irradiance of Lyman-α at 1216 Å, the single brightest line in EUV. Since the data from AIA and HMI are used extensively in this thesis work, they are described below in detail.

2.1.2.1 Atmospheric Imaging Assembly

Atmospheric Imaging Assembly (AIA)[1] is an array of four telescopes that captures the solar atmosphere in 10 different wavelength bands. Figure 2.2 show these four telescopes with their individual guide telescopes mounted on the SDO spacecraft during integration at NASA's Goddard Space Flight Centre (GSFC). The primary aperture of each telescope is 20 cm, which image the full disk over a 4k $\times$ 4k CCD at a spatial resolution of $\sim$0.6 Å per pixel. The FOV is circular with diameter of 41$'$ that allows the observations up to 0.28 $R_\odot$ above the limb. A set of seven EUV and three UV-visible channels exists in it. Six of these seven EUV channels are to observe ionized Fe to study temperature diagnostics of the solar

表 2.1: The list of seven EUV and three UV-visible channels used in AIA. The region of atmosphere that can be observed and their characteristics temperatures are listed. Adapted from Lemen et al. (2012) [1]

Channel	Primary ion(s)	Region of atmosphere	Char. log(T)
4500 Å	continuum	photosphere	3.7
1700 Å	continuum	temperature minimum, photosphere	3.7
304 Å	He II	chromosphere, transition region	4.7
1600 Å	C IV+cont.	transition region, upper chromosphere	5.0
171 Å	Fe IX	quiet corona, upper transition region	5.8
193 Å	Fe XII, XXIV	corona and hot flare plasma	6.2, 7.3
211 Å	Fe XIV	active-region corona	6.3
335 Å	Fe XVI	active-region corona	6.4
94 Å	Fe XVIII	flare corona	6.8
131 Å	Fe VIII, XXI	transition region, flaring corona	5.6, 7.0

atmosphere from 1 MK to 20 MK. For all the ten channels, the primary ion(s) responsible for the emissivity in each channel. The regions of atmosphere that can be observed using these different channels and their characteristic temperatures are listed in Table 2.1. Three out of the four telescopes observes the Sun in six channels, while the fourth telescope observes C IV (near 1600 Å) along with the 171 Å channel. It also has a filter that observes in the visible around 4500 Å to enable co-alignment with images from other telescopes. The temperature response functions of the seven EUV channels, the arrangement of telescopes, and their observing wavelengths as viewed from the Sun are shown in Figure 2.2. The cadence at which images are captured in the standard observing mode is 12 s[122]. However, AIA has the capability to readout small regions of interest, which reduces the cadence up to 2 s for selected wavelength channels to meet specific science objectives such as flare studies.

2.1.2.2 Helioseismic and Magnetic Imager (HMI)

The Helioseismic and Magnetic Imager (HMI) [123] is a solar spectro-polarimeter onboard the Solar Dynamics Observatory (see Figure 2.1). It was designed as a full-disk solar imager to measure intensities, velocities and magnetic fields in the solar photosphere. HMI was built at the LMSAL (Lockheed Martin Solar and Astrophysics Laboratory) which was operational since 2010. The instrument is attached to the telescope which has primary lens with a diameter of 0.14 m and an effective focal length of 4.95 m. HMI observes the photospheric Fe I spectral line at 6173 Å which is sensitive to the magnetic Zeeman effect with an effective Lande-factor of $g_{eff} = 2.5$. A dedicated optical setup is used to filter six wavelength positions across the spectral coverage (6.9 pm spacing), which consists of a front-window filter with 50 Å bandpass, a blocking filter with 8 Å bandpass, a Lyot filter with a single tunable element and two tunable Michelson interferometers. The first one filters a broad spectral band, whereas the second one transmits a narrow wavelength position. A set of tuning waveplates is integrated to perform polarimetric observations. The final spectro-polarimetric signal is divided by a beam splitter and recorded in two CCD cameras having 4k $\times$ 4k pixels each, at every 3.75 s. The size of solar disk at the detectors is 4.6 cm. The images are recorded with a scale of $0.5''$/pixel to approach the spatial resolution of $1''$. The first camera measures both left and right circular polarization at the six wavelength positions on an overall scan time of 45 s. With this measurements, full-disk solar maps are created for the continuum intensity, Doppler shifts translated into line-of-sight velocities (Dopplergram), and line-of-sight magnetic fields (LOS magnetogram). The second camera measures the full Stokes vector at the same wavelength positions. To increase the accuracy, the Stokes vectors are averaged for a time span of 12 minutes. The inversion uses the Zeeman effect to produce full-disk vector magnetograms at the temporal cadence of 12 minutes. Since whole community has access to the HMI products, the data can serve as context information for any co-temporal observation made with any other solar telescopes.

第三章 BBSO/GST observations and Data analysis

Big Bear Solar Observatory has the worlds largest solar telescope, the off-axis Goode Solar Telescope (GST) of 1.6 m aperture is NJIT (New Jersey Institute of Technology's) one of the ground based observatories (shown in Figure 3.1). It is the first of a new generation large aperture solar telescope. The GST has a resolution of 0.06″ at 0.5 μm and 0.2″ at 1.56 μm. The primary mirror (PM) of GST is 1.7-m with a clear aperture of 1.6-m. The focal ratio of the PM is f/2.4, and the final ratio is f/52. The 100 circular openings in the field defines a 70″ × 70″ maximal square field of view (FOV). The working wavelength range covers from 0.4 to 1.7 μm. An off-axis design was chosen for optimizing the reduced stray light, since there is no central obscuration to degrade the telescope modulation transfer function (MTF) at high spatial frequencies. The wavefront sensing system for alignment and for the PM active optics resides just before M3. Also, resides here the polarization modulator. Advanced design of modulator helps to obtain vector magnetograms, which were never possible with the old 0.6 m telescope. The reason, in part, could be there were always many (oblique) mirrors between the sunlight and the modulator. The GST has a fully operational, nearly achromatic AO system on a vertical bench in the Laboratory for diffraction limited imaging. Early observations have been concentrated in the near infrared (NIR) region due to limitations in AO system, which are now being solved by larger format of deformable mirrors (DMs). A sample Hα image from GST in Figure 3.2 reveals the dynamical layer overlying the surface region. Most apparent are the long dark streaks, so-called "jets" arising from the bright magnetic regions on the edge of the penumbra. Its post-focus instrumentation consists of a broadband filter image (BFI), visible imaging spectrometer (VIS), near-infrared imaging spectropolarimeter (NIRIS), fast-imaging solar spectrograph (FISS), and a cryogenic infrared spectrograph (CYRA). Also on the site, exists an H-alpha full-disk imager which is part of the Global H-Alpha Network and a Global Oscillations Network Group (GONG) station.

Broadband filter imager (BFI): This imager records continuum context data over an AO-corrected field using a high speed 2048×2048 CCD camera. Three bands are currently used: G-band centering at 4305 Å with 5 Å bandpass. The field of view and image scale are of 55″ and 0.027″/pixel, respectively . Red continuum at 6684 Å with 4 Å bandpass and TiO band centering at 7057 Å with 10 Å bandpass. The field of view and image scale are of 70″ at 0.034″/pixel. Filtergrams are typically taken in short bursts: 100 frames for every 15 s, and processed via speckle reconstruction to achieve diffraction-limited images. The resolutions achieved are of 0.06″ in G-band, 0.09″ in TiO and red continuum.

Visible Imaging Spectrometer (VIS) The purpose of VIS is to provide spectral diagnostics of solar features at the diffraction limit of the telescope. VIS currently adapts a single Fabry-Perot etalon to produce a narrow 0.07 Å bandpass over a 70″ circular field of view. The wavelength range is tunable from 5500 to 7000 Å. A future plan is underway to upgrade VIS to dual-etalon system. The spectral lines available now includes Hα, Fe I at 6300 Å, and Na I D2 at 5890 Å. He I D3 line at 5876 Å will be added soon. The image scale is 0.034″/pixel, and typically 11 line positions are sampled in 15 s. However, the number of line positions and corresponding time resolution is a tunable parameter. Bursts of typically 25 frames are used for speckle reconstruction at each line position.

Near Infra-Red Imaging Spectropolarimeter (NIRIS) The dual Fabry-Perot etalons are used in NIRIS that provides an 85″ circular field of view. Recently, a new Teledyne camera with a 2024 × 2048 HgCdTe and closed-cycle He cooled IR array was introduced to record the data. The system utilizes only half the chip to capture two simultaneous polarization states side-by-side with each 1024 × 1024 pixels in size. It is providing an image scale of 0.083″/pixel. In future, the other half of the chip is used for two out-of-focus images to be used for phase-diversity correction. The primary lines used by NIRIS are He I multiplet at 10830 Å with bandpass of 0.05 Å and the Fe I doublet at 15650 Å doublet with bandpass of 0.1 Å. The polarimetry is operated using a rotating waveplate that samples 16 phase angles at each line position. For a single full spectroscopic measurement including full-Stokes parameters (I, Q, U and V), more than 100 line positions are used at a cadence of 10 s. The inversion of these data to provide magnetograms and other spectral diagnostics are currently under development. The system can also be operated in a fixed-phase-angle, dual-polarization mode that would allow speckle reconstruction of I and V images for diffraction limited line-of-sight magnetic field diagnostics.

Fast-Imaging Solar Spectrograph (FISS) FISS was designed to study fast dynamics of solar features at moderate spatial resolution and high spectral resolution. FISS is a scanning Echelle-type spectrograph which was made through a collaboration between two Korean groups, Seoul National University (SNU) and Korean Astronomy and Space Institute (KASI). FISS observations are mostly dedicated for spectral lines of Ca II H and K lines near 8540 Å and Hα . Interestingly, both the spectral regions can be observed simultaneously using a dual-camera system. The spectrograph slit is 40″ long covering field of view of 40″ × 60″ which is typically scanned in 10 s. The Hα camera has a CCD size of 512 × 512 and the Ca II camera is with 1004 × 1000 pixel CCD. The width of slit is 32μm that corresponds to a spatial sampling of 0.16″. The spectral sampling at Hα and Ca II are typically 0.019 Å and 0.025 Å, respectively, provides a spectral resolution

表 3.1: Available observing wavelength of interest at BBSO. Adapted from Cao et al. (2010)[2]

Wavelengths	Bandpass	Solar features
430 nm	5 Å	G-band bright points
656 nm	0.25 Å	Filaments, spicules, jets, flares..
706 nm	10 Å	Granulations, sunspots....
1.083 μm	0.25 Å	Coronal holes...
1.6 μm	2.5 Å	The deepest photosphere
2.2 μ	5 Å	Cold clouds in the chromosphere

of 0.05 Å and 0.06 Å at a resolving power of R=$\lambda/\Delta\lambda$=1.4×10^5.

3.0.2.3 Hα Full-Disk Imager

The Hα full-disk telescope has aperture size of 10-cm refractor. It is equipped with a Zeiss Lyot 0.25 Å bandpass filter with a tunable range of ± 3 Å. The size of detector is 2048 × 2048 pixels with 12-bit processor. The spatial scale is about 1″/pixel. The exposures given are typically 30 ms, and frames are taken at a cadence of 1 frame/minute. However, during flares the cadence can be manually increased to 1 frame/15 s. The images are used in real time which enables to aid in target selection of the GST. Also, used for context for the high-resolution GST data. In addition, the station is part of a world-wide network called the Global Halpha Network (GHN) comprising BBSO, Kanzelhohe Solar Observatory in Austria, Catania Astrophysical Observatory in Italy, Meudon and Pic du Midi in France, Huairou and Yunnan Observatories in China, and the Uccle Solar Equatorial Table in Belgium.

3.0.2.4 Global Oscillation Network Group station

GONG is a network of six identical instruments located at Big Bear Solar Observatory (California), Learmonth Solar Observatory (Australia), Udaipur Solar Observatory (India), Observatorio del Teide (Canary Islands), Cerro Tololo Interamerican Observatory (Chile), and Mauna Loa Observatory (Hawaii). A description of the instrumentation and capabilities of GONG is given in the National Solar Observatory summary document.

The available wavelengths needed for specific observations depending on the line of interest are listed in Table 3.1 and Table 3.2.

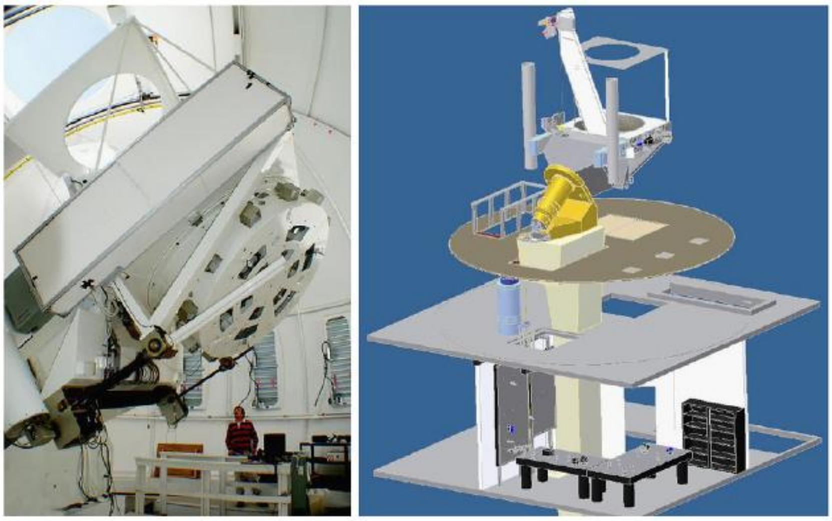

图 3.1: Left picture shows the 1.6 m off-axis GST with the primary mirror cell shown in the foreground. The design was driven by competing needs for rigidity atop the secondary mirror tower and an un-obscured light path throughout the telescope. Right schematic shows the full optical path through the GST with the bottom floor housing all instruments that are fed light from the AO.

3.1 Observations and Data processing

We performed the High-resolution observations using Goode Solar Telescope [2] operating at Big Bear Solar Observatory (BBSO) on two main sunspots of NOAA ARs 12127 (sunspot 1, located at S09E08 on 2014 August 1) and 12132 (sunspot 2, located at S19E04 on 2014 August 5). Inorder to investigate the umbral oscillations in sunspot 2 at different solar altitudes, in addition to the Hα data, we also used images of the narrow band (band-pass: 0.5 Å) of He I 10830 of the GST with a pixel size of 0.078″ and time cadence of 15 s as observed on August 5, and the images of 304 Å taken by the SDO/AIA. These lines allow us to study the

表 3.2: NIR bands of interest for CYRA at BBSO. Adapted from Cao et al. (2010) [2]

Spectral Lines	Magn.Sensitivity(λ_{geff})	Region
Ti I 2.231 μm	5578 nm	Photosphere
Fe I 4.064 μm	5080 nm	Photosphere
Si I 4.143 μm	9321 nm	Photosphere
Ca I 3.697 μm	4067 nm	Chromosphere
Mg I 3.682 μm	4307 nm	Chromosphere
CO 4.6 μm	Molecular band	Chromosphere

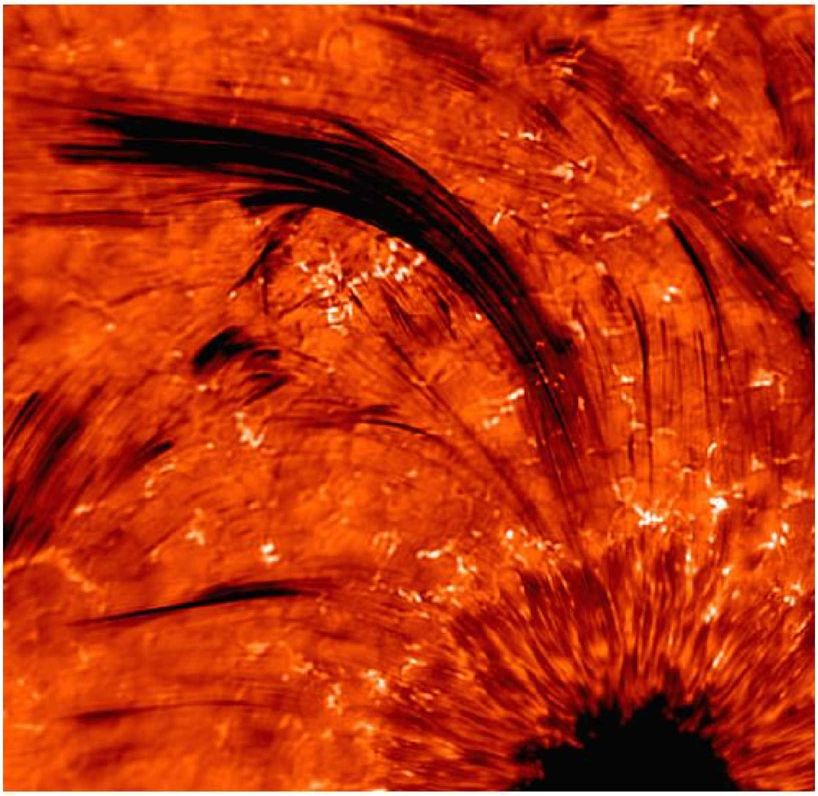

图 3.2: Off-band Hα image of a sunspot revealing the dynamical layer overlying the surface region above a sunspot.

umbral oscillations in the chromosphere (Hα line), in the upper chromosphere (He I 10830 Å line), and in the transition and lower corona region (304 Å line). For studying the spiral structures of wavefronts in the sunspot, the observations were carried out at 18:19 UT for a duration of 60 minutes. We used the broad-band filter imager of GST, with FOV of $70''$ at $0.034''$ pixel^{-1} image scale to acquire continuum photospheric images every 15 s in TiO band (705.7 nm, 10 Å bandpass). We also employed VIS of GST that has a single Fabry-P'erot etalon to produce a narrow 0.07 Å bandpass over a $70''$ circular FOV at $0.034''$ pixel^{-1} image scale. The chromospheric images were thus acquired every 23 s by scanning the Hα spectral line from its blue wing -1 Å to red wing $+1$ Å with a step size of 0.2 Å. In addition, we also acquired the simultaneous space observations taken in 304 Å line (formed in the transition and lower corona) of the AIA on SDO [1]. We used the first image at $\mathrm{H}\alpha - 1.0$ Å as a reference to align all the other images at the same passband. In this procedure, the relative shifts to the first image are kept, and are then used to align the Hα images in the other passbands (all the images observed every 23 s are assumed here to be already co-aligned). Similarly, with the reference image, it is convenient to co-align it with the images of other instruments. The relative shifts were recorded, and used to register the images in the other passbands of Hα. Similarly, using the reference image, alignment was easily executed for TiO images and one white-light image at 17:15 UT taken with the Helioseismic and Magnetic Imager[124] on board SDO. The aligned white light image was then used to co-align the 304 Å images. Finally, Fast Fourier Transform (FFT) was applied to the time-series images to generate the filtered component images, either in phase speeds of $v_{ph} > 4$ km s^{-1}[125] or centering at certain frequency (e.g., 3.33 mHz, 5.55 mHz, etc).

3.2 Data Analysis

3.2.1 Fast Fourier Transform

To measure the oscillation period, the time profiles are transformed with Fast Fourier Transform (FFT) function using IDL. FFT algorithm computes the discrete Fourier transform (DFT) of a sequence, or its inverse. Fourier analysis converts a signal from its original domain (often time or space) to a representation in the frequency domain and vice versa. In chapter 4 we show the FFT results where every power spectrum of the resulting transformation has one peak that appears as a spike. FFT is a convenient method to measure the periods of the umbral and penumbral oscillations, however the significance level of the measured periods is not directly given in the analysis.

3.2.2 Phase speed filter

A filtering method working on the frequency wavenumber (ω - k) domain is employed in order to extract the wave signals of interest from the analyzed temporal sequences of Hα images. A three-dimensional time-space matrix generated by one image sequence is transformed to the $\omega - k$ domain using the three-dimensional Fourier transform. The wave phase velocity, v, is equal to the ratio of ω and k in the $\omega - k$ domain. However, as umbral waves are the main concern for our study, we concentrate more on the low-pass filter and apply it to all the temporal sequences of Hα images from -1 to $+1$ Å off the line center. After a few comparisons, we see that the waves are clearly visible in the filtered images at the blue wing 0.4 Å as seen in Figure 3.3. Therefore, most of our investigation lies at this passband in our analysis.

$$H^{low}(v, v_c) = \frac{1}{1 + [\frac{v}{v_c}]^{2n}}, \tag{3.1}$$

where $v = w/k$, the phase-speed, v_c is the cut-off speed, and n is the order. Similarly, the high-pass one is given by

$$H^{high}(v, v_c) = \frac{1}{1 + [\frac{v_c}{v}]^{2n}}. \tag{3.2}$$

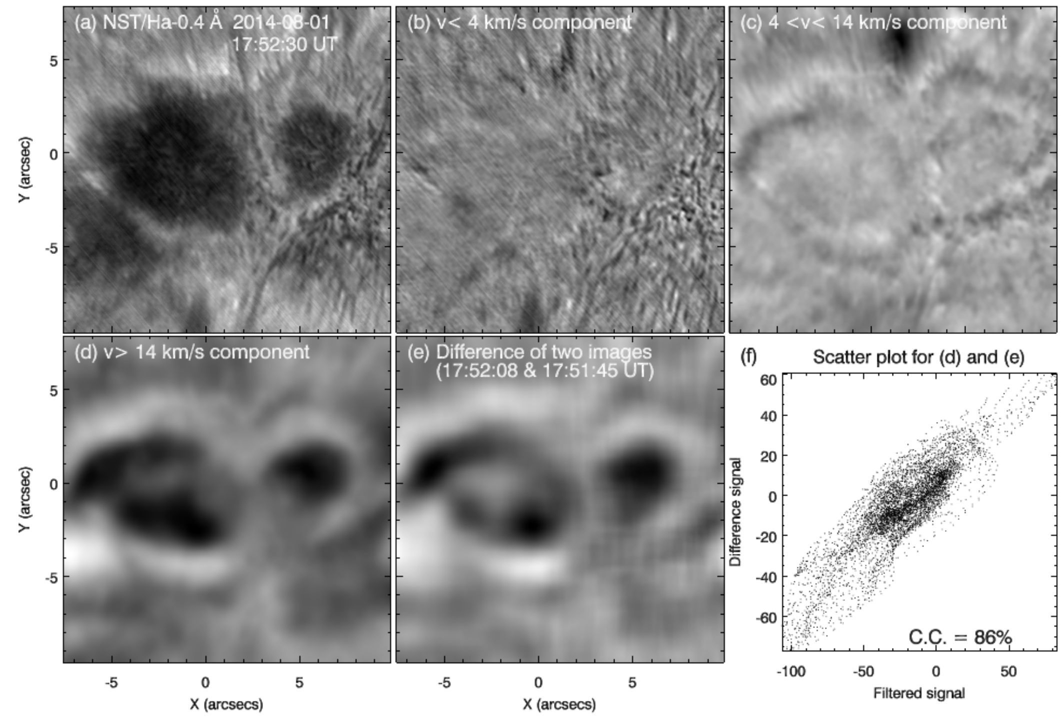

图 3.3: Test on the phase-speed filtering method with the observed data. Panels (a)-(d) in order: An original H$\alpha - 0.4$ Å image and its filtered components with speeds of $v < 4$, $4 < v < 14$ and $v > 14$ km s^{-1}, respectively. Panel (e): A difference image of the two observed ones at 17:52:08 UT and 17:51:45 UT. Panel (f): Scatter plot of the filtered and the difference signals.

第四章　Emergence of Running Waves

The running penumbral waves are the line-of-sight (LOS) velocity wavefronts in the chromosphere above sunspot penumbrae which shows expansion outward from the umbrae. It is important to study the origin of these waves and analyse it based on its emergence and further propagation. Intensity and velocity observations in various spectral lines have revealed the existence of 5 and 3-min oscillations (Thomas 1985; Lites et al. 1992; Staude et al. 2002; Bogdan et al. 2006)[33,57–59] in the umbral photosphere[60] or chromosphere[55,61]. The 5-min oscillations are predominantly a photospheric phenomenon. Their amplitude decreases with increasing height and they can hardly be detected in the upper chromosphere and transition region. On the other hand, the oscillatory power in the 3-min band shows a dominant peak in the sunspot chromosphere[62,63] and in the transition region between the chromosphere and the corona[64]. In the next section, we concentrate on the chromospheric umbral oscillations and the running waves associated with them. There are several theoretical models for the nature of the 3-min umbral oscillations. It was proposed by Thomas (1982)[126] that the oscillations are driven by a resonance of fast magnetoacoustic waves, located in the photosphere and subphotospheric layers, that are excited by overstable convection (a photospheric resonator).

4.1　AR NOAA 12127 and 12132

The GST observations were performed on the sunspots of NOAA ARs 12127 (sunspot 1, located at S09E08 on 2014 August 1) and 12132 (sunspot 2, located at S19E04 on 2014 August 5)(see Figure 4.1). The data on sunspot 1 were taken at 17:15 UT - 17:55 UT, and the data on sunspot 2 at 18:20 UT - 19:20 UT. Chromospheric images were acquired every 23 s by scanning of the Hα spectral line from the blue wing -1 Å to the red wing $+1$ Å with a step of 0.2 Å. The map of sunspots in TiO band of selected ARs are observed and shown in Figure 4.1 (a). The corresponding magnetic field inclination map is shown in Figure 4.1 (c). The range of magnetic field inclinations (15°, 35° and 45°) are indicated by different contours. These range of inclinations are very helpful in understanding the variation of strength of oscillaions umbral center to the boundary of sunspot umbra.

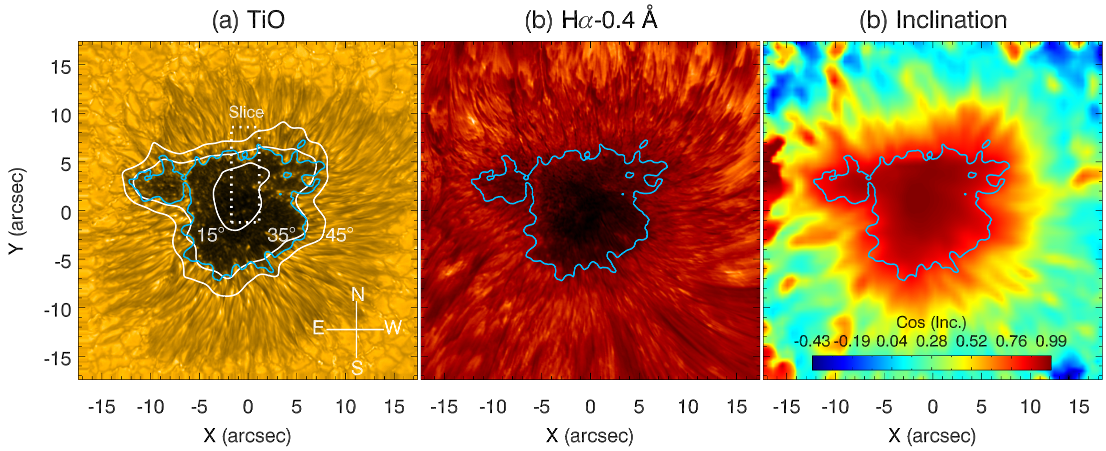

图 4.1: Sunspot in active region NOAA 12132 on August 5, 2014. (a) is a TiO image, box marked by dotted lines is selected which has been studied later. White contours represent the inclinations of 15°, 35° and 45° and blue contour in (a)-(c) denotes the umbral boundaries (45% of the maximum intensity). (b) is a $H\alpha - 0.4$ Å image. (c) is a field inclination image.

4.2 5-min oscillations at different heights

The oscillatory motions in sunspots are usually measured as Doppler shifts which could either be of spectral lines with or without the Zeeman effect Lites (1992)[33]. The periods of 5 min in the layers of photosphere and of 3 min in the layers of chromosphere has been found earlier. We looked into the oscillations of sunspots in various bands (passbands of TiO, $H\alpha = -1.0, -0.8, -0.6, -0.4, -0.2,$ 0.0 Å and 304 Å) as seen in Figure 4.2 to see how the strength of the oscillation power varies with distance. As could be seen from Figure 4.2 (a) and (b) that the power is much weaker in the sunspot than in the quiet Sun at the photosphere. But still the power in penumbrae becomes stronger as the height increases (see Figure 4.2 (c)-(e)). It has been known that the resonant oscillations exist inside the sunspot, basically inside the sunspot penumbra as said by Zhao (2013)[96]. We make a circular slit as shown in Figure 4.2 to see how the distribution of power is, and make an the intensity curve for TiO and $H\alpha - 0.4$ Å (see Figure 4.3) which gives an indication that there is a little higher concentration of power along the superpenumbral fibrils. A figure simlar to Figure 4.2 is plotted for high frequency oscillations in the range of 1.7-3.8 min (See Figure 4.4). Inspite of all this it has not been possible enough to confirm the existence of 5-min oscillations in the umbra of chromosphere (see Figure 4.2 (d)-(g)).

Figure 4.5 displays the power spectra of oscillations in the sunspot averaged over some circular slits with inclination in the range of 5° interval between 0° and 35° (e.g. 0°-5°, 5°-10°, upto 30°-35°) in the passband of $H\alpha - 0.4$ Å (top

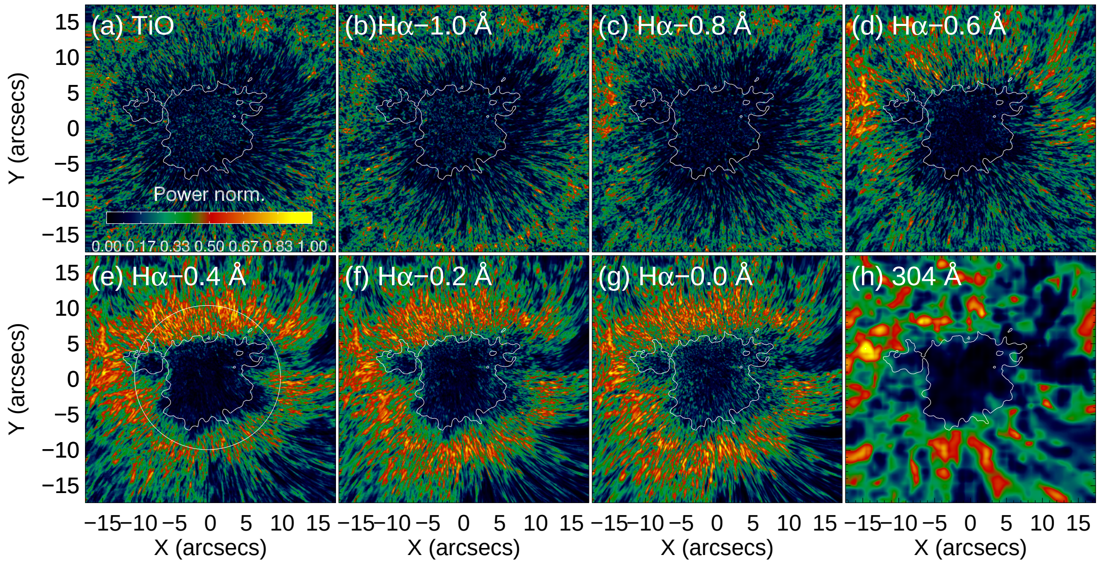

图 4.2: Power maps of the sunspot. (a)-(h) are spatial distribution of the normalized Fourier power for 3.8-8.0 min oscillations taken in the indicated passband. Umbral regions of sunspots are shown in white contours (see Figure 4.1).

panel), and averaged over a circular slit with 0-15° inclination in the passbands of TiO, H$\alpha - 1.0, -0.8$, ... and 304 Å (bottom panel). The noise in the data is removed by performing numerical differentiation on all time series of intensity. We arbitrarily take 3.8 min as the cut-off point of 3-min and 5-min band oscillations. In Figure 4.5 (a), 5-min oscillations show their strongest signal appearing in the inclination range of 30°-35°, which is close to umbral boundaries (see Figure 4.5). Subsequently, they decrease while approaching the umbral center and are nearly evanescent in the range of 15°-20°. It is quite possible to estimate the height to which oscillations propagate by using the method employed by Reznikova et al. (2012)[127] and Reznikova et al. (2014)[127], where they take the cutoff frequency of compressible acoustic waves in the form,

$$f_c = \frac{g\gamma}{4\pi c_s} = 1.28 g_0 cos\theta T_{min}^{-0.5}[mHz] \tag{4.1}$$

where $g_0 = 274$ ms^{-2}, $cos\theta = 1$ in umbral center, and T_{min}=temperature in the temperature-minimum layer and then calculate the cut off frequency and estimate the height of propagation.

Figure 4.5 (b) show 5-min oscillations are stronger at the formation heights of TiO and H$\alpha - 1.0$ Å. However, they become nearly invisible at the formation height of H$\alpha - 0.8$ Å. We divided the power spectra in Figure 4.5 (a) and Figure 4.5 (b) into two periodic ranges, $1.7 < P < 3.8$ min (short) and $3.8 < P < 8$ min (long), and the average power in the two ranges are shown in Figure 4.6. The variation in power with inclination is plotted in Figure 4.6 (a). For the curve

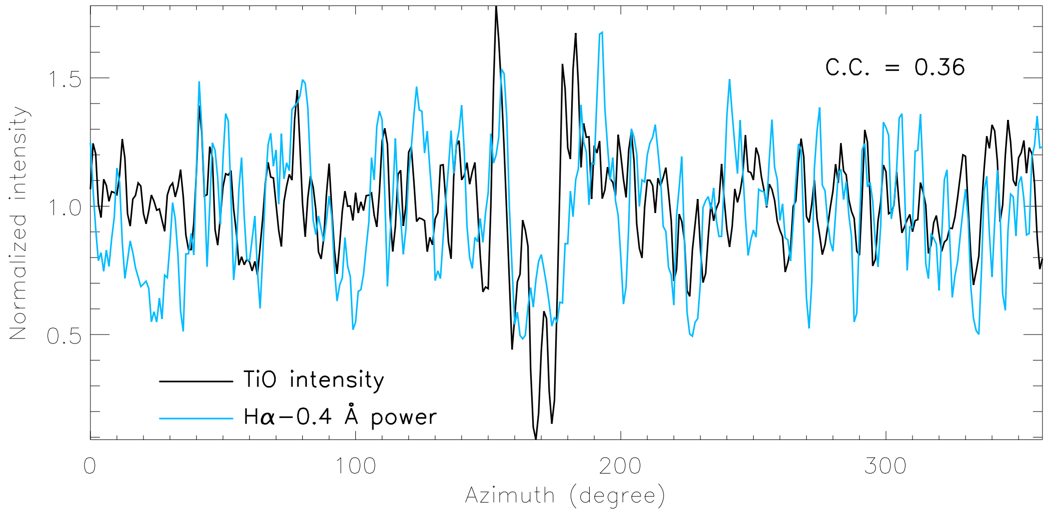

图 4.3: The TiO intensity and Hα − 0.4 Å oscillations power averaged over the circular slits shown in Figure 4.2.

of 3.8-8 min, the power increases exponentially with inclination in the range of $\sim 15-36^\circ$. Figure 4.6 (b) demonstrates the variation in power with height. For the 3.8-8 min curve, it falls off exponentially with increase in height, and fades out while approaching the formation height of Hα − 0.4 Å. Generally, it is less than 5% for the transmission rate of 5-min oscillation power from TiO to H$\alpha - 0.4$, -0.2 and 0.0 Å. Thus, it seems no 5-min p -mode waves can propagate vertically from photospheric to chromospheric umbra (e.g., within 15° inclination range).

4.3 Time-distance diagram

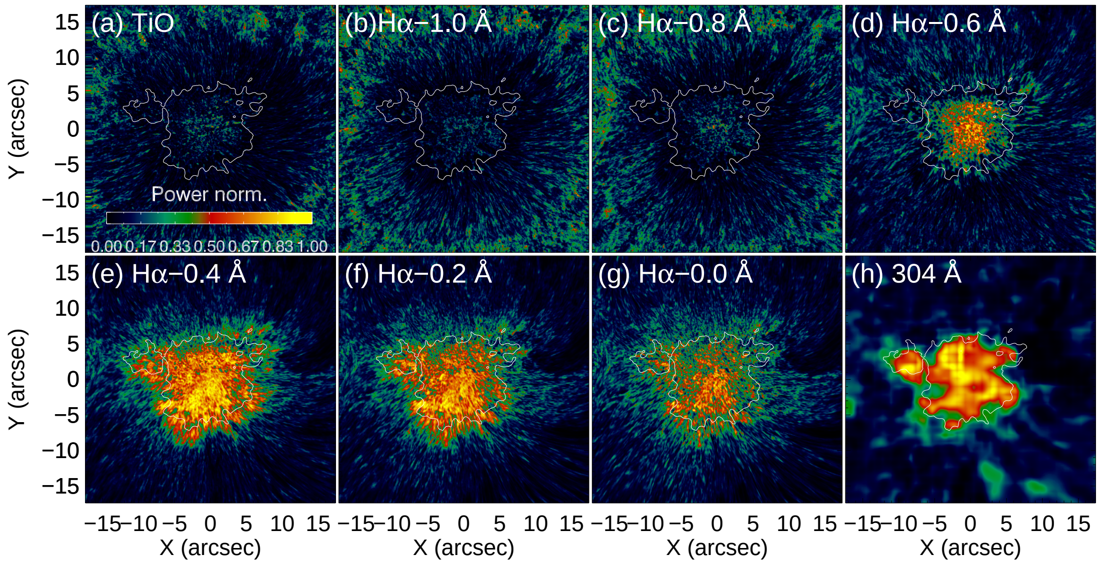

图 4.4: Similar to Figure 4.2 but for the higher frequency oscillations in a range of 1.7-3.8 min.

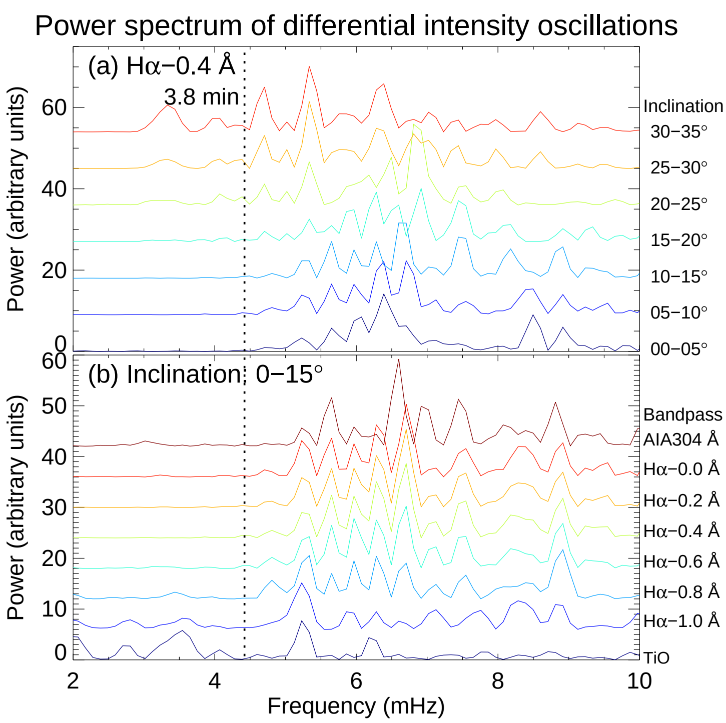

图 4.5: (a) Averaged power as a function of field inclination in the passband of H$\alpha - 0.4$ Å. (b) shows averaged power in a range of 0°-15° as a function of passbands TiO, H$\alpha - 1.0$ Å, ... and 304 Å.

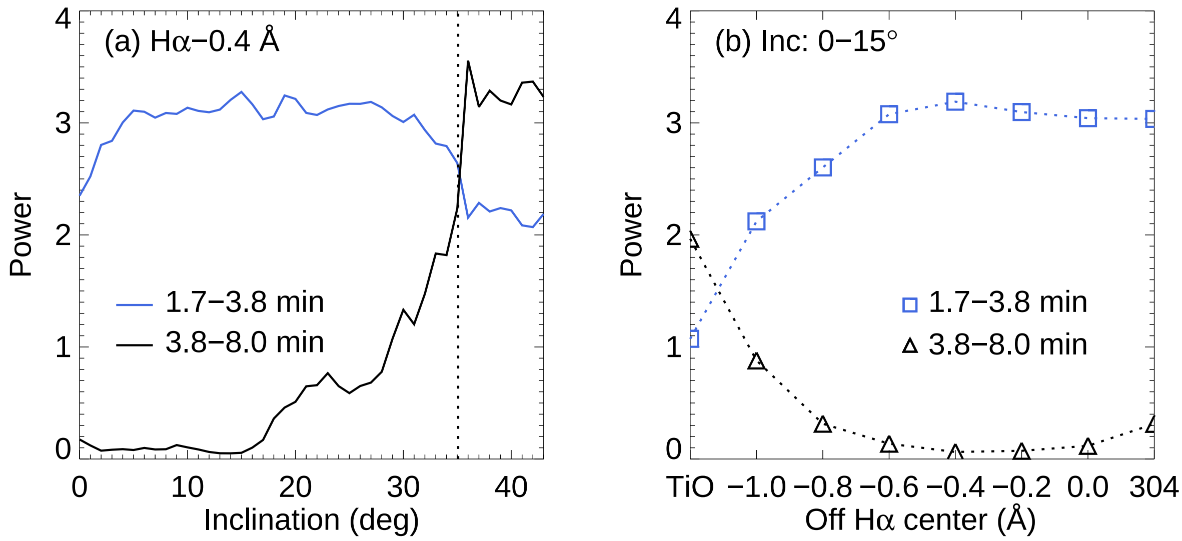

图 4.6: (a) Power spectra of H$\alpha - 0.4$ Å averaged over a circular slice with inclination range of 0°-5°, 5°-10°, ... and 30°-35° in the sunspot, where the dotted-line gives the limits of the umbra and the penumbra. (b) shows spectra of TiO, H$\alpha-1.0$, ..., 0.0 Å and 304 Å, averaged over a circular slice with 0°-15° inclination.

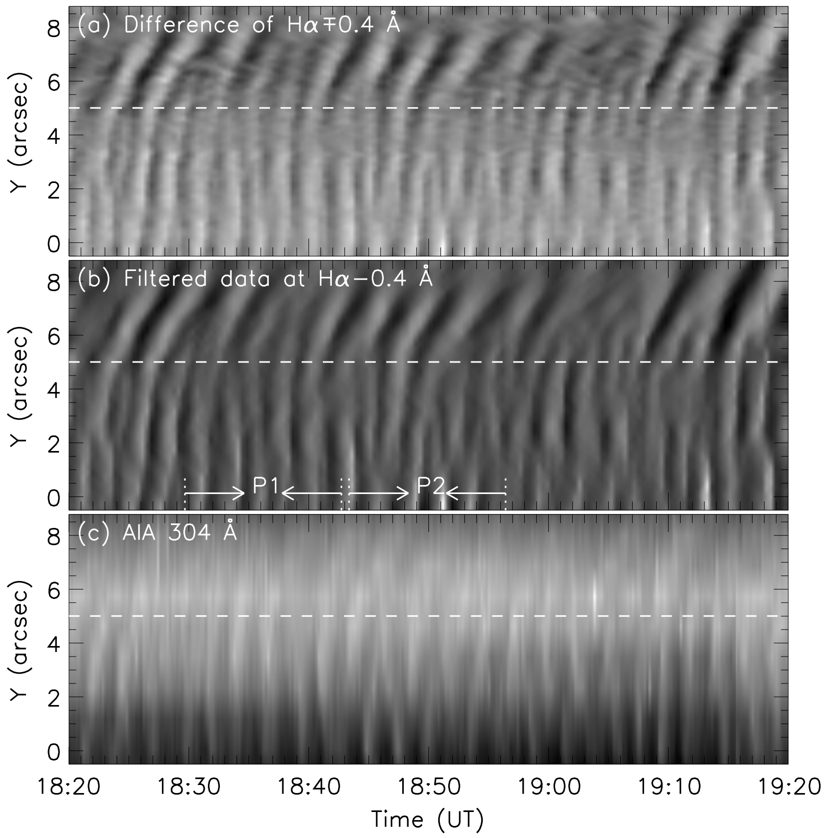

图 4.7: Time-distance diagrams of the Doppler shift (difference of H$\alpha \pm 0.4$ Å), H$\alpha - 0.4$ Å and AIA 304 Å, derived for the intensity averaged along the width of the slice shown in Figure 4.1 for the entire time sequence. White dashed line marks umbral boundary. The data in (b) marked by the arrows are to be analyzed in the following figure.

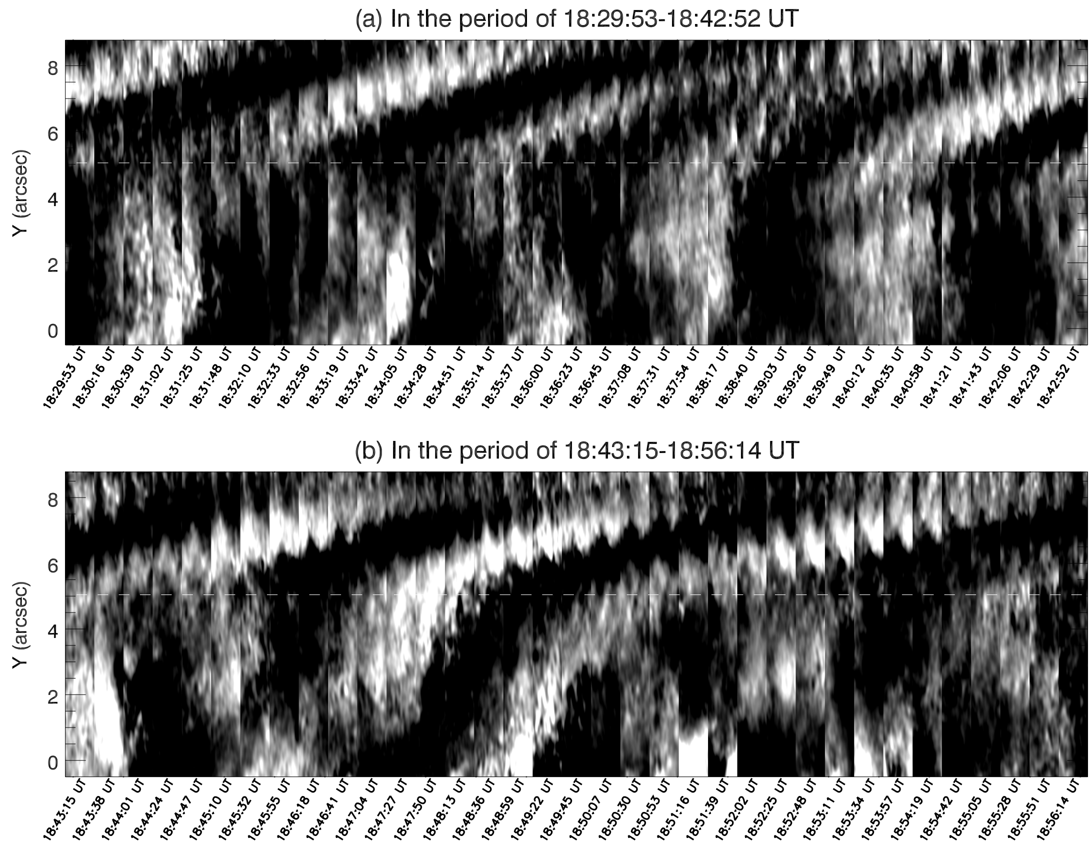

图 4.8: Time-distance diagrams for the slice shown in Figure 4.1 within the periods of 18:29:53 - 18:42:52 UT (a) and 18:43:15 - 18:56:14 UT (b). White dashed line marks umbral boundary.

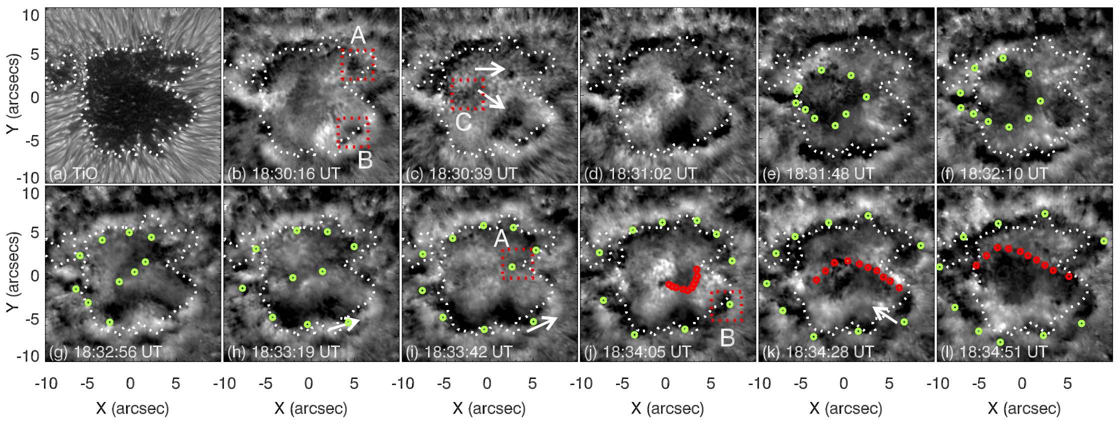

图 4.9: (a) a TiO map for reference and white dotted contours in it and the other panels mark umbral boundaries. (b)-(l) the time series of filtered H$\alpha - 0.4$ Å images with phase speeds > 4 km s^{-1}, on which circles are superposed to highlight the trajectories of running wavefronts. Red squares and capital letters A,B and C mark initial emerging locations of the next umbral oscillations.

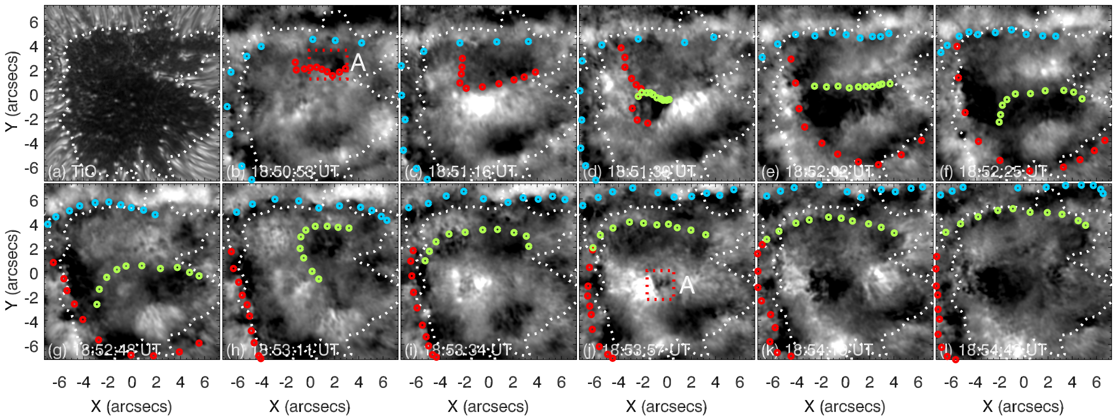

图 4.10: Similar to Figure 4.9, but for umbral oscillatory events of 18:51:39 UT and 18:53:57 UT.

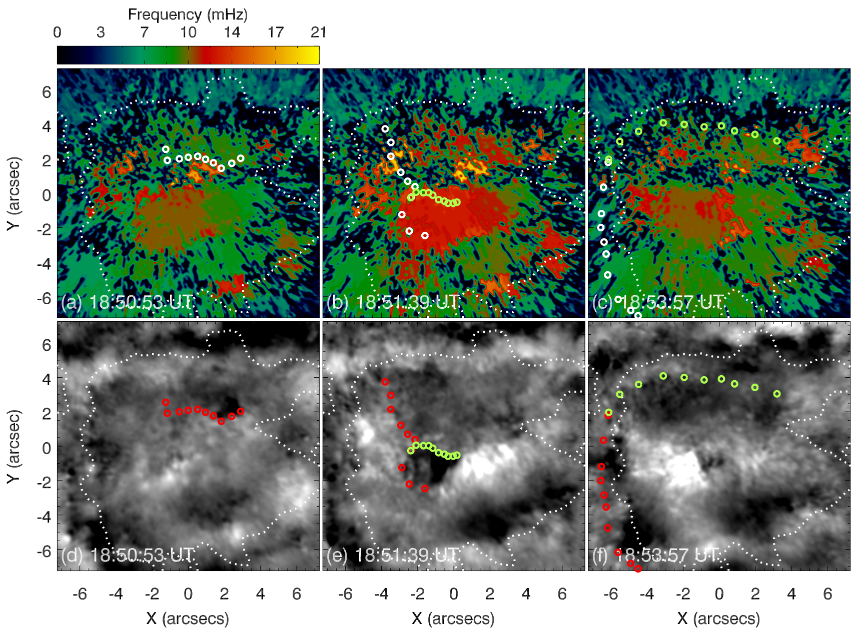

图 4.11: (a)-(c) distributions of dominant oscillatory frequency in the sunspot umbra, obtained with wavelet analysis for the time series of H$\alpha - 0.4$ Å filtered images. (d)-(e) the corresponding H$\alpha - 0.4$ Å filtered images for event of 18:51:39 UT in the three phases, first emerging, propagating to umbral center and developing into RPW highlighted with circles. White contours in all panels denote umbral boundaries.

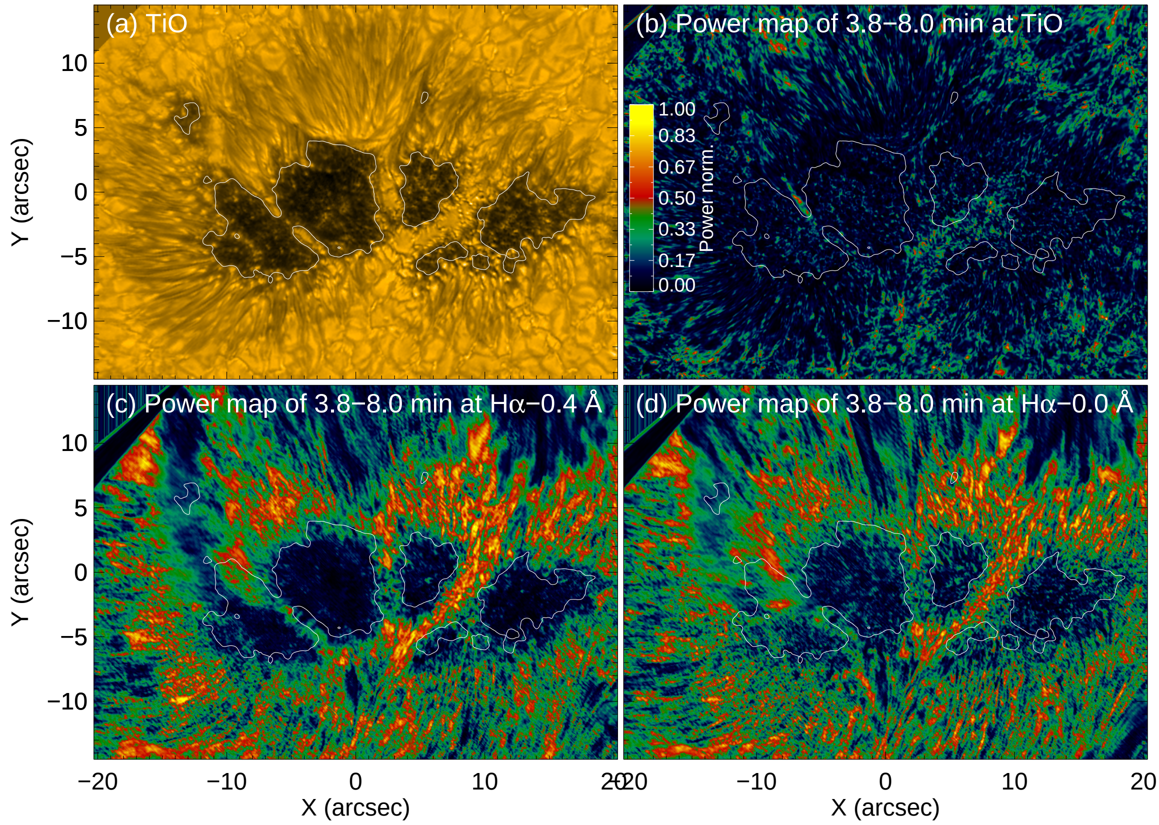

图 4.12: Maps of main sunspots of AR 12127. (a) the location of sunspots in TiO image. (b)-(d) the corresponding spatial distribution of normalized Fourier power for 3.8-8.0 min oscillations taken in the indicated passband. Note that umbral regions of sunspots are shown in white contours.

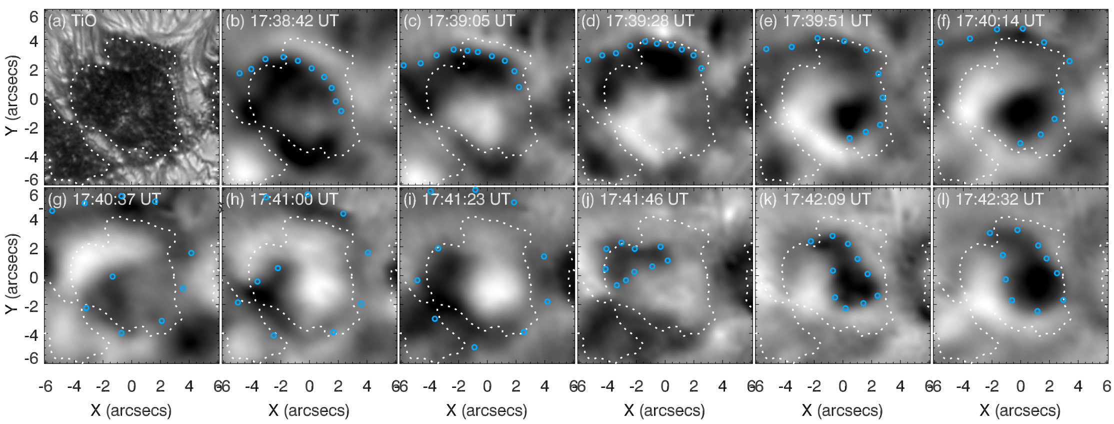

图 4.13: (a) a TiO map for reference and the white dotted contours marks the umbral boundaries. (b)-(l) the temporal evolution of the filtered Hα − 0.4 Å images with phase speeds $v_{ph} > 4$ km s^{-1}. Blue dots show the directions of wave propagation.

With a slit of $\sim 3''$ width, we constructed space-time diagram of the doppler shift (difference of Hα − 0.4 Å, and Hα + 0.4 Å), Hα − 0.4 Å, and AIA 304Å and derived the intensity averaged along the slit shown in Figure 4.1. We do not find much difference between (a) and (b) panels of Figure 4.7 as oscillations in umbral and penumbral regions are seen. But the panel (c) is quite different as it shows features of only oscillations in umbra and penumbra as well. To have a more broader view on such a propagation we gather two more diagrams along the slit as shown in Figure 4.8 in the two time intervals of 18:29:53 - 18:42:52 UT and 18:43:15 - 18:56:14 UT, respectively as seen in Figure 4.7. The connection between umbral oscillations and RPWs are generally demonstrated. In both panels, there are 5 individual complete umbral oscillatory events, e.g., at 18:31:25 UT, 18:34:05 UT, etc (named after their kick-off time), but correspond to 4 RPWs in panel Figure 4.8 (a) and only 3 RPWs in panel Figure 4.8 (b), respectively, which might be due to the merging of some of the umbral oscillations together or may be it could not propagate at all. Another puzzling feature is the association of some umbral oscillations with their preceding RPWs. For example, events of 18:31:25 UT and 18:34:05 UT were connected to their preceding RPW by some stripes, which indicates the inward propagation of the associated wavefront towards umbral center. Around 24 events of umbral oscillations in the time interval 18:19 to 19:19 UT (as shown in Table 4.1) has been investigated upon in details.

4.4 Propagation of RPWs

We investigate upon two umbral oscillatory events starting at 18:31:25 UT and 18:51:39 UT in panels (e) of Figure 4.9 and (d) of Figure 4.10, respectively. The three dark patches, A, B and C highlighted by red squares Figure 4.9 appeared

表 4.1: Umbral oscillatory events and RPWs in the period of 18:19-19:19 UT for AR 12127.

Umbral oscillations	Start time (UT)	θ [a] (degree)	$\bar{\theta}$ (degree)	Preceding[b] RPW	Following[c] RPW	$\bar{v}^{rpw}$ km s^{-1}
01	18:21:24	$10-20°$	15°	Yes	Yes	9.8
02	18:23:42	$10-25°$	18°	Yes	Yes*	9.8
03	18:25:40	$10-30°$	20°	Yes	Yes	9.2
04	18:27:58	$15-25°$	20°	Yes	Yes*	9.2
05	18:31:25	$40-30°$;30-20° ;15-25°	35° ; 25° ; 20°	Yes	Yes	10.0
06	18:34:05	$15-30°$	23°	Yes	Yes	10.5
07	18:36:23	$10-25°$	18°	Yes	Yes*	10.5
08	18:38:17	$30-45°$;10-30°	38° ;20°	Yes	Yes	13.8
09	18:40:58	$15-30°$;30-45°	26° ;38°	Yes	Yes	12.8
10	18:44:01	$25-40°$;30-45°	26° ;38°	Yes	Yes	9.7
11	18:46:18	$10-20°$	15°	Yes	Yes	8.0
12	18:49:22	$15-30°$	23°	Yes	Yes	7.5
13	18:51:39	$10-20°$	15°	Yes	Yes*	7.5
14	18:54:19	$0-15°$	8°	?	Yes	10.0
15	18:57:22	$25-40°$	33°	Yes	Yes	8.5
16	19:00:26	$25-40°$;10-25°	33° ; 18 °	Yes	Yes*	8.5
17	19:03:09	?	?	?	Yes	6.0
18	19:05:50	$25-40°$	33°	Yes	Yes	14
19	19:08:08	$25-35°$	30°	Yes	Yes	10
20	19:10:03	$10-25°$	18°	Yes	Yes*	10
21	19:11:57	$10-30°$	20°	Yes	Yes	12
22	19:13:52	$0-35°$	18°	Yes	Yes*	12
23	19:16:09	$0-10°$	5°	No	Yes	9.0
24	19:19:13	$25-35°$	30°	Yes	?	?

[a] Range of magnetic field inclination at the initial emergence of the umbral oscillatory event.
[b] Whether was the event related to its preceding RPW?
[c] Whether did the event develop into the following RPW?
Symbol $*$ denotes the following wavefront catching up and merging with its preceding one.

initially close to/on umbral boundaries. It has central field inclinations of ∼35° (A), 25° (B) and 20° (C) respectively (see Figure 4.9 (*b*)). A and B patches separated off from the umbral boundaries and patch C moved to the umbral center (see white arrows in panel Figure 4.9 (*c*)) The three patches become enhanced and then shrink towards the umbral center at 18:31:25 UT. At this juncture the first event of umbral oscillation began as shown in Figure 4.8. Later, a dark circular patch formed at 18:31:48 UT in umbral center and the wavefront began to expand at 18:32:10 UT. In the meantime, the propagation in clockwise direction at the top takes a spiral form along the trajectory of wavefront (See Figure 4.9 (i)-(k)). In Figure 4.9 (*k*), the spiral's top end marked in a red squares (denoted as A) separated from its main part and pushed itself towards the umbral center (see red circles in Figure 4.9 (*l*)) and a new oscillatory event began again (see

Figure 4.9 and Figure 4.10). It is immediately noticeable that the main part of the preceding wavefront crossed the umbral boundaries and became a circular trajectory of RPW. We compared Figure 4.9 (l) and Figure 4.10 (b) and found that the wavefront in umbral central region showed a rapid expansion. Subsequently, it expanded continuously in radial direction and finally became a RPW after crossing umbral boundaries as shown by the red circles in the following panels of Figure 4.10. It is seen in Figure 4.8 that there is a break between the umbral oscillation and RPW at 18:35:14 UT and 18:35:37 UT which could be attributed to the fact that the wavefront in slit location weakened when compared to the wavefronts in preceding or following panel and did not stop its propagation. Also, the stripes are stacked reversely, slightly slanted in Figure 4.8 from 18:35:37 UT to 18:37:31 UT suggesting an inward propagation of wavefronts. The initial emergence of the event at 18:36:23 UT is seen in Figure 4.10 (c), where it was located close to top right umbral boundaries (with $\sim 18°$ inclination) and is shown in yellow circles. It then propagated anticlockwise in azimuthal direction towards the umbral center (see Figure 4.10 (c)-(k)). This inward motion is consistent with the reverse slant stripes in Figure 4.8 (j). Note that the new wavefront merged with the old one at the top umbral boundaries (see Figure 4.10) with its left part propagating towards the umbral center than continuing its propagation along left umbral boundaries (see panels (j)-(l) in Figure 4.10). This leftward wavefront propagating towards umbral center resulted in a new wavefront. Similarly, the other two events occurring at 18:38:17 UT and in the period of 18:43:15 - 18:56:14 UT visualized in Figure 4.8 and Figure 4.9 showed similar behavior wherein the wavefront propagate towards the umbral center and merges with the preceding wavefront. A part of the merged wavefront jumps into the umbral center forming a new wavefront which ultimately results into a new umbral oscillation while the remaining wavefront crosses umbral boundaries to form RPW. In summary, we have interpreted the developments of features of dark patches A or B in the above 5 events with the wavefront initially reaching umbral boundaries without showing any further propagation along radial and azimuthal directions. Then, it begins to propagate towards the umbral center the next moment. Hence, it appears to build a connection between the preceding and the following running waves. It is important to emphasize that the wavefronts in some events were having multi-spiral structures and are complicated to determine their initial emergence, whether related to the preceding RPW or not.

4.5 The oscillatory frequency within the umbra of sunspot

The distribution of dominant oscillating frequency in the sunspot umbra for event 18:51:39 UT is shown in three phases (see Figure 4.11 (a)-(c)): The initial emergence followed by its propagation towards umbral center and finally its development into RPW. The power of short period oscillation was weak at umbral center, before and after the wavefront propagation (see Figure 4.11 (a)-(b)). Also, one can see that the dominant periods are very much different along the wavefront direction, and the averaged periods over the wavefront edges in the panels are 2.7 ± 5.3 min, 2.8 ± 5.9 min and 4.0 ± 7.0 min, respectively. This may indicate that the running waves in the sunspot are broadband waves.

4.6 Transient brightening event in sunspot penumbra

In the TR most of the interesting research has been focused on sunspot oscillations and explosive events or blinkers by Aschwanden (2004)[21]. The successful launch of the Interface Region Imaging Spectrograph (IRIS) by Depontieu (2004)[17] enabled us to investigate the TR above sunspots with an unprecedented spatial resolution of about $0.33''$ and many subarcsecond bright dots in the sunspots which are found in the TR[128]. The corona appears to be highly dynamical above the sunspots, as evidenced by quasi-periodic upward propagating disturbances (PDs)[129], jets, active region transient brightenings observed in the EUV or X-ray wavelength bands, and EUV bright dots[21], etc. One such kind of a brightening is seen along a loop observed in Hα image, which seem to be propagating along the loop rooted at the umbral boundary. The chapter 6 describes details on the brightening seen along one such loop. The up-to-date high-resolution observation from the High-resolution Coronal (Hi-C) imager revealed that the EUV bright dots at the edge of sunspots have a typical lifetime of 25 s and their length is about 680 km ($<1''$)[130]. These new findings gives a unique opportunity to understand the dynamic evolution of plasma at subarcsecond scales in the case of strong magnetic fields. A subarcsecond penumbral transient brightening event with the high-spatial resolution observations from the 1.6 m Goode Solar Telescope (GST), Interface Region Imaging Spectrograph (IRIS), and the Solar Dynamics Observatory has been reported[13]. In general, most of the solar activities occurring at different solar atmosphere layers near sunspots are not independent, but are closely interconnected, because there are various interactions between energy and mass among these layers. As is well known, there is strong coupling among the chromosphere, TR, and corona during solar flares[20].

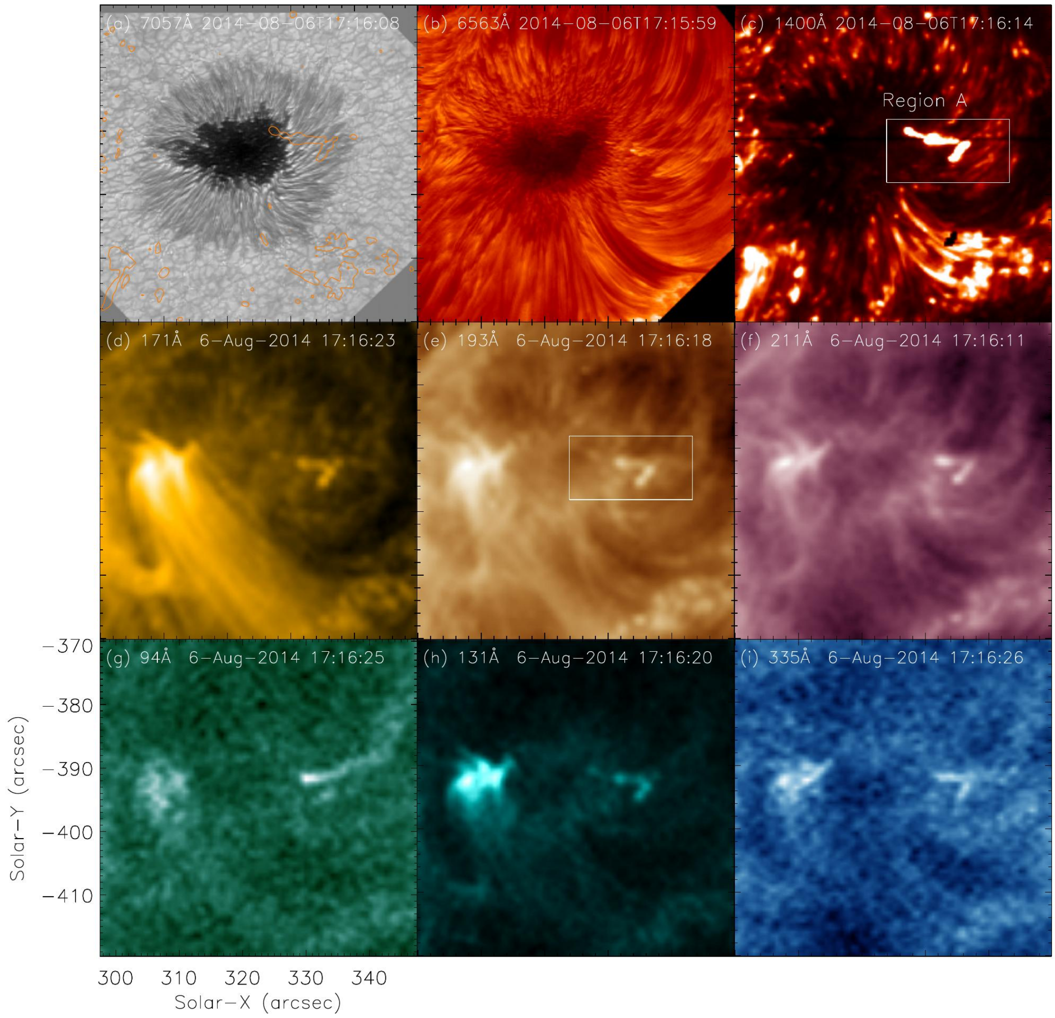

图 4.14: Images obtained with NST, IRIS and SDO/AIA around 17:16 UT on 2014 August 6, containing the photosphere(a), chromosphere(b), TR (c) and corona (d)-(i) layers. (a) The brown contours are from 1400 Å generally mark the location of the brightening region. (c) Region A shows the position of the penumbral transient brightening event[13].

Some flare models indicate that magnetic reconnection first takes place in the corona, and then the chromosphere below is heated up by the downward propagating accelerating particles and the thermal conduction, which generates emission seen as flare ribbons. The heated chromospheric plasma can then trigger an upflow, which is called chromospheric evaporation[21]. The above scenario is confirmed by observations[22–27]. Regarding small-scale solar eruptions, such as microflares, it is found that their evolution closely resembles those of large flares. For example, they are seen in soft X-ray, hard X-ray, EUV, and Hα wavelengths, indicating that microflares have signatures not only in the chromosphere, but also in the corona[131–136]. Chromospheric evaporation is also observed in a microflare by Chae et al. (2010)[137]. Moreover, Hα surges and EUV jets are usually found to be associated with the microflare[138] which are generally thought to be driven by the release of non-potential magnetic energy[21]. Another such a small-scale penumbral transient brightening event has been observed by IRIS (as seen in Figure 4.14) and GST. Its evolution and spectroscopic signatures at the chromosphere and TR, reveals its signature in the corona using observations from AIA on board the SDO, and try to find its relationship with the evolution of magnetic fields by employing HMI data. The possible triggering mechanism of the transient brightening event is magnetic reconnection. The evolution of the magnetic fields of the radial magnetogram from HMI CEA data show that an Moving Magnetic Feature (MMF) with negative magnetic polarity emerges in the photosphere and then moves outward. The magnetic cancellation between the MMF and the nearby magnetic fields with opposite polarity is observed at one footpoint associated with the brightening event. The new emerged magnetic field and its cancellation with the existing opposite magnetic fields are generally thought to be the observational evidence for magnetic reconnection. According to simulation results by Jiang (2012)[139], the height of the magnetic reconnection is possibly in the low corona and hence the emission is seen in all of the AIA EUV passbands and the increase in temperature is seen from the DEM analysis. It is seen that a part of the plasma from the magnetic reconnection process moves downward and reaches the TR, as evidenced by the redshift in the Si IV 1402.77 Å line and the inward motion in IRIS 1400 Å passband. Finally, it arrives at the chromosphere and appears as ribbon-like brightening. If the interpretation (Bai et al. (2016)[13]) of the penumbral transient brightening is correct, then observation indicates that the magnetic reconnection process possibly occurs at a scale as thin as 100 km.

第五章　Evolution of Dynamic Fibrils

As discussed in chapter 4, the umbral wavefronts emerges at the chrmospheric umbral center and grows into RPWs but a part of the already emerged RPWs are the source of newly formed RPWs. Many such events have been observed. Along with studying the emergence of RPWs, the dynamic fibrils (DFs) which appears to be jet-like, are connected around the same region has also been studied. The formation of jet like DFs, mottles, and spicules in the chromosphere of the sun is one of the most important phenomena of the Suns magnetized outer atmosphere. It was a subject of debate if quiet-Sun jets such as spicules or mottles follow parabolic paths that are ballistic (i.e., solar gravity), or of constant velocity. Few studies from high resolution data reveals that most of the active region DFs observed in the Hα line core follow parabolic paths. The solar chromosphere is dominated by linear structures that display vigorous dynamical evolution on time scales ranging from seconds to minutes. Off the limb, elongated features are observed as spicules with typical linear dimensions between 5 and 10 Mm by Tsiropoula (2012)[140]. High-resolution Hinode observations revealed the existence of at least two types of spicules, of which the second class, or type II spicules, was found to be most abundant in the solar atmosphere by De Pontieu (2007)[141]. Type I spicules are mostly found in ARs, are the minority species in the quiet Sun, and are virtually absent in coronal holes[142]. They are characterized by clear rising and descending phases on time scales of 140-400 s and their tops describe a distinct parabolic trajectory in the space-time domain. Their properties agree well with what was measured on the solar disk for dynamic fibrils in AR plage[141] and for some mottles in the quiet Sun[143]. Numerical simulations demonstrated that this wave-like behavior is driven by slowmode magneto-acoustic shocks that result from p-mode waves leaking from the photosphere into higher atmospheric layers[141,144–147]. It has been shown that the five minute p-mode oscillations that earlier were considered to be evanescent above the photosphere can propagate progressively more efficiently along increasingly more horizontal magnetic fields[17]. When these long-period waves propagate to higher atmospheric regions with lower density, they turn into shocks that drive the observed dynamic fibrils. Such a change in the cutoff frequency for wave propagation along slanted fields had earlier been described[148,149] but was not appreciated in the subsequent literature[150].

5.1　Analysis of the dynamic fibrils

Using the high cadence and high spatial resolution observations of NOAA 12132, we have therefore fit the paths to all DFs outlined in the Hα line center with parabolas. We have used these fits to determine velocities and decelerations. The Figure 5.1 shows the detected dynamic fibrils which are used for further anlaysis in the following sections. A close look into Hα line core images gives an insight into fibrils located in the close proximity and in the vicinity of sunspot near the image center, a few of which were colligated with the superpenumbra. We investigate upon 40 such DFs for this study, wherein most AR DFs from the line core of Hα images ensues almost a perfect parabolic paths.

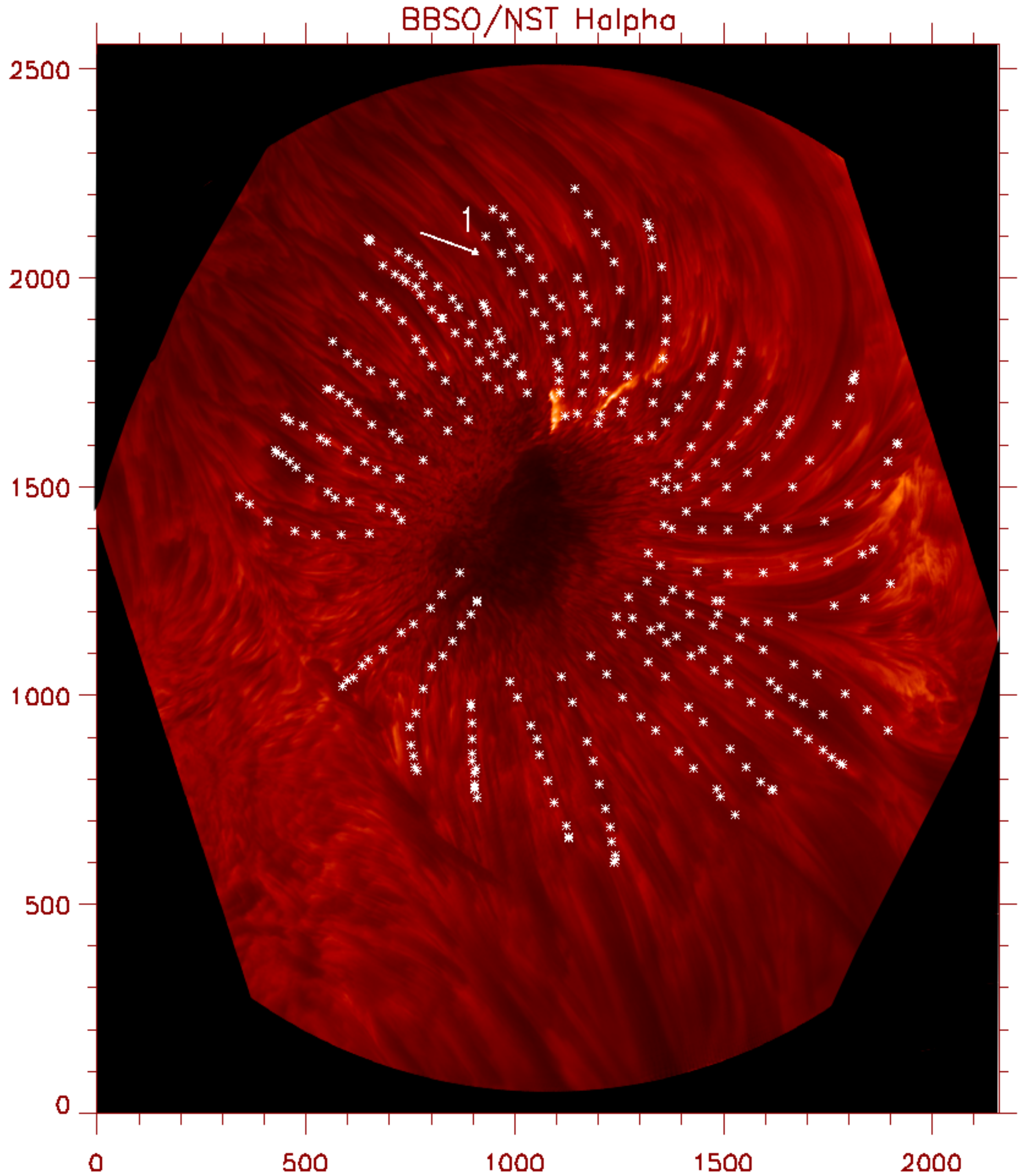

图 5.1: Hα line core image showing the paths of DFs overplotted. The DF marked as '1' is used for further analysis. Tick marks are in Pixels.

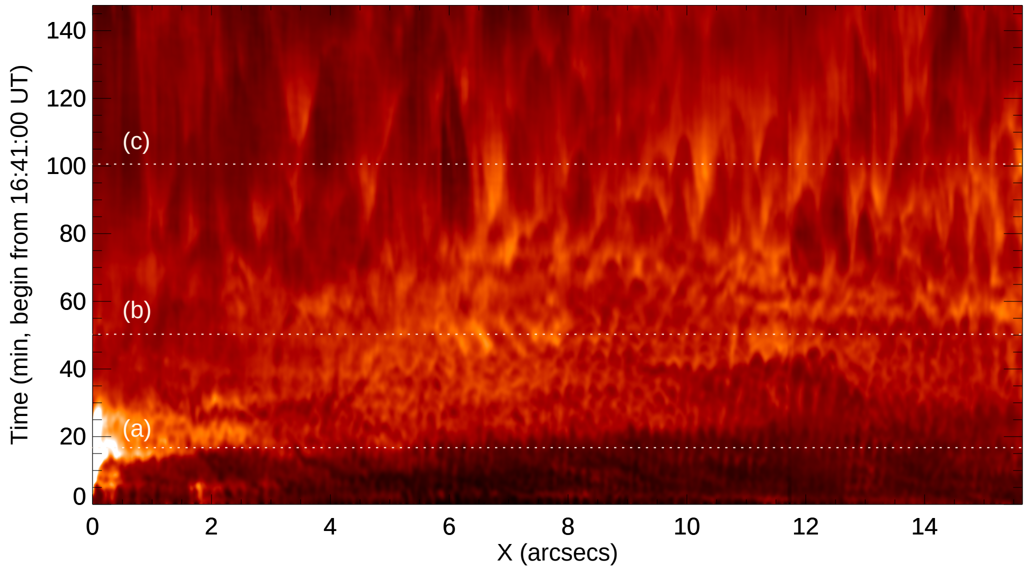

图 5.2: Space time diagram of the Hα line center image for DF marked as '1' in Figure 5.1. The three dotted lines indicates the umbral (a), penumbral (b) and superpenumbral (b) regions for which power spectrum is shown in Figure 5.9.

5.1.1 Measurements from CRisp SPectral EXplorer

We opt for choosing the direction of a DF, or a bunch of DFs, manually using CRisp SPectral EXplorer CRISPEX[14] which helps in analyzing the multidimensional data cubes and an additional software called TANAT (Timeslice ANAlysis tools) for analyzing and also for various measurements of data. The CRISPEX is a widget based versatile IDL tool for visual inspection and analysis of high resolution data. CRISPEX also provides space-time diagram for all the linear as well as curved paths (See Figure 5.2 and Figure 5.3 showing an example for the space-time diagram). This information could be stored and could be retrieved later for further analysis. A default layout of the windows loaded by the software CRISPEX is shown in Figure 5.4. We have produced the space-time diagram for all the 40 DFs detected. A comprehensive use of this software not only made the seeking of sequence of images easier but also helped in tracking the events that were very clear while ascending and descending along their individual paths in 584 jet like features in Hα. The space-time diagram for one of the DF is shown in Figure 5.2 and its evolution is shown in Figure 5.5. A space-time diagram is shown for a linear path that crosses from the umbra through the penumbra and into the surrounding plage (see the location of the path marked in Figure 5.1.)

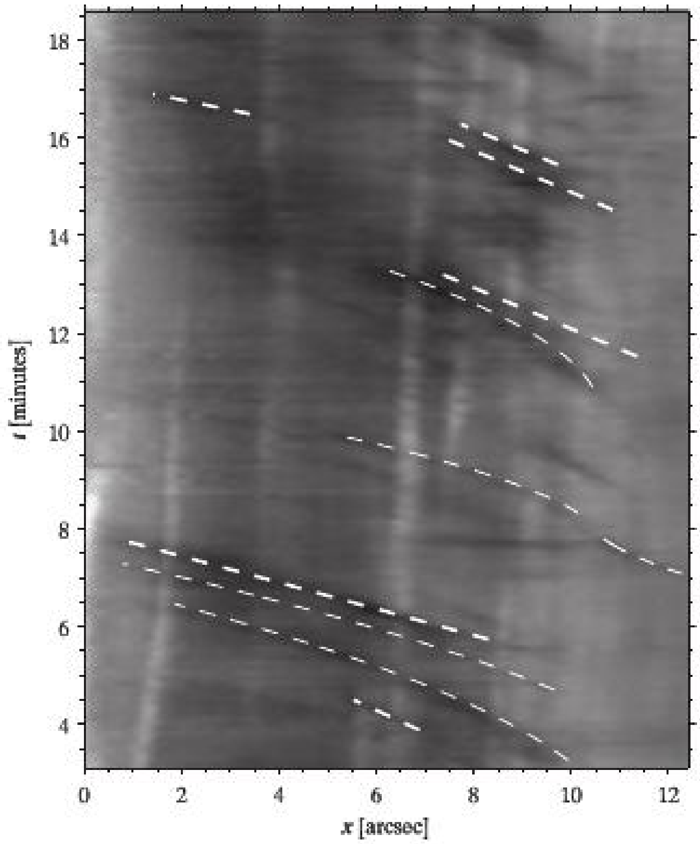

图 5.3: The dashed curves indicate measurements of the projected velocity and acceleration components and illustrate the method discussed[14].

5.2 Dynamics of the fibrils

The Figure 5.5 shows the receding of the already risen DF along the same path. We have detected almost 584 such trajectories and did a parabolic fitting on it. Figure 5.6 gives an example of the fitting. From the fit, we calculated the parameters like deceleration, maximum velocity, maximum height, duration and kinetic energy as well and showed the distribution through scatter plot in Figure 5.7. We assume the electron density to be same throughout the chromosphere. This electron density (n_e) multiplied with the mass of the electron (m_e) gives density ($\rho = n_e m_e$) which means that the kinetic energy per unit volume would be equal to the square of the maximum velocity (KE $= v_{max}^2/2$). The kinetic energy per unit volume of these jet like features may transform further into heat and might play a significant role in the heating of corona.

By tracing all the jet like features we obtain the histograms of max velocity, duration, deceleration, and the kinetic energy shown in Figure 5.8. From the histograms, it is detected that the maximum velocity, duration and decelerations follows a Gaussian distribution. The maximum velocities are within 10 km s^{-1} to 30 km s^{-1} and the average is about 15 km s^{-1}, the duration ranges from 2 min to

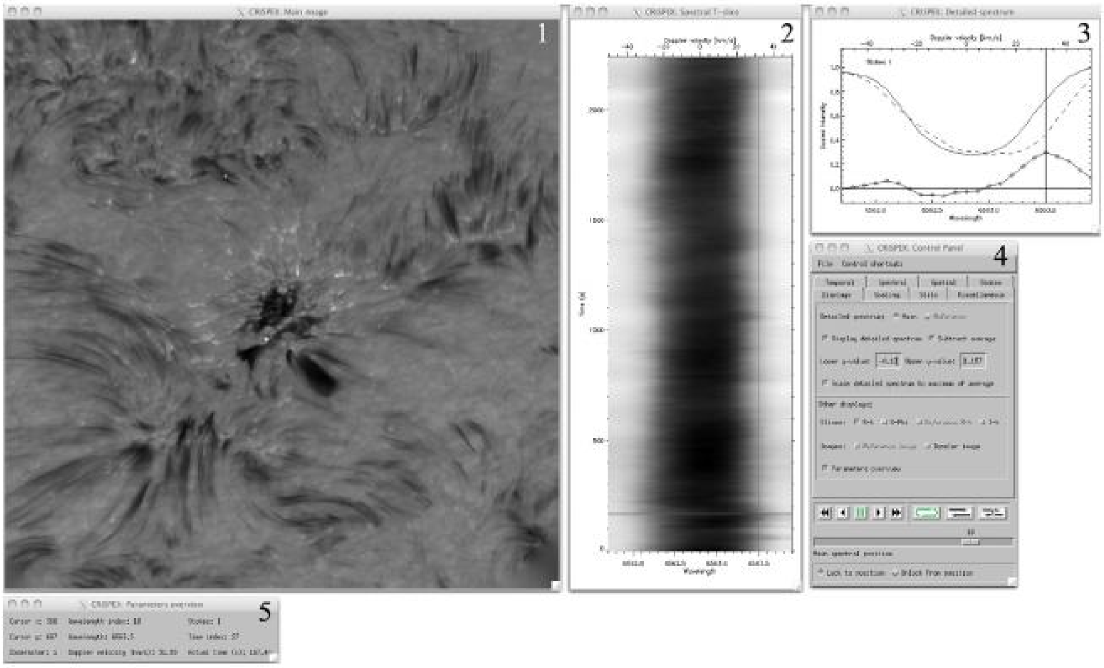

图 5.4: Default layout of windows loaded by CRISPEX, showing clockwise from the top left: (1) the intensity image, (2) the spectrum-time diagram, (3) the local spectrum, (4) the control panel, and (5) the parameters overview window[14].

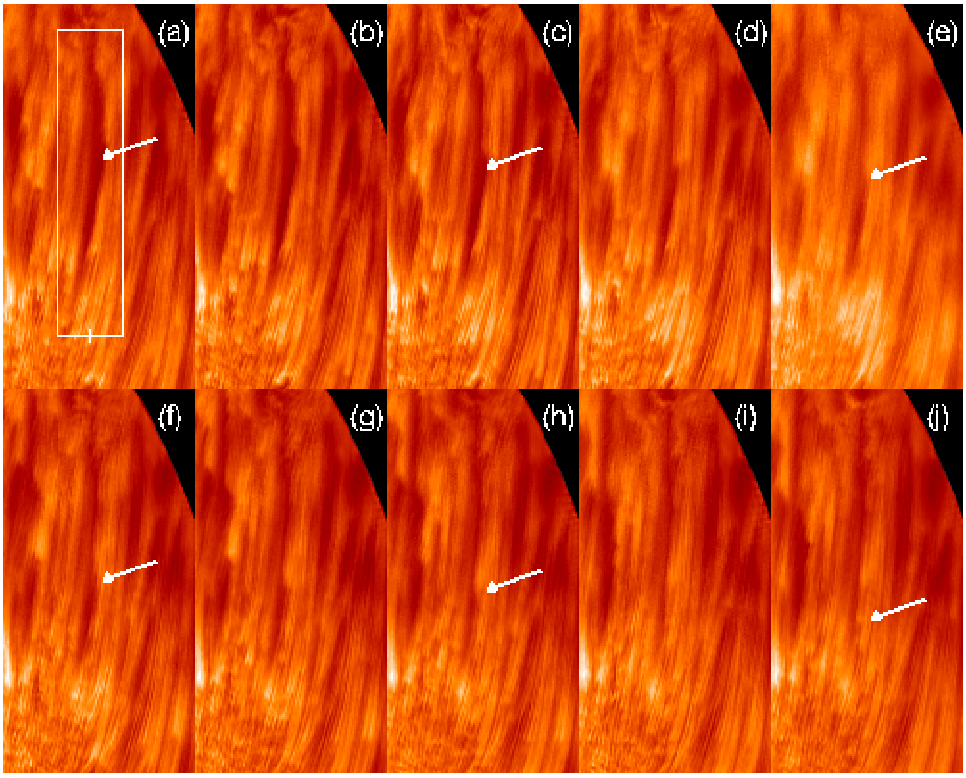

图 5.5: The snapshots of Hα line core showing the temporal evolution of DFs (marked as '1' in Figure 5.1) as it recedes.

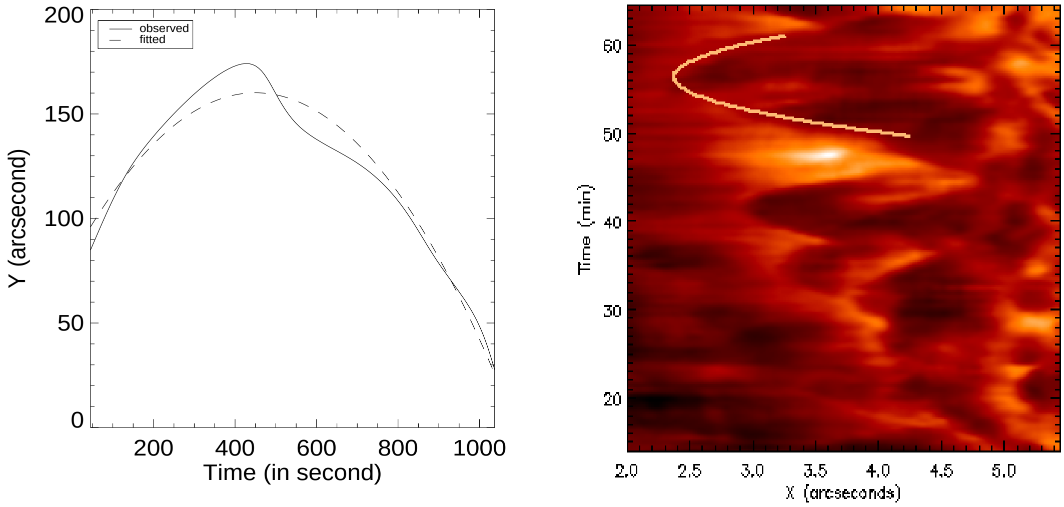

图 5.6: The extracted portion of x-t plot for sample DFs are shown. The DFs follows almost perfect parabolic path. The yellow line indicates the bestfit used to derive the deceleration, maximum velocity, duration and the maximum height. The parabolic fitting for corresponding trajectories are shown.

20 min and the average is about 11 min, the deceleration ranges from 10 m s^{-2} to 200 m s^{-2} and the average is around 100 m s^{-2}. We obtain the average maximum height to be around 0.025 Mm. We find the kinetic energy of all the 584 jet like features and estimated its average to be about 220 gm $cm^{-1}s^{-2}$ and found it to follow a partial Gaussian distribution.

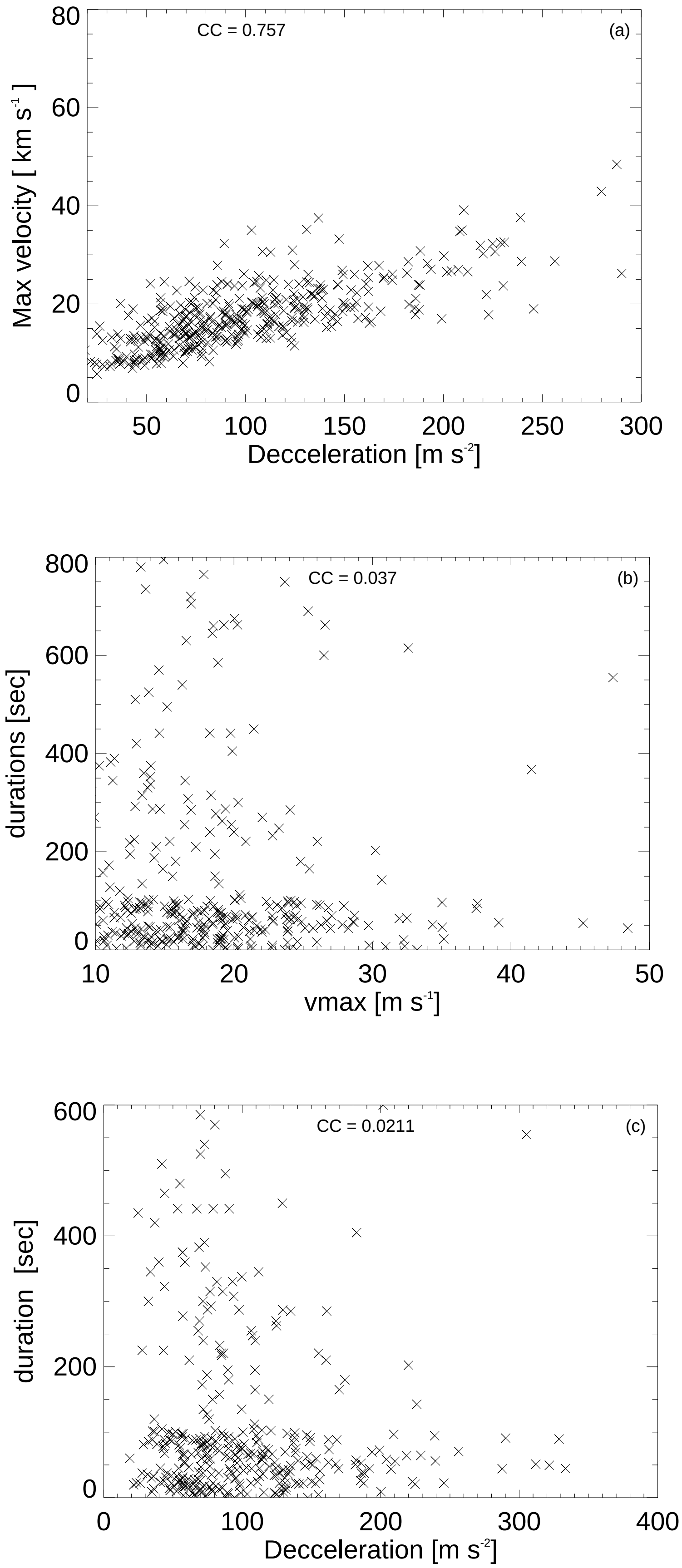

图 5.7: Scatter plots of deceleration vs. maximum velocity (a), maximum velocity vs. duration (b), and deceleration vs. duration (c). A clear linear correlation exists between the deceleration and the maximum velocity.

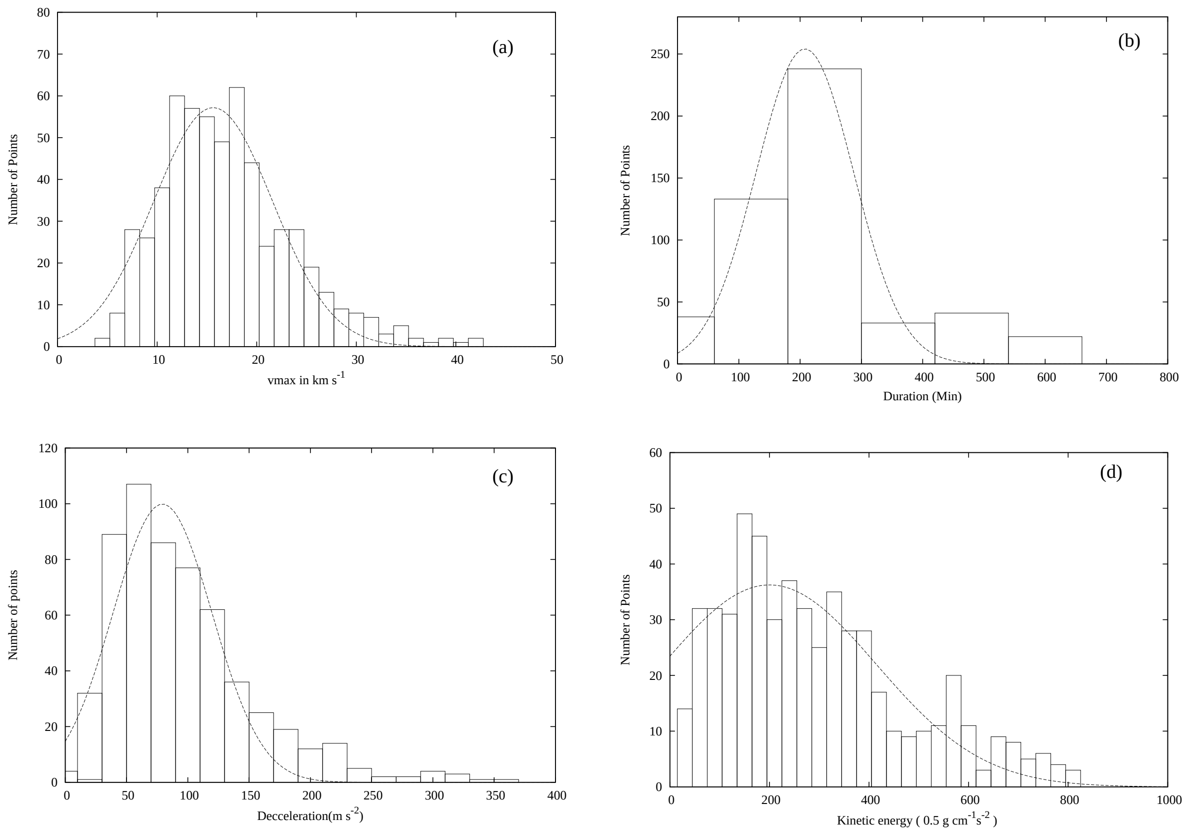

图 5.8: Distributions of the maximum velocity (panel (a)), duration (panel (b)), deceleration (panel (c)), Kinetic energy (panel (d)) respectively. The histograms are constructed from the observations of DFs.

We obtained the maximum velocity is between 10 km s^{-1} and 30 km s^{-1} and deceleration between 50 m s^{-2} and 200 m s^{-2}. We noticed that these correlations are quite similar to the measurements on dynamic fibrils done by Hansteen et al. (2006)[146]. But we found that the correlation between the duration and the deceleration/maximum velocity is comparatively weaker, showing a high scatter and nonlinearity in almost all the DFs. It is seen that the correlation between the duration and the deceleration/maximum velocity is not so clear or in other words weak[146]. Similar results have been obtained in DFs with the reason being the effect of projection by Langangen et al. (2008)[151]. It could be probable that there is no effect of projection seen in duration whereas the effect is more prominent in velocity and deceleration. It is very clear from scatter plot in Figure 5.7 that the correlation between duration and deceleration/maximum velocity is ambiguous with huge scatter and difference in slopes.

5.3 Umbrae, Penumbrae and Fibril Oscillations

To study the strength of an oscillation, the power-map which is the squared amplitude or power, was obtained from the Fourier transform. The method adopted for the power-map is discussed in Krijger et al. (2001)[152]. We look into the connection between oscillations in the umbrae, penumbrae and the fibril which are important for studying the relationship between the fibril and the sunspot as demonstrated by Chae et al. (2014)[120]. We take the fourier power spectra along the DF (originates from the umbral boundary and propagates higher up into the superpenumbral region) at three different points along the DF as shown in Figure 5.9. The power spectra in Figure 5.9 (a) is at the umbral boundary, (b) is at penumbral region and (c) is at superpenumbral region. The running waves travels through the boundary of umbra and penumbra and eventually disappears at the penumbral boundary. In the power spectra we see oscillations in DF varying with time. To measure the oscillation period, we use the FFT function using IDL. As shown in Figure 5.9, the frequency at the umbral boundary is $\approx$ 4.3 mHz and based on the frequency of the power spectra, the oscillation periods at the same point is 235 s. The results show that the oscillations within umbra are a typical 3-min oscillation with period T = 235 s, and the oscillations of the same within penumbra are a typical 5-min oscillation with period T = 345 s and T=408 s. The period of umbra oscillations is almost one half of that of the penumbral oscillations. The corresponding periods of umbral and penumbral oscillations measured by using FFT function are T_umbra = 235 s and $T\_penumbra$ = 408 s respectively. These oscillations propagates higher up and further develops into shocks as shown in Figure 5.10 suggesting oscillations are upward propagating shock waves which will be discussed in the next section.

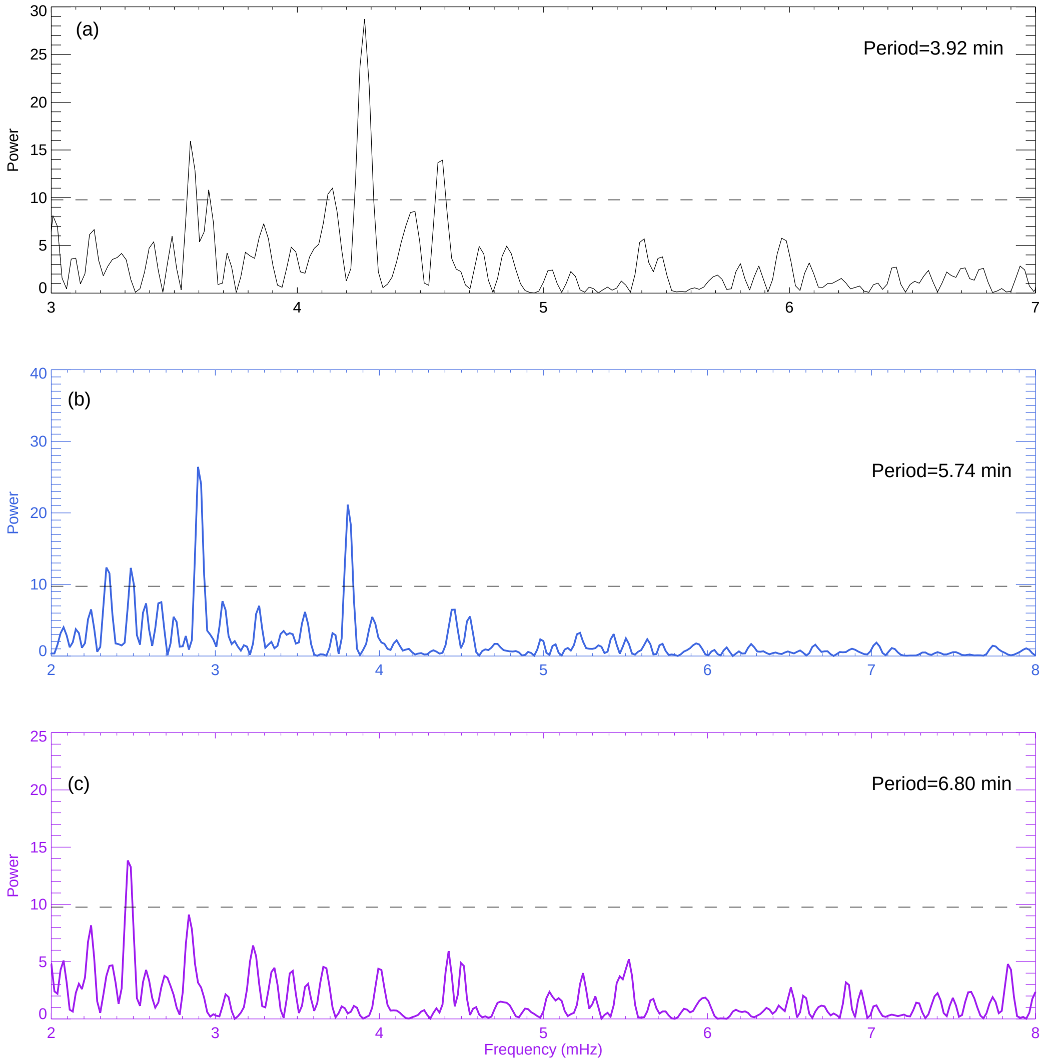

图 5.9: The fourier power spectra at the positions marked in white dotted lines in Figure 5.2.

5.4 Shock wave propagation

The presence of upward propagating waves and shocks in sunspot atmospheres has been known from both observations[33] and simulations. The parabolic paths in dynamic fibrils occur as a natural result of shock wave driving. When a shock impacts the top of the chromosphere, the plasma is catapulted upward at a velocity that exceeds the local sound speed of ∼510 km s^{-1}. This agrees well with the lower cutoff at 10 km s^{-1} of maximum velocities in the observed DFs. Shock waves generally have velocity profiles in the form of N or sawtooth shapes[153]. As a result, a plasma parcel passing through a shock wave will first experience a sudden impulse in velocity, followed by a gradual, linear deceleration as the shock recedes; this is consistent with a parabolic path. As seen in Figure 5.10, each panel corresponds to three different positions along the marked DF in Figure 5.1. It is quite possible that the dynamic fibrils are usually driven in union with the sunspot oscillations[120]. The Oscillations propagates higher up and develops into shock which propels the fibrils quite a several times. Thus, we speculate that the shocks driven DFs are related to the sunspot oscillations. To be more precise, there exists a form of propagation of shock wave fronts that starts from the sunspot center and reaches the bottom of the fibrils and propagates higher up along the DF[120]. Hence, it is clear that the DFs are physically related to the sunspot oscillations and the form of shock fronts propagates from the sunspot center. Figure 5.10 shows the temporal-spectral variations (λ-t plots) indicating the oscillations at three different positions along the DF (connecting the sunspot to the fibril) to infact be the upward propagating shock waves. The simulations showed the upward propagating magnetoacoustic shock waves and created the dynamic fibrils observational behaviour[141,146]. They found that the highly dynamic chromospheric shock waves cause significant upward and downward motion of the upper chromosphere. The transition of an upward propagating shock through the chromosphere produces a form of sawtooth or N-shape (as seen in Figure 5.10), which marks an impression of blueshift followed by a gradual drift towards the redshift and then a sudden appearance of a blueshift[146]. The N-shape pattern preponderate in all the three λ-t plots constructed at different locations along the DF and hence confirms the idea of shock driven fibrils. The correlation coefficient between the maximum velocity and deceleration of a sample of 40 sunspot dynamic fibrils is 0.757. This proves that the oscillations in sunspots are the magnetoacoustic shock waves that propagates upward[80,101,120,154].

The above found correlations could probably be a significant signature for the jets that are periodic, are perhaps driven by the waves that normally propagates from photosphere into the chromosphere and hence steepen into shocks[155]. The maximum velocities of these jet like features that we have found in our data are usually between 10-30 km s^{-1} and is found to be similar in comparison other results[11,146].

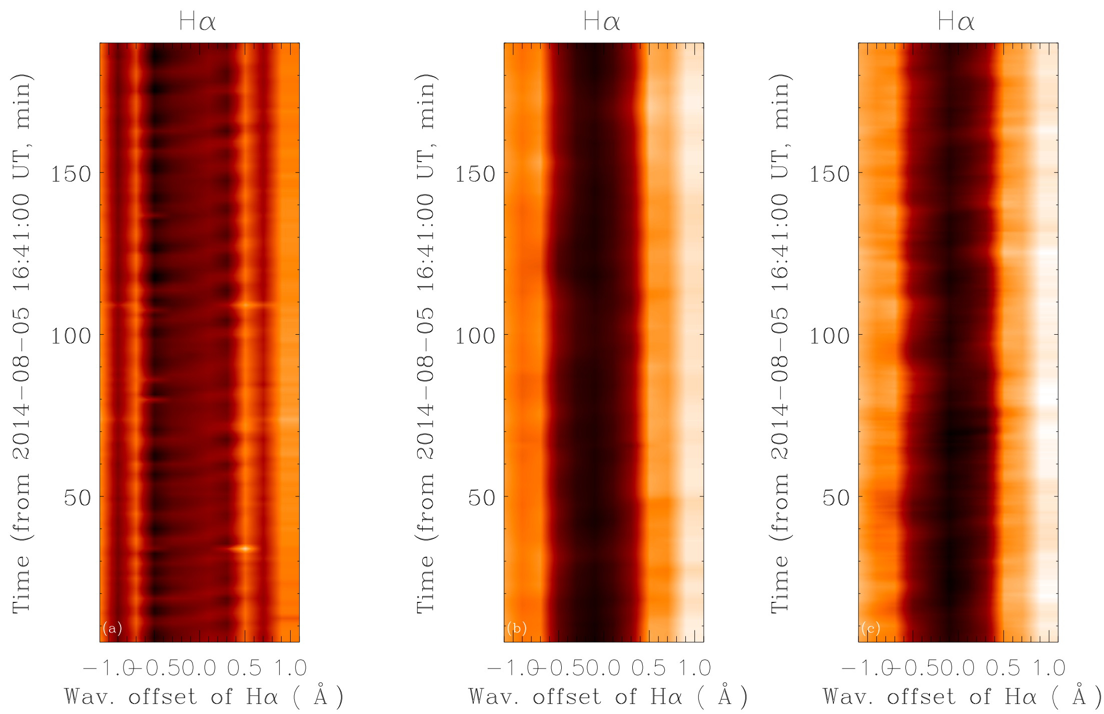

图 5.10: Shock waves along the dynamic fibrils. The wavelength-time maps of the Hα spectral line at different points along the DF as it propagates upward is shown in (a), (b) and (c).

The chromospheric waves are usually created by the usual convective flows and also due to the oscillations found in photosphere and also in the convection zone. These disturbances further propagates into the chromosphere upwards and thereby shock and becomes a driving force for the plasma in chromospheric region and hence results in the formation of the DFs. It is well known that compressional acoustic waves can easily evolve into shock waves during propagation, and the distance required for a shock to form in the stratified medium Stein & Leibacher (1974)[156] is given by

$$d = 2\Lambda log_e(1 + \frac{Pc_s^2}{2(\gamma+1)\Lambda v_1}) \tag{5.1}$$

where $\gamma = 5/3$, $c_s = 9.6$ km s^{-1}, $P = 1.9$ min, $\Lambda = 200$ km (scale height) and v_1=1 km s^{-1} (the initial amplitude of a wave).

The periods that are longer than the period of local acoustic cut off is blocked by the chromosphere. This cut off period is completely dependent on the magnetic filed line inclination with respect to the vertical [17,150]. A single shock could possibly drive the DFs and is also the reason to understand the correlation between the deceleration and the maximum velocity. These DFs are the direct consequence of the upward propagating chromospheric oscillations/waves that are produced in the convection zone or photosphere as a result of global p-mode oscillations and also the convective flows. The waves propagates into the chromosphere and passes through upto the region where Hα is formed, thus forming shocks thereby while its upward propagation. The fact on which we stress our interpretation is that the DFs follow a parabolic path with a good positive correlation between the properties like the velocity and the deceleration for all of the detected DFs. We found that velocity and deceleration are directly proportional with higher the velocity, the higher is the deceleration. The velocity reported by Suematsu (1995) [100] for their event of mottles is in the range of 10-30 km s^{-1} and we found it to be rather similar to what we found in our BBSO/NST observations for our event of DFs. It was also evident from other [146] reports that the formation of DFs is due to the shocks in the chromosphere driven by the photospheric convective flows and oscillations as well. Hence, we conclude that the driving mechanism is same. Simulation also explains that the usually long period waves propagates into the solar atmosphere along the magnetic field lines that are inclined [147,157]. The most essential conclusion is with the explanation that the driving force for the DFs are the so called magnetoacoustic shocks that are induced by the p-mode oscillations and in addition leakage of convective flows into the chromosphere. Both the observations by Lites (1992) [33] and simulations by Bard (2010) [158] provides enough evidence for the waves that propagates upwards and also the shocks in the atmosphere of the sunspots. This phenomena appears as a dark feature in the Hα images and are due to the density of magnetic flux. It was proposed that the similarity between the observations and some modeling done earlier on the DFs provides reason for the upward and downward movement of the upper chromosphere which is due to the shock waves in the chromosphere [17]. It is also proven that the oscillations which appears to be like surge or light walls which lies above the LB are also caused by shocks [159]. Our findings indicates that, in ARs, most of these jet like features are caused by the shocks in chromosphere.

第六章　Coronal loop heating

The solar magnetic field has long been recognized as playing a key role in the transport, storage, and release of energy from the photosphere to the corona[160,161]. Plasma in the solar atmosphere is mostly confined to magnetic structures called coronal loops which are regarded as the basic building blocks of the solar corona. Any improvement in the knowledge of these loops, such as the exact thermal structure of a coronal loop and other such properties, can therefore help us to solve several long-lasting questions related to corona (e.g., coronal heating). One of the earliest attempts to theoretically model the coronal loops was made by Rosner (1978)[162]. They derived scaling laws between the temperature, pressure, and length of the loop and demonstrated that in a uniformly heated stable hydrostatic loop, the temperature maximum must be located near its apex. It is proposed by Aschwanden (2001)[163] that for long EUV loops, most of the heating is concentrated at the foot points, resulting in the near isothermal loop structure. It is also shown that the inclusion of flows in the coronal loop models (non-static loops) can give similar results[164]. Non-uniformity in the loop cross section, with a significant decrease near the foot points, can also make the temperature profile more isothermal than that in the case of constant cross section as seen by Landi et al. (2004)[165]. We investigated the thermal profile along coronal loop using data observed with the BBSO/GST and at all other wavelengths (see Figure 6.1) which shows a loop at different wavelengths representing the different layers on sun. The mechanism that heats the corona and injects chromospheric plasma into the closed magnetic flux is highly localised. The mechanism behind plasma filling, dynamic flows and coronal heating remains a mystery. The mechanism(s) must be stable enough to continue to feed the corona with chromospheric plasma and powerful enough to accelerate and therefore heat the plasma from 6000 K to well over 1 MK over the short distance from the chromosphere and transition region to the corona. This is the very reason coronal loops are targeted for intense study. They are anchored to the photosphere, are fed by chromospheric plasma, protrude into the transition region and exist at coronal temperatures after undergoing intensive heating. The idea that the coronal heating problem is solely down to some coronal heating mechanism is misleading. We make an attempt to make clear the heating mechanism of the coronal loop rooted at the umbral boundaries as can be seen in Figure 6.2. The main focus is on the region marked within the white box. The probability that a magnetic reconnection might be producing heating in the loop is the question that needs to be answered. The white contours in Figure 6.2 (a) shows the IRIS 1400 Å profile of the loop at 18:32:23 UT. As there were

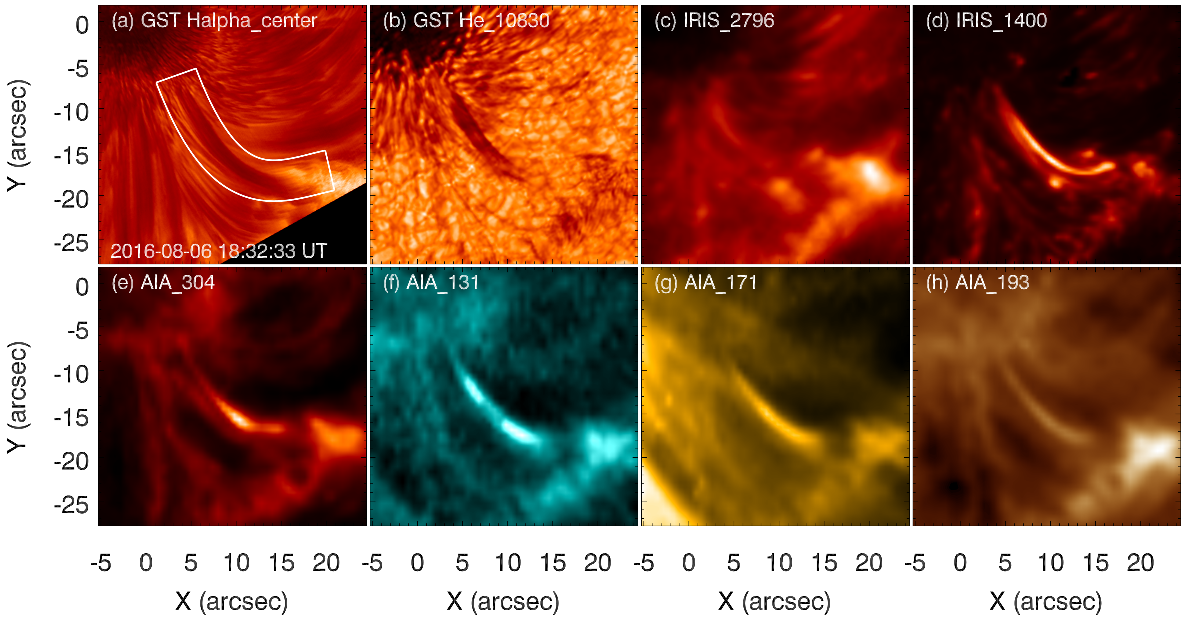

图 6.1: Multiwavelength images showing brightening along the loop rooted at the umbral boundary.

no evident magnetic cancellations observed at the top of the footpoint as shown by Figure 6.2 (c)-(f), and at its bottom footpoint shown in Figure 6.2 (g)-(j), the concept of magnetic reconnection is ruled out.

A closer look at the loop gave an insight into the concept that the sunspot is rotating. The rotation could be seen in He I 10830 images in Figure 6.3 (a)-(b). Does this rotation cause loop heating? The Panel (c) of Figure 6.3 shows that in more than 4.5 hours, sunspot rotated clockwise round 30°. Stretched by the rotating sunspot, the dark fibrils would rotate clockwise as well.

The Magnetic twist could be an element in understanding the physics of coronal loops since it may be responsible for the coronal heating. The rotational motion of a loop around its axis reported from SOHO SUMER observations may be considered as an evidence for the magnetic twist[106]. Similar rotation in the loop is seen in Figure 6.5. Also, it is well known that ARs contain significant amount of magnetic helicity[110], a fraction of which may exist in the form of the magnetic twist of coronal loops. With the Non-linear force free extrapolation as shown in Figure 6.4 (a), the fibrils were found likely rooted in the areas of negative current helicity. The question is if a positive or negative helicity gets transported to the fibrils from the photosphere? The areas shows the feature of negative helicity see shown by Figure 6.4 (c)-(j). It indicates that the rotating sunspot transported negative helicity along the fibrils. Corresponding to sunspot rotation, the fibrils show clockwise rotations at their bottom as shown by H_{los} velocity as seen in Figure 6.5. We speculate that several fibrils could have twisted together and merged into one thus showing brightening. It might also be possible

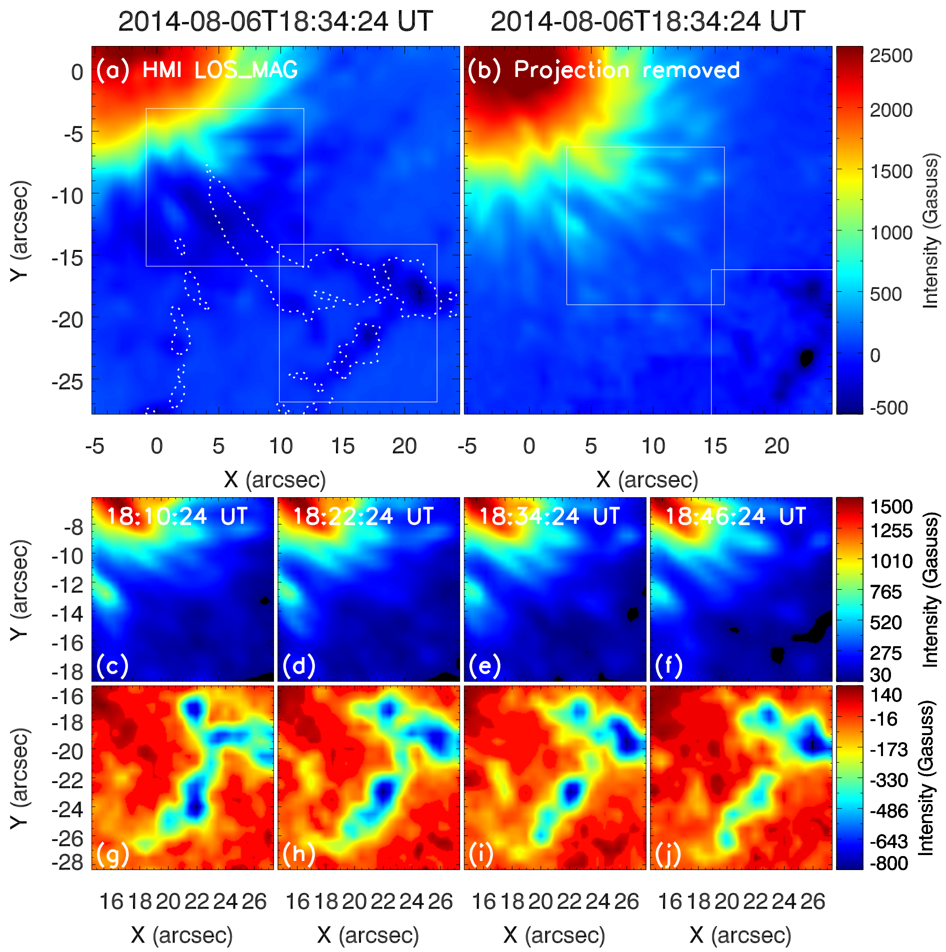

图 6.2: (a) and (b) are the images of HMI line of sight magnetogram. The white contours shows the profile of IRIS 1400 Å overplotted along the loop. (c)-(j) shows the morphological evolution in the regions marked with box in (a).

that the twist of fibrils may lead to an increase in the electric current and due to Ohmic loss, the fibril gets heated up.

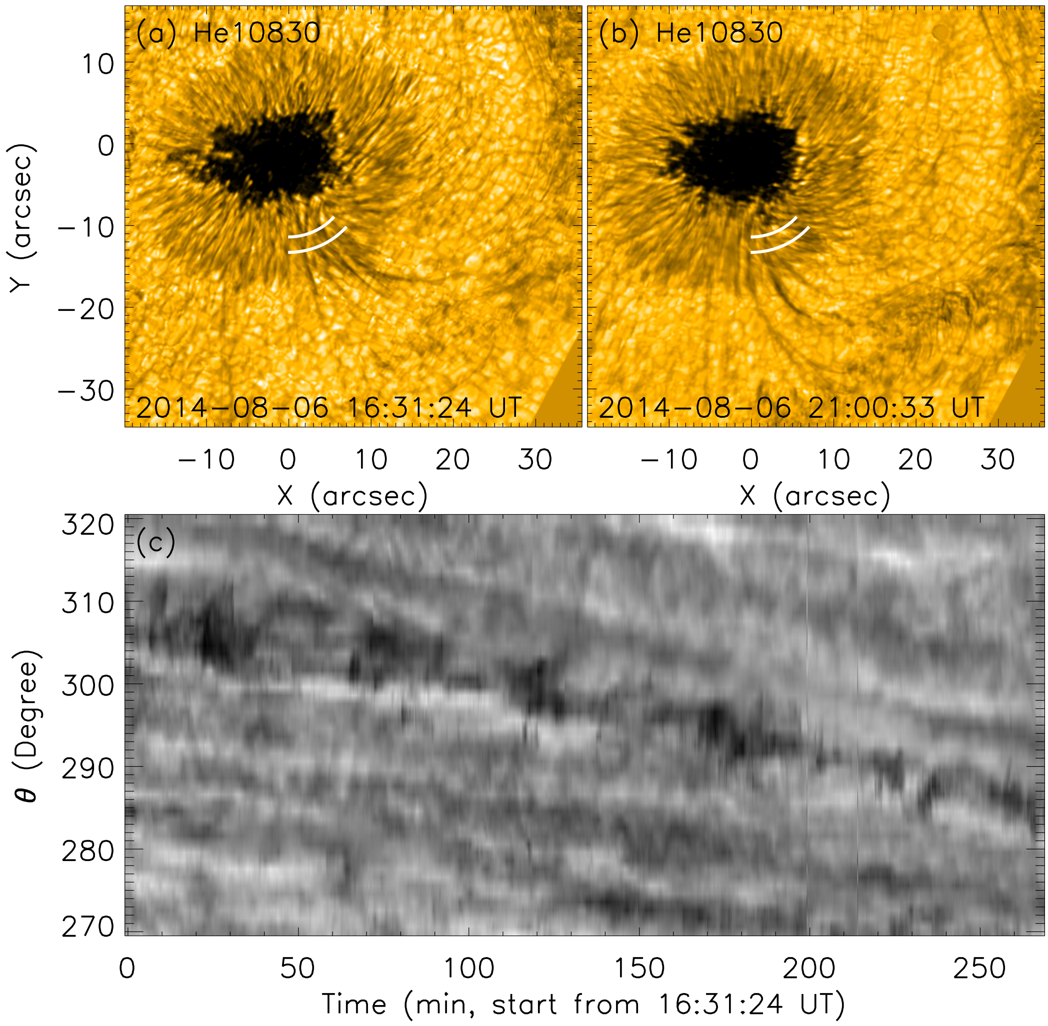

图 6.3: (a) and (b) is the sunspot in He I 10830 Å showing the rotation. Panel (c) shows the sunspot rotated by ∼30°.

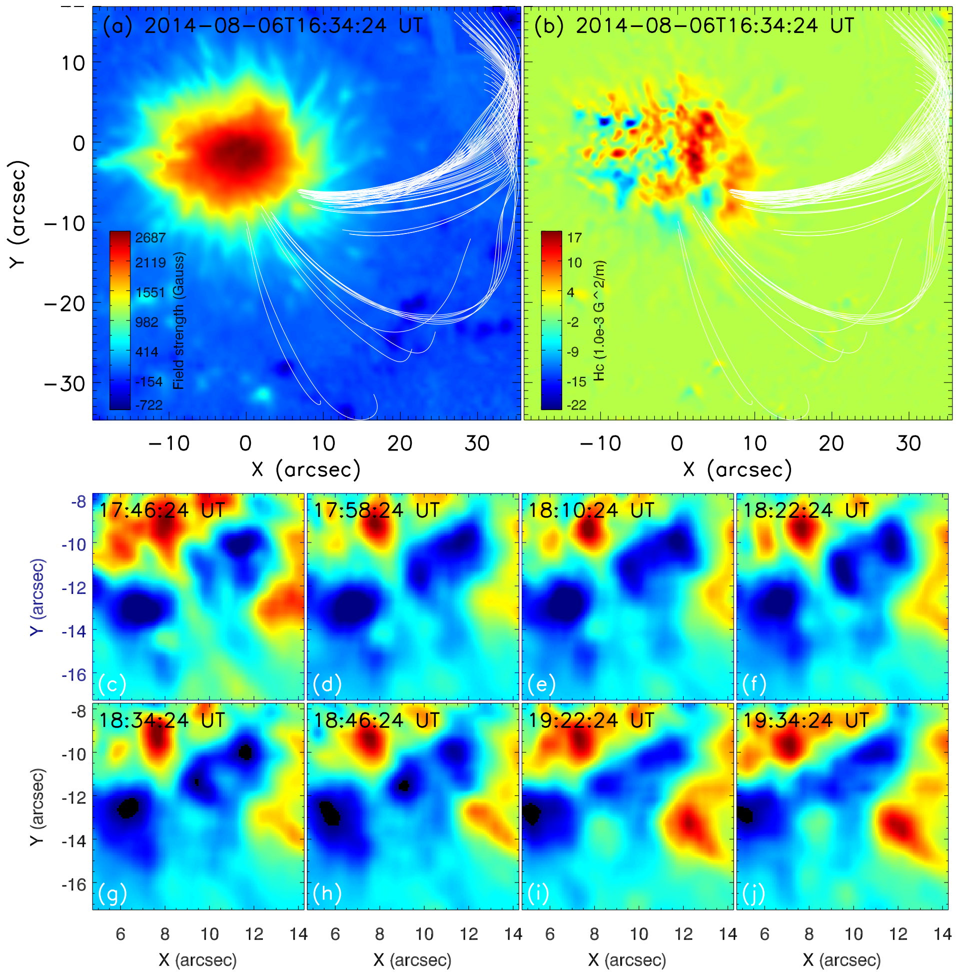

图 6.4: (a) and (b) shows non linear force free extrapolation along the fibrils rooted at the umbral boundary. (c) to (j) shows the negative helicity retained along the region marked as box in (b).

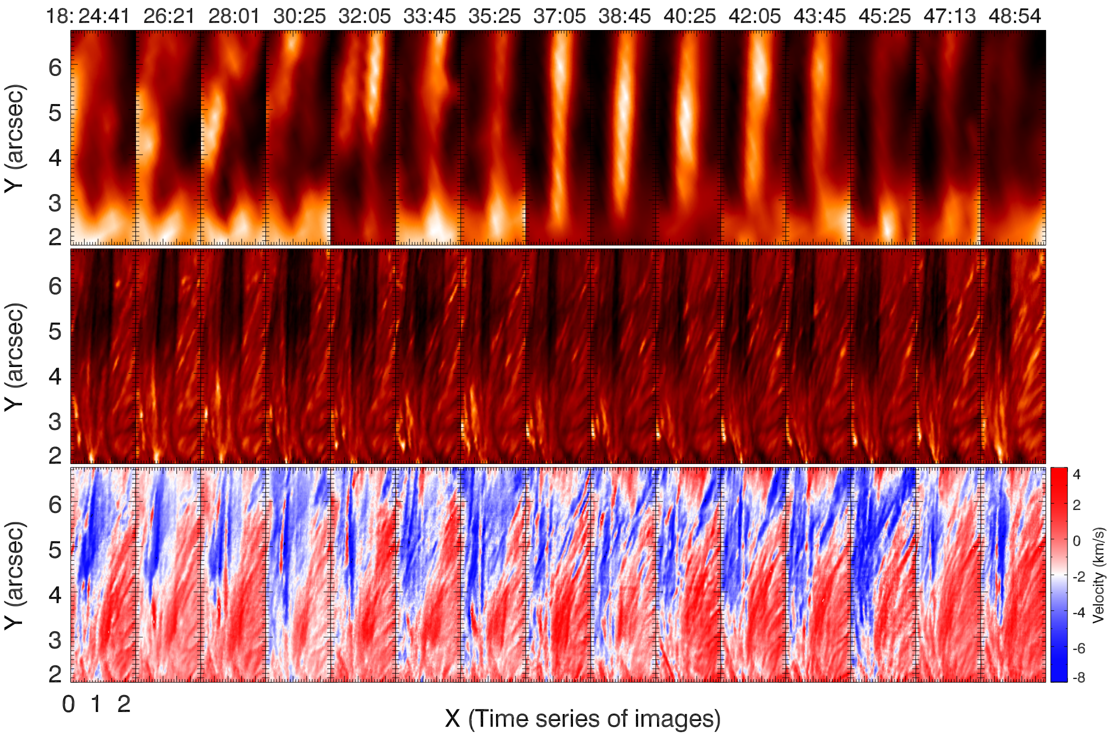

图 6.5: Shows the twist along the fibril in (a) AIA - 304 Å (top), (b) H$\alpha - 0.6$ Å (middle) and (c) at LOS velocity (bottom).

第七章 Conclusions and future scope

The high resolution imaging observations of active region NOAA AR 12132 helped in investigating the umbral oscillations and RPWs. The main results are discussed below.

1. We find that the detection of long period oscillations in the chromospheric umbra is quite difficult which happens to be consistently matching with the theory of MHD wave propagation in the inclined magnetic field. The power that we observe with our data contributes to only 5% of the power observed with TiO. We find a new result with the filtered image observations that a lot of umbral oscillations originates either at the umbral boundary or very close to the umbral boundary. It is also observed that the umbral oscillations are a part of the preceding RPWs. It is seen that the wavefronts separates from the preceding wavefronts and moves into the umbral center, and expands radially to begin a new oscillation. We find this scenario to be consistent with the MHD wave propagation. This phenomena is clearly shown in Figure 4.10 (f) which reveals that the new wavefront emerges at the umbral center. The panels in Figure 4.10 (a)-(e) shows that the umbral oscillations are related to the preceding RPWs whereas the panels in Figure 4.10 (g)-(l) shows that the umbral oscillations are related to the following RPWs. Such a finding is seen with nearly all the umbral oscillations. We remark that this observational result clearly contributes to an observational evidence as how an umbral oscillation is associated with the preceding and following RPWs. It could also be seen from Figure 4.9 and Figure 4.10 clearly that the wavefronts forms a spiral structure indicating a twist in the waveguides which could probably be the reason why the wavefronts are first seen at high latitudes and then at lower latitudes of the umbral center. But due to the association of RPWs with the umbral oscillations, the 5-min signal goes almost undetected at the umbral boundaries. De Pontieu at al. (2004)[17] interpreted the leakage of leakage of p-modes or photospheric oscillations into the chromosphere along the inclined magnetic flux tubes and Khomenko et al. (2008)[166] explains that 5-min oscillations can leak into the chromosphere through small-scale vertical magnetic flux tubes due to the efficiency of energy exchange by radiation in the solar photosphere that can lead to a significant reduction of the cutoff frequency and may allow the propagation of the 5-min waves vertically into the chromosphere. This completely supports our observational view giving a way to study further

if these propagating oscillations might be a driver for the dynamic fibrils that originates from the sunspots. To support our view we studied all the dynamic fibrils that originated from the sunspot. The dynamic fibrils have been studied extensively by many scientific groups. Tremendous amount of work has been carried out by De Pontieu et al. (2004)[17]. The jet-like features which are also known as spicules, mottles and DFs are observed on the limb, QS disk and in ARs respectively. We examined the correlation between the maximum velocity of the fibrils and its deceleration, and found that the inclined magnetic fields allow normally evanescent long period waves to propagate into the upper chromosphere and corona as seen by[11,17,146,148–150,167].

2. It is identified the correlations to be the signatures for the periodic jets to be driven by waves that propagates from lower atmosphere into chromosphere where they steepen into shocks in their numerical simulations[155]. The dynamic fibrils are generally considered to have shorter maximum lengths, shorter durations, lower maximum velocities, and smaller decelerations. The maximum velocities of these jet like features in our observation are in the range 10-30 km s^{-1}, which is comparable to those of[11,146]. The chromospheric waves are believed to be generated by convective flows and oscillations in the photosphere/convection zone. The magnetic field concentrations allows these disturbances to propagate up into the chromosphere. While they propagate upward, the disturbances shock and drives the chromospheric plasma upward, thereby forming DFs in the process. The chromosphere does not allow the waves with periods longer than the local acoustic cutoff period to propagate. The acoustic cutoff period depends on how much the magnetic field lines are inclined with respect to the vertical[17,150]. The DFs formed along the inclined magnetic field line experiences just a component of gravity. The correlation observed between the deceleration and the maximum velocity can be understood in terms of shock wave physics and that the DFs are driven by single shocks. DFs with higher maximum velocity, which means those driven by stronger shocks, will show greater deceleration, for a given lifetime of DF. The high-resolution chromospheric data and the numerical simulation suggests that these DFs are consequence of upwardly propagating chromospheric oscillations/waves. These waves are generated in the convection zone/photosphere due to global p-mode oscillations and convective flows, propagates into and also through the chromosphere, forms shocks during their propagation up to the regions where Hα is formed. The facts on which we stress our interpretation is that the DFs follow a parabolic path with a good positive correlation between the velocity and deceleration

of all DFs, the higher the velocity, the more deceleration. The evidence to show that the quiet-Sun mottles follow parabolic paths with decelerations that are small to be in consistency with the purely ballistic flight at solar gravity is found[100]. The velocities reports[100] for mottles are typically of order 10-30 km s^{-1}, and are similar to those we find in our BBSO/NST observations of DFs. From these results and also by the other results[146], it is almost clear that in ARs, the DFs are formed by chromospheric shocks driven by convective flows and oscillations in the photosphere. However, we would like to conclude that its driving mechanism and also its nature must be the same.

3. The simulations by Heggland et al. (2007)[147,157] explains on the idea that long-period waves propagates along the inclined magnetic fields into higher and lower density regions of the solar atmosphere[17]; and was previously investigated[148–150]. Inclined magnetic fields change the acoustic cutoff period for waves that happen to propagate along the magnetic field due to the lower effective gravity so that the long-period waves can propagate into higher atmospheric where they would be evanescent otherwise in non-magnetic regions. The analysis of DFs has increased in few years due to the important advances in both observational and simulation efforts[11,17,146]. One of the important conclusion is that DFs are driven by magnetoacoustic shocks caused by p-mode oscillations and leakage of convective flows into the chromosphere. The presence of upward propagating waves and also shocks in the sunspot atmospheres is a known fact from both the observations[33] and simulations[158]. The phenomena appears as a dark feature in the wings and core of Hα as well and are mostly associated with the concentrations of magnetic flux. The spicules observed at limb showed parabolic paths with decelerations and maximum velocities as those for mottles and DFs[168]. The similarities between spicule observations and some modeling done earlier on the DFs implies that the highly dynamic chromospheric shock waves causes a significant upward and downward motion of the upper chromosphere in active region and quiet Sun was proposed[17]. Zhang et al. (2007)[159] suggested that the oscillations which appears to be like surge or light walls which lies above the LB are also caused by shocks. Our findings indicates that, in ARs, most of these jet like features are caused by the shocks in chromosphere which are driven by convective flows and oscillations in the photosphere, this is comparable with the earlier findings but none of the earlier findings were based on BBSO/GST data.

4. The granular flows and the p-mode oscillations are considered to be the most abundant energy sources in the quiet regions of photosphere. The maximum energy is transported upwards when the magnetic filed lines are inclined vertically[17]. It was stated that DFs of longer periods are located in regions where magnetic fields are more horizontal[155]. The umbral oscillations and the running penumbral waves are considered to be the most well known patterns of chromospheric motions. We come with conclusions that the dynamic fibrils, superpenumbral fibrils outside the sunspot are driven by the oscillations inside the sunspot. It is quite possible that the dynamic fibrils and the oscillations inside the sunspots (more specifically the umbral oscillations), have a same driver. The basic result which confirms the earlier studies[141,146,155] is that at every position of these mentioned features, the $\lambda - t$ plots displays a sequence of N-shaped patterns compatible with the motion of upwardly propagating shock waves. We see from $\lambda - t$ plots that these N-shape patterns originates from the sunspot interior and propagates outward along the dynamic fibrils. The 3-min oscillations are more predominant at the sunspot center while the fibrils oscillates with much longer periods of about 8-9 minutes. This also confirms the previous studies by (Tziotziou 2006; Tziotziou 2007; RouppevanderVoort 2013; Jess 2013 and Chae 2014)[66,94,120,155,169].

5. Coronal heating is one of the hot topic and a fundamental topic of discussion in solar physics. The domination of corona by the magnetic field, makes the plasma of active region to be highly confined along the loops. These loops forms the basic blocks for understanding the heating problem, which essentially needs the analysis and evolution of these so called loops. Our analysis finds such a loop rooted at the sunspot umbral boundary showing brightening along the loop. We presume that this brightening could be either due to the twisting of all the fibrils together into one which results in some ohmic loss and becomes a cause for the heating of the loop. The exact physical process responsible for this brightening remains to be explored.

参考文献

[1] J. R. Lemen, *et al.* The Atmospheric Imaging Assembly (AIA) on the Solar Dynamics Observatory (SDO). *Sol. Phys.* **275**, 17–40 (2012).

[2] W. Cao, *et al.* Scientific instrumentation for the 1.6 m New Solar Telescope in Big Bear. *Astronomische Nachrichten* **331**, 636 (2010).

[3] S. H. Yang, J. Zhang, C. L. Jin, L. P. Li, H. Y. Duan. Response of the solar atmosphere to magnetic field evolution in a coronal hole region. *A&A* **501**, 745–753 (2009).

[4] M. J. Aschwanden. *Physics of the Solar Corona. An Introduction with Problems and Solutions (2nd edition)* (2005).

[5] J. Joshi. *Magnetic and Velocity Field of Sunspots in the Photosphere and Upper Chromosphere*. Ph.D. thesis, Max-Planck Institute for Solar System Research (2014).

[6] J. H. Thomas, N. O. Weiss, eds. *Sunspots: Theory and observations; Proceedings of the NATO Advanced Research Workshop on the Theory of Sunspots, Cambridge, United Kingdom, Sept. 22-27, 1991*, vol. 375 of *NATO Advanced Science Institutes (ASI) Series C* (1992).

[7] S. K. Solanki. Sunspots: An overview. *A&A Rev.* **11**, 153–286 (2003).

[8] J. Löhner-Böttcher, N. Bello González. Signatures of running penumbral waves in sunspot photospheres. *A&A* **580**, A53 (2015).

[9] J. H. Thomas, L. E. Cram, A. H. Nye. Dynamical phenomena in sunspots. I - Observing procedures and oscillatory phenomena. *ApJ* **285**, 368–385 (1984).

[10] B. W. Lites, J. H. Thomas, T. J. Bogdan, P. S. Cally. Velocity and Magnetic Field Fluctuations in the Photosphere of a Sunspot. *ApJ* **497**, 464–482 (1998).

[11] B. De Pontieu, V. H. Hansteen, L. Rouppe van der Voort, M. van Noort, M. Carlsson. High-Resolution Observations and Modeling of Dynamic Fibrils. *ApJ* **655**, 624–641 (2007).

[12] W. D. Pesnell, B. J. Thompson, P. C. Chamberlin. The Solar Dynamics Observatory (SDO). *Sol. Phys.* **275**, 3–15 (2012).

[13] X. Y. Bai, *et al.* Multi-wavelength Observations of a Subarcsecond Penumbral Transient Brightening Event. *ApJ* **823**, 60 (2016).

[14] G. Vissers, L. Rouppe van der Voort. Flocculent Flows in the Chromospheric Canopy of a Sunspot. *ApJ* **750**, 22 (2012).

[15] A. Vögler, M. Schüssler. A solar surface dynamo. *A&A* **465**, L43–L46 (2007).

[16] O. Steiner, R. Rezaei, W. Schaffenberger, S. Wedemeyer-Böhm. The Horizontal Internetwork Magnetic Field: Numerical Simulations in Comparison to Observations with Hinode. *ApJL* **680**, L85 (2008).

[17] B. De Pontieu, R. Erdélyi, S. P. James. Solar chromospheric spicules from the leakage of photospheric oscillations and flows. *Nature* **430**, 536–539 (2004).

[18] J. T. Mariska, *et al.* Yohkoh BCS Observations of Doppler Shifts Early in Solar Flares. In *American Astronomical Society Meeting Abstracts #180*, vol. 24 of *Bulletin of the American Astronomical Society*, 761 (1992).

[19] A. G. de Wijn, J. O. Stenflo, S. K. Solanki, S. Tsuneta. *Small-Scale Solar Magnetic Fields*, 275 (2009).

[20] A. O. Benz. Flare Observations. *Living Reviews in Solar Physics* **5**, 1 (2008).

[21] M. J. Aschwanden. *Physics of the Solar Corona. An Introduction* (Praxis Publishing Ltd, 2004).

[22] E. Antonucci. Solar flare spectral diagnosis - Present and future. *Sol. Phys.* **121**, 31–60 (1989).

[23] T. Yokoyama, K. Akita, T. Morimoto, K. Inoue, J. Newmark. Clear Evidence of Reconnection Inflow of a Solar Flare. *ApJL* **546**, L69–L72 (2001).

[24] R. O. Milligan, P. T. Gallagher, M. Mathioudakis, F. P. Keenan. Observational Evidence of Gentle Chromospheric Evaporation during the Impulsive Phase of a Solar Flare. *ApJL* **642**, L169–L171 (2006).

[25] T. Wang, L. Sui, J. Qiu. Direct Observation of High-Speed Plasma Outflows Produced by Magnetic Reconnection in Solar Impulsive Events. *ApJL* **661**, L207–L210 (2007).

[26] H. Hara, T. Watanabe, L. K. Harra, J. L. Culhane, P. R. Young. Plasma Motions and Heating by Magnetic Reconnection in a 2007 May 19 Flare. *ApJ* **741**, 107 (2011).

[27] H. Tian, *et al.* Imaging and Spectroscopic Observations of Magnetic Reconnection and Chromospheric Evaporation in a Solar Flare. *ApJL* **797**, L14 (2014).

[28] L. Biermann. Der gegenwärtige Stand der Theorie konvektiver Sonnenmodelle. *Vierteljahresschrift der Astronomischen Gesellschaft* **76**, 194–200 (1941).

[29] K. Jahn. Magnetohydrostatic equilibrium in sunspot models. In Thomas, J. H. and Weiss, N. O.(editor) *NATO Advanced Science Institutes (ASI) Series C*, vol. 375 of *NATO Advanced Science Institutes (ASI) Series C*, 139–162 (1992).

[30] W. Deinzer. On the Magneto-Hydrostatic Theory of Sunspots. *ApJ* **141**, 548 (1965).

[31] F. Hoyle. *Some recent researches in solar physics.* (1949).

[32] L. H. Auer, J. N. Heasley. The origin of broad-band circular polarization in sunspots. *A&A* **64**, 67–71 (1978).

[33] B. W. Lites. Sunspot oscillations - Observations and implications. In Thomas, J. H. and Weiss, N. O.(editor) *NATO Advanced Science Institutes (ASI) Series C*, vol. 375 of *NATO Advanced Science Institutes (ASI) Series C*, 261–302 (1992).

[34] M. Landolfi, E. Landi Degl'Innocenti. Net Circular Polarization in Magnetic Spectral Lines Produced by Velocity Gradients: Some Analytical Results. *Sol. Phys.* **164**, 191–202 (1996).

[35] S. K. Solanki, U. Walther, W. Livingston. Infrared lines as probes of solar magnetic features. VI. The thermal-magnetic relation and Wilson depression of a simple sunspot. *A&A* **277**, 639 (1993).

[36] J. M. Borrero, *et al.* Magnetic Field Vector Retrieval With the Helioseismic and Magnetic Imager. *Sol. Phys.* **240**, 177–196 (2007).

[37] D. A. N. Müller, R. Schlichenmaier, O. Steiner, M. Stix. Spectral signature of magnetic flux tubes in sunspot penumbrae. *A&A* **393**, 305–319 (2002).

[38] D. A. N. Müller, R. Schlichenmaier, G. Fritz, C. Beck. The multi-component field topology of sunspot penumbrae. A diagnostic tool for spectropolarimetric measurements. *A&A* **460**, 925–933 (2006).

[39] J. M. Borrero, S. K. Solanki. Convective Motions and Net Circular Polarization in Sunspot Penumbrae. *ApJ* **709**, 349–357 (2010).

[40] V. Martínez Pillet. Spectral signature of uncombed penumbral magnetic fields. *A&A* **361**, 734–742 (2000).

[41] V. Martínez Pillet. Spectral signature of uncombed penumbral magnetic fields. Reply. *A&A* **369**, 644–645 (2001).

[42] S. K. Mathew, *et al.* Three dimensional structure of a regular sunspot from the inversion of IR Stokes profiles. *A&A* **410**, 695–710 (2003).

[43] L. R. Bellot Rubio, H. Balthasar, M. Collados, R. Schlichenmaier. Field-aligned Evershed flows in the photosphere of a sunspot penumbra. *A&A* **403**, L47–L50 (2003).

[44] J. M. Borrero, S. K. Solanki, A. Lagg, H. Socas-Navarro, B. Lites. On the fine structure of sunspot penumbrae. III. The vertical extension of penumbral filaments. *A&A* **450**, 383–393 (2006).

[45] J. M. Borrero, B. W. Lites, S. K. Solanki. Evidence of magnetic field wrapping around penumbral filaments. *A&A* **481**, L13–L16 (2008).

[46] C. Beck. An uncombed inversion of multiwavelength observations reproducing the net circular polarization in a sunspot's penumbra. *A&A* **525**, A133 (2011).

[47] K. D. Leka. The Vector Magnetic Fields and Thermodynamics of Sunspot Light Bridges: The Case for Field-free Disruptions in Sunspots. *ApJ* **484**, 900–919 (1997).

[48] I. Rueedi, S. K. Solanki, J. O. Stenflo, T. Tarbell, P. H. Scherrer. Oscillations of sunspot magnetic fields. *A&A* **335**, L97–L100 (1998).

[49] M. Sobotka, *et al.* Dynamics of the solar atmosphere above a pore with a light bridge. *A&A* **560**, A84 (2013).

[50] D. Yuan, *et al.* Oscillations in a Sunspot with Light Bridges. *ApJ* **792**, 41 (2014).

[51] I. Rueedi, S. K. Solanki, W. C. Livingston. Infrared lines as probes of solar magnetic features. X. HeI 10830A as a diagnostic of chromospheric magnetic fields. *A&A* **293**, 252–262 (1995).

[52] R. B. Leighton, R. W. Noyes, G. W. Simon. Velocity Fields in the Solar Atmosphere. I. Preliminary Report. *ApJ* **135**, 474 (1962).

[53] M. Stix. *The sun: an introduction* (2002).

[54] J. M. Beckers, P. E. Tallant. Chromospheric Inhomogeneities in Sunspot Umbrae. *Sol. Phys.* **7**, 351–365 (1969).

[55] R. G. Giovanelli. Oscillations and Waves in a Sunspot. *Sol. Phys.* **27**, 71–79 (1972).

[56] H. Zirin, A. Stein. Observations of Running Penumbral Waves. *ApJL* **178**, L85 (1972).

[57] J. H. Thomas. Oscillations in sunspots. *Australian Journal of Physics* **38**, 811–824 (1985).

[58] J. Staude. Magnetic field oscillations of sunspots? *Astronomische Nachrichten* **323**, 317–320 (2002).

[59] T. J. Bogdan, P. G. Judge. Observational aspects of sunspot oscillations. *Philosophical Transactions of the Royal Society of London Series A* **364**, 313–331 (2006).

[60] A. Bhatnagar, K. Tanaka. Intensity Oscillation in Hα-Fine Structure. *Sol. Phys.* **24**, 87–97 (1972).

[61] J. M. Beckers, R. B. Schultz. Oscillatory Motions in Sunspots. *Sol. Phys.* **27**, 61–70 (1972).

[62] B. W. Lites. Photoelectric observations of chromospheric sunspot oscillations. IV - The CA II H line and He I 10830 A. *ApJ* **301**, 1005–1017 (1986).

[63] T.-S. Yoon, H. S. Yun, J.-H. Kim. Dynamical Characteristics of Sunspot Chromospheres II. Analysis of CA II H, K and lambda 8498 Lines of a Sunspot(SPO 5007) for Oscillatory Motions. *Journal of Korean Astronomical Society* **28**, 245–253 (1995).

[64] J. B. Gurman, J. W. Leibacher, R. A. Shine, B. E. Woodgate, W. Henze. Transition region oscillations in sunspots. *ApJ* **253**, 939–948 (1982).

[65] V. Yurchyshyn, V. Abramenko, A. Kilcik. Dynamics in Sunspot Umbra as Seen in New Solar Telescope and Interface Region Imaging Spectrograph Data. *ApJ* **798**, 136 (2015).

[66] K. Tziotziou, G. Tsiropoula, N. Mein, P. Mein. Dual-line spectral and phase analysis of sunspot oscillations. *A&A* **463**, 1153–1163 (2007).

[67] T. E. Abdelatif, B. W. Lites, J. H. Thomas. The interaction of solar p-modes with a sunspot. I - Observations. *ApJ* **311**, 1015–1024 (1986).

[68] H. Balthasar, E. Wiehr, G. Kueveler. A comparison of the oscillations in sunspot umbrae, penumbrae, and the surrounding photosphere. *Sol. Phys.* **112**, 37–48 (1987).

[69] H. Balthasar, V. Martínez Pillet, H. Schleicher, H. Wöhl. Velocity Oscillations in Active Sunspot Groups. *Sol. Phys.* **182**, 65–72 (1998).

[70] L. R. Bellot Rubio, M. Collados, B. Ruiz Cobo, I. Rodríguez Hidalgo. Oscillations in the Photosphere of a Sunspot Umbra from the Inversion of Infrared Stokes Profiles. *ApJ* **534**, 989–996 (2000).

[71] N. I. Kobanov. On spatial characteristics of five-minute oscillations in the sunspot umbra. *Sol. Phys.* **125**, 25–30 (1990).

[72] N. I. Kobanov, D. V. Makarchik. Propagating waves in the sunspot umbra chromosphere. *A&A* **424**, 671–675 (2004).

[73] D. C. Braun, T. L. Duvall, Jr., B. J. Labonte. Acoustic absorption by sunspots. *ApJL* **319**, L27–L31 (1987).

[74] J. H. Thomas. Theories of dynamical phenomena in sunspots. In Cram, L. E. and Thomas, J. H.(editor) *The Physics of Sunspots*, 345–358 (1981).

[75] T. J. Bogdan. Sunspot Oscillations: A Review - (Invited Review). *Sol. Phys.* **192**, 373–394 (2000).

[76] R. Centeno, M. Collados, J. Trujillo Bueno. Wave Propagation and Shock Formation in Different Magnetic Structures. *ApJ* **692**, 1211–1220 (2009).

[77] M. Stangalini, F. Giannattasio, D. Del Moro, F. Berrilli. Three-minute wave enhancement in the solar photosphere. *A&A* **539**, L4 (2012).

[78] B. W. Lites. Photoelectric observations of chromospheric sunspot oscillations. II - Propagation characteristics. *ApJ* **277**, 874–888 (1984).

[79] F. Kneer, W. Mattig, M. v. Uexkuell. The chromosphere above sunspot umbrae. III - Spatial and temporal variations of chromospheric lines. *A&A* **102**, 147–155 (1981).

[80] R. Centeno, M. Collados, J. Trujillo Bueno. Spectropolarimetric Investigation of the Propagation of Magnetoacoustic Waves and Shock Formation in Sunspot Atmospheres. *ApJ* **640**, 1153–1162 (2006).

[81] D. B. Jess, A. Andić, M. Mathioudakis, D. S. Bloomfield, F. P. Keenan. High-frequency oscillations in a solar active region observed with the RAPID DUAL IMAGER. *A&A* **473**, 943–950 (2007).

[82] B. I. Demchenko, G. S. Minasyants, N. G. Makarenko, S. O. Obashev. On the Possible Oscillation of Sunspot. *Astronomicheskij Tsirkulyar* **1360**, 3 (1985).

[83] H. Zirin, A. Stein. Observations of Running Penumbral Waves. *ApJL* **178**, L85 (1972).

[84] A. H. Nye, J. H. Thomas. The nature of running penumbral waves. *Sol. Phys.* **38**, 399–413 (1974).

[85] C. E. Alissandrakis, A. A. Georgakilas, D. Dialetis. Dynamic phenomena in the chromospheric layer of a sunspot. *Sol. Phys.* **138**, 93–105 (1992).

[86] E. Marco, M. A. Aballe Villero, M. Vazquez, J. I. Garcia de La Rosa. Spatial changes of the oscillatory pattern in sunspot penumbrae at the photospheric level. *A&A* **309**, 284–290 (1996).

[87] G. Tsiropoula, C. E. Alissandrakis, B. Schmieder. Time evolution of fine structures in the solar chromosphere. *A&A* **290**, 285–294 (1994).

[88] E. B. Christopoulou, A. A. Georgakilas, S. Koutchmy. Oscillations and running waves observed in sunspots. *A&A* **354**, 305–314 (2000).

[89] N. I. Kobanov. The properties of velocity oscillations in vicinities of sunspot penumbra. *Sol. Phys.* **196**, 129–135 (2000).

[90] K. Tziotziou, G. Tsiropoula, P. Mein. Ca II 8542 Å sunspot oscillations observed with THEMIS. *A&A* **381**, 279–289 (2002).

[91] D. S. Bloomfield, A. Lagg, S. K. Solanki. The Nature of Running Penumbral Waves Revealed. *ApJ* **671**, 1005–1012 (2007).

[92] M. Sigwarth, W. Mattig. Velocity and intensity oscillations in sunspot penumbrae. *A&A* **324**, 743–749 (1997).

[93] C. A. Madsen, H. Tian, E. E. DeLuca. Observations of Umbral Flashes and Running Sunspot Waves with the Interface Region Imaging Spectrograph. *ApJ* **800**, 129 (2015).

[94] D. B. Jess, V. E. Reznikova, T. Van Doorsselaere, P. H. Keys, D. H. Mackay. The Influence of the Magnetic Field on Running Penumbral Waves in the Solar Chromosphere. *ApJ* **779**, 168 (2013).

[95] W. F. Brisken, H. Zirin. New Data and Models of Running Penumbral Waves in Sunspots. *ApJ* **478**, 814–816 (1997).

[96] J. Zhao, D.-Y. Chou. Analysis of the Helioseismic Power-Spectrum Diagram of a Sunspot. *Sol. Phys.* **287**, 149–159 (2013).

[97] N. Freij, *et al.* The Detection of Upwardly Propagating Waves Channeling Energy from the Chromosphere to the Low Corona. *ApJ* **791**, 61 (2014).

[98] J. M. Beckers. Solar Spicules (Invited Review Paper). *Sol. Phys.* **3**, 367–433 (1968).

[99] U. Grossmann-Doerth, W. Schmidt. Chromospheric fine structure revisited. *A&A* **264**, 236–242 (1992).

[100] Y. Suematsu, H. Wang, H. Zirin. High-Resolution Observation of Disk Spicules. I. Evolution and Kinematics of Spicules in the Enhanced Network. *ApJ* **450**, 411 (1995).

[101] H. Tian, *et al.* Prevalence of small-scale jets from the networks of the solar transition region and chromosphere. *Science* **346**, 1255711 (2014).

[102] G. E. Hale. On the Probable Existence of a Magnetic Field in Sun-Spots. *ApJ* **28**, 315 (1908).

[103] J. A. Watko, J. A. Klimchuk. Width Variations along Coronal Loops Observed by TRACE. *Sol. Phys.* **193**, 77–92 (2000).

[104] E. N. Parker. The origin of solar activity. *ARA&A* **15**, 45–68 (1977).

[105] J. A. Klimchuk, S. K. Antiochos, D. Norton. Twisted Coronal Magnetic Loops. *ApJ* **542**, 504–512 (2000).

[106] J. Chae, H. Wang, J. Qiu, P. R. Goode, K. Wilhelm. Active Region Loops Observed with SUMER on Board the SOHO. *ApJ* **533**, 535–545 (2000).

[107] J. Chae, Y.-J. Moon. Magnetic Twist of an Extreme-Ultraviolet Coronal Loop Inferred from Plasma Constriction. *ApJ* **629**, 1110–1121 (2005).

[108] C. J. Schrijver, *et al.* A new view of the solar outer atmosphere by the Transition Region and Coronal Explorer. *Sol. Phys.* **187**, 261–302 (1999).

[109] D. R. Williams, T. Török, P. Démoulin, L. van Driel-Gesztelyi, B. Kliem. Eruption of a Kink-unstable Filament in NOAA Active Region 10696. *ApJL* **628**, L163–L166 (2005).

[110] H. Jeong, J. Chae. Magnetic Helicity Injection in Active Regions. *ApJ* **671**, 1022–1033 (2007).

[111] M. J. Aschwanden, *et al.* Three-dimensional Stereoscopic Analysis of Solar Active Region Loops. I. SOHO/EIT Observations at Temperatures of (1.0-1.5) $\times 10^6$ K. *ApJ* **515**, 842–867 (1999).

[112] Z. Mikic, D. D. Schnack, G. van Hoven. Dynamical evolution of twisted magnetic flux tubes. I - Equilibrium and linear stability. *ApJ* **361**, 690–700 (1990).

[113] C. L. Gerrard, A. W. Hood, D. S. Brown. Effect of photospheric twisting motions on a confined toroidal loop. *Sol. Phys.* **222**, 79–94 (2004).

[114] S. Tsuneta, *et al.* The Soft X-ray Telescope for the SOLAR-A Mission. *Sol. Phys.* **136**, 37–67 (1991).

[115] S. Tsuneta. Interacting Active Regions in the Solar Corona. *ApJL* **456**, L63 (1996).

[116] T. Yoshida, S. Tsuneta. Temperature Structure of Solar Active Regions. *ApJ* **459**, 342 (1996).

[117] R. G. Giovanelli. Magnetic and Electric Phenomena in the Sun's Atmosphere associated with Sunspots. *MNRAS* **107**, 338 (1947).

[118] E. R. Priest. Magnetic reconnection on the sun. In Priest, E. R. and Krishan, V.(editor) *Basic Plasma Processes on the Sun*, vol. 142 of *IAU Symposium*, 271–288 (1990).

[119] E. R. Priest. Three-dimensional magnetic reconnection in the solar corona. *Physics of Plasmas* **4**, 1945–1952 (1997).

[120] J. Chae, *et al.* Superpenumbral Fibrils Powered by Sunspot Oscillations. *ApJ* **789**, 108 (2014).

[121] P. R. Goode, R. Coulter, N. Gorceix, V. Yurchyshyn, W. Cao. The NST: First results and some lessons for ATST and EST. *Astronomische Nachrichten* **331**, 620 (2010).

[122] P. Boerner, *et al.* Initial Calibration of the Atmospheric Imaging Assembly (AIA) on the Solar Dynamics Observatory (SDO). *Sol. Phys.* **275**, 41–66 (2012).

[123] J. Schou, *et al.* Design and Ground Calibration of the Helioseismic and Magnetic Imager (HMI) Instrument on the Solar Dynamics Observatory (SDO). *Sol. Phys.* **275**, 229–259 (2012).

[124] J. Schou, *et al.* Polarization Calibration of the Helioseismic and Magnetic Imager (HMI) onboard the Solar Dynamics Observatory (SDO). *Sol. Phys.* **275**, 327–355 (2012).

[125] J. T. Su, *et al.* Observations of Oppositely Directed Umbral Wavefronts Rotating in Sunspots Obtained from the New Solar Telescope of BBSO. *ApJ* **817**, 117 (2016).

[126] J. H. Thomas, L. E. Cram, A. H. Nye. Five-minute oscillations as a subsurface probe of sunspot structure. *Nature* **297**, 485–487 (1982).

[127] V. E. Reznikova, K. Shibasaki. Spatial Structure of Sunspot Oscillations Observed with SDO/AIA. *ApJ* **756**, 35 (2012).

[128] H. Tian, *et al.* Observations of Subarcsecond Bright Dots in the Transition Region above Sunspots with the Interface Region Imaging Spectrograph. *ApJL* **790**, L29 (2014).

[129] I. De Moortel, V. M. Nakariakov. Magnetohydrodynamic waves and coronal seismology: an overview of recent results. *Philosophical Transactions of the Royal Society of London Series A* **370**, 3193–3216 (2012).

[130] S. Régnier, *et al.* Sparkling Extreme-ultraviolet Bright Dots Observed with Hi-C. *ApJ* **784**, 134 (2014).

[131] T. Shimizu, R. A. Shine, A. M. Title, T. D. Tarbell, Z. Frank. Photospheric Magnetic Activities Responsible for Soft X-Ray Pointlike Microflares. I. Identifications of Associated Photospheric/Chromospheric Activities. *ApJ* **574**, 1074–1088 (2002).

[132] C. Liu, J. Qiu, D. E. Gary, S. Krucker, H. Wang. Studies of Microflares in RHESSI Hard X-Ray, Big Bear Solar Observatory Hα, and Michelson Doppler Imager Magnetograms. *ApJ* **604**, 442–448 (2004).

[133] J. Qiu, C. Liu, D. E. Gary, G. M. Nita, H. Wang. Hard X-Ray and Microwave Observations of Microflares. *ApJ* **612**, 530–545 (2004).

[134] C. Fang, P.-F. Chen, R.-L. Jiang, Y.-H. Tang. Synthetic analysis of a two-ribbon microflare. *Research in Astronomy and Astrophysics* **10**, 83–90 (2010).

[135] R. Kano, T. Shimizu, T. D. Tarbell. Hinode Observation of Photospheric Magnetic Activities Triggering X-ray Microflares Around a Well-developed Sunspot. *ApJ* **720**, 1136–1145 (2010).

[136] P. Zhang, C. Fang, Q. Zhang. H α counterparts of X-ray bright points in the solar atmosphere. *Science China Physics, Mechanics, and Astronomy* **55**, 907–914 (2012).

[137] F. Chen, M. D. Ding. Evidence of Explosive Evaporation in a Microflare Observed by Hinode/EIS. *ApJ* **724**, 640–648 (2010).

[138] J. Chae. Non-Coplanar Magnetic Reconnection as a Magnetic Twist Origin. *Journal of Korean Astronomical Society* **32**, 137–147 (1999).

[139] R.-L. Jiang, C. Fang, P.-F. Chen. Numerical Simulation of Solar Microflares in a Canopy-type Magnetic Configuration. *ApJ* **751**, 152 (2012).

[140] G. Tsiropoula, *et al.* Solar Fine-Scale Structures. I. Spicules and Other Small-Scale, Jet-Like Events at the Chromospheric Level: Observations and Physical Parameters. *Space Sci. Rev.* **169**, 181–244 (2012).

[141] B. de Pontieu, *et al.* A Tale of Two Spicules: The Impact of Spicules on the Magnetic Chromosphere. *PASJ* **59**, S655–S662 (2007).

[142] T. M. D. Pereira, B. De Pontieu, M. Carlsson. Quantifying Spicules. *ApJ* **759**, 18 (2012).

[143] L. H. M. Rouppe van der Voort, B. De Pontieu, V. H. Hansteen, M. Carlsson, M. van Noort. Magnetoacoustic Shocks as a Driver of Quiet-Sun Mottles. *ApJL* **660**, L169–L172 (2007).

[144] Y. Suematsu, K. Shibata, T. Neshikawa, R. Kitai. Numerical hydrodynamics of the jet phenomena in the solar atmosphere. I - Spicules. *Sol. Phys.* **75**, 99–118 (1982).

[145] K. Shibata, Y. Suematsu. Why are spicules absent over plages and long under coronal holes. *Sol. Phys.* **78**, 333–345 (1982).

[146] V. H. Hansteen, B. De Pontieu, L. Rouppe van der Voort, M. van Noort, M. Carlsson. Dynamic Fibrils Are Driven by Magnetoacoustic Shocks. *ApJL* **647**, L73–L76 (2006).

[147] L. Heggland, V. H. Hansteen, B. De Pontieu, M. Carlsson. Wave Propagation and Jet Formation in the Chromosphere. *ApJ* **743**, 142 (2011).

[148] A. G. Michalitsanos. The Five Minute Period Oscillation in Magnetically Active Regions. *Sol. Phys.* **30**, 47–61 (1973).

[149] N. Bel, B. Leroy. Analytical Study of Magnetoacoustic Gravity Waves. *A&A* **55**, 239 (1977).

[150] Y. Suematsu. Influence of Photospheric 5-Minute Oscillations on the Formation of Chromospheric Fine Structures. In Osaki, Y. and Shibahashi, H.(editor) *Progress of Seismology of the Sun and Stars*, vol. 367 of *Lecture Notes in Physics, Berlin Springer Verlag*, 211 (1990).

[151] Ø. Langangen, L. Rouppe van der Voort, Y. Lin. Measurements of Plasma Motions in Dynamic Fibrils. *ApJ* **673**, 1201–1208 (2008).

[152] J. M. Krijger, *et al.* Dynamics of the solar chromosphere. III. Ultraviolet brightness oscillations from TRACE. *A&A* **379**, 1052–1082 (2001).

[153] D. Mihalas, B. W. Mihalas. *Foundations of radiation hydrodynamics* (1984).

[154] V. Yurchyshyn, V. Abramenko, A. Kosovichev, P. Goode. High Resolution Observations of Chromospheric Jets in Sunspot Umbra. *ApJ* **787**, 58 (2014).

[155] L. Rouppe van der Voort, J. de la Cruz Rodríguez. Short Dynamic Fibrils in Sunspot Chromospheres. *ApJ* **776**, 56 (2013).

[156] R. F. Stein, J. Leibacher. Waves in the solar atmosphere. *ARA&A* **12**, 407–435 (1974).

[157] L. Heggland, B. De Pontieu, V. H. Hansteen. Numerical Simulations of Shock Wave-driven Chromospheric Jets. *ApJ* **666**, 1277–1283 (2007).

[158] S. Bard, M. Carlsson. Radiative Hydrodynamic Simulations of Acoustic Waves in Sunspots. *ApJ* **722**, 888–898 (2010).

[159] J. Zhang, H. Tian, J. He, L. Wang. Surge-like Oscillations above Sunspot Light Bridges Driven by Magnetoacoustic Shocks. *ApJ* **838**, 2 (2017).

[160] T. Gold, F. Hoyle. On the origin of solar flares. *MNRAS* **120**, 89 (1960).

[161] P. A. Sturrock, Y. Uchida. Coronal heating by stochastic magnetic pumping. *ApJ* **246**, 331–336 (1981).

[162] R. Rosner, W. H. Tucker, G. S. Vaiana. Dynamics of the quiescent solar corona. *ApJ* **220**, 643–645 (1978).

[163] M. J. Aschwanden, C. J. Schrijver, D. Alexander. Modeling of Coronal EUV Loops Observed with TRACE. I. Hydrostatic Solutions with Nonuniform Heating. *ApJ* **550**, 1036–1050 (2001).

[164] A. R. Winebarger, H. Warren, A. van Ballegooijen, E. E. DeLuca, L. Golub. Steady Flows Detected in Extreme-Ultraviolet Loops. *ApJL* **567**, L89–L92 (2002).

[165] E. Landi, U. Feldman. Models for Solar Magnetic Loops. IV. On the Relation between Coronal and Footpoint Plasma in Active Region Loops. *ApJ* **611**, 537–544 (2004).

[166] E. Khomenko, R. Centeno, M. Collados, J. Trujillo Bueno. Channeling 5 Minute Photospheric Oscillations into the Solar Outer Atmosphere through Small-Scale Vertical Magnetic Flux Tubes. *ApJL* **676**, L85 (2008).

[167] B. De Pontieu, R. Erdélyi, I. De Moortel. How to Channel Photospheric Oscillations into the Corona. *ApJL* **624**, L61–L64 (2005).

[168] E. B. Christopoulou, A. A. Georgakilas, S. Koutchmy. Fine Structure of the Magnetic Chromosphere: Near-Limb Imaging, Data Processing and Analysis of Spicules and Mottles. *Sol. Phys.* **199**, 61–80 (2001).

[169] K. Tziotziou, G. Tsiropoula, N. Mein, P. Mein. Observational characteristics and association of umbral oscillations and running penumbral waves. *A&A* **456**, 689–695 (2006).

个人简历

Personal Information

1. Name: Priya T G
2. Gender: Female
3. Date of Birth: 17-11-1981
4. Marital Status: Married
5. Nationality: Indian

Education

- Sep 2014 to Jun 2018 - Ph.D. Physics, NAOC, CAS, Beijing
- Jun 2002 to Jun 2004 - M.Sc. Physics, Mangalore University, Mangalore, India
- Jun 1999 to Jun 2002 - B.Sc. Physics (Major), Mathematics and Electronics, St.Aloysius College, Mangalore, India

Research Experience

- Sep 2014 to Till date - PhD Scholar, National Astronomical Observatories, CAS, Beijing
- Jun 2013 to May 2014 - Research Scholar, North-West university, Mafikeng, South Africa
- Oct 2011 to May 2013 - Project Associate, Indian Institute of Astrophysics(IIA), Bangalore
- Sep 2008 to Sep 2011 - Research Trainee, Indian Institute of Astrophysics, Kodaikanal Observatory.

Academic Fellowships

- Awarded CAS-TWAS Presidential Fellowship for PhD 2014 by Chinese Academy of Sciences, Beijing

发表文章目录

[1] **Priya,T.G.**, Wenda Cao, Jiangtao Su, Jie Chen, Xinjie Mao, Yuanyong Deng and Robert Erdelyi , 2018, *Observations of Running Penumbral Waves emerging in a Sunspot*, **The Astrophysical Journal**, Vol. 852, 15.

[2] **Priya,T.G.**, Thambaje Gopalan Priya, Jiang-Tao Su, Jie Chen, Yuan-Yong Deng and Debi Prasad Choudhury, 2018, *Statistical analysis of dynamic fibrils observed from NST/BBSO observations*, **RAA**, Vol.18, 2.

[3] **Priya,T.G.**, Yuanyong Deng, Su J.T., 2018, *Coronal loop heating along the fibril rooted at umbral boundary*, **In preparation**

[4] **Priya,T.G.**, Su J.T., and Robert Erdelyi, 2018, *Where do running penumbral waves emerge in chromosphere*, **Proceedings of the International Astronomical Union**, **Accepted**

[5] Bai, X.Y. and Su, J.T. and Cao, W.D. and Liu, S.Q. Deng, Y.Y. and **Priya,T.G.**, 2016, *Multi-wavelength Observations of a Subarcsecond Penumbral Transient Brightening Event*, **The Astrophysical Journal** Vol. 823, 60.

[6] Su, J.T. and Ji, K.F. Cao, W. Banerjee, D. **Priya,T.G.**, Zhao, J.S. Bai, X.Y.Chen, J. Zhang, M. and Ji, H.S., 2016, *Observations of Oppositely Directed Umbral Wavefronts Rotating in Sunspots Obtained from the New Solar Telescope of BBSO*, **The Astrophysical Journal** Vol. 817, 117.

[7] Su, J.T., Ji K.F.,Banerjee, D, Cao W.D., **Priya,T.G.**, Zhao, J.S., Yu, S.J., Ji H.S. and Zhang, M., 2016, *Interference of the Running Waves at Light Bridges of a Sunspot*, **The Astrophysical Journal** Vol. 816, 30.

[8] Chen, J., Su J., Yin Z, **Priya,T.G.**, Zhang H, Liu, J., Xu H, Yu S., 2015, *Recurrent Solar Jets Induced by a Satellite Spot and Moving Magnetic Features*, **The Astrophysical Journal** Vol. 2015, 71.

[9] Su J.T. Liu Y, Shen Y.D, **Priya,T.G.**, 2014, *Imaging Observation of Quasi-periodic Disturbances' Amplitudes Increasing with Height in the Polar Region of the Solar Corona*, **The Astrophysical Journal** Vol. 2014, 150.

致　谢

I feel immense pleasure in expressing my sincere and heartfelt gratitude to NAOC for giving me a chance to be a part of the institute. My sincere gratitude and thanks to my supervisors, Prof. Deng Yuanyong and Prof. Jiangtao Su, for their invaluable guidance throughout the tenure. I am indebted to Prof. Deng Yuanyong, for all the wonderful discussions we had and for his patience in explaining me simpler things. My special thanks are due to Prof. Jiangatao Su, for his constant encouragement and support, without which much of the work in this thesis would not have reached the stage of completion. From his scientific instinct, profound knowledge and remarkable expertise I have learned so much. I thank him for reading and improving all my manuscripts as well as for teaching me the way of scientific writing and approaches. It was all my pleasure to work with them. Words are less to thank Dr. Haixing Xu and Dr. Xianyong Bai who helped me in my intial period of PhD and later too. My heartfelt thanks to Prof Hui Tian of Peking university for suggestion and discussions in various aspects. I am thankful to Prof. Zhang Hongqi for many interesting discussions. I would also like to thank Prof. Jingxu Wang for all the good advices and discussions we had in the coffee room. I also want to thank Prof. Robertus Erdelyi and Prof. Debi Prasad Choudhury for initiating the collaborative works and showing me a path to successful research. A special thanks to my officemates for the good company and for interesting dicussions on many things. I would also like to thank passed out students like Song Yogliang, Zhang Xiaomin, Wei and Zhang Yang for their helping hand in solving many of my problems which I faced in my initial stay at Beijing. A big thanks to Dr. Susant Bisoi for helping me in dealing with issues related to IDL programming and useful discussions. I specially thank Dr. Chen Jie for assisting me in many ways. It is my pleasure to thank Prof. Gang Zhao (Supervisor of my husband) for all the help and support extended by him. I want to give thanks to all of my colleagues at HSOS. Last but not the least I owe tremendous gratitutde to my family (my in laws, my parents) for believing me. Nothing would have been possible without the support of my dear husband and my little daughter who are always there for me, provides me with the necessary balance, and makes my life completely rich.

Finally I would like to acknowledge the financial support from The World Academy of Sciences (TWAS), the Chinese Academy of Sciences (CAS) in the form of Presidential Fellowship